



University of Pennsylvania
ScholarlyCommons

Publicly Accessible Penn Dissertations

2013

From Engineering of Tumor Shrinking Dds to Engineering the Nucleus for Tumor Growth

Takamasa Harada
University of Pennsylvania, tkmsharada@gmail.com

Follow this and additional works at: <https://repository.upenn.edu/edissertations>

 Part of the [Chemical Engineering Commons](#)

Recommended Citation

Harada, Takamasa, "From Engineering of Tumor Shrinking Dds to Engineering the Nucleus for Tumor Growth" (2013). *Publicly Accessible Penn Dissertations*. 761.
<https://repository.upenn.edu/edissertations/761>

This paper is posted at ScholarlyCommons. <https://repository.upenn.edu/edissertations/761>
For more information, please contact repository@pobox.upenn.edu.

From Engineering of Tumor Shrinking Dds to Engineering the Nucleus for Tumor Growth

Abstract

Key questions in this study are how to shrink tumors in vivo and what physical property of cancer cell determines tumor invasiveness. Delivery of drug molecules to distant tumor tissue in the body is the highest challenge in any types of cancer therapies, and this goal was approached from two aspects in the first half of the study, namely using worm-like shaped drug delivery vehicle or Filomicelle and adding protein CD47 to the vehicle surface, which can send a stop signal to macrophage phagocytosing a foreign material. Drug-loaded Filomicelles applied for brain tumor treatment in combination with radiation therapy to obtain the access inside brain tissue by disrupting blood brain barrier. CD47-attached particle was tested for accumulation in tumor tissue, followed by subcutaneous tumor shrinkage study. Second half of the study focuses on cell nuclear physics in the context of cell migration and tumor progression as a physiological example where cell migration plays an essential role for progression. Nuclear stiffness was controlled by changing the expression of Lamin-A,C, a protein forming mesh structure underneath inner nuclear membrane to give a physical strength the nucleus. Relative expression of Lamin-A,C to its isoform Lamin-B nicely predicts behavior of nuclear shape after stress application and importantly cell migration sensitivity against Lamin-A,C change through physically constraining environment. This observation leads to quite simple viscoelastic model in which Lamin-A,C and -B are responsible for nuclear viscosity and elasticity, respectively.

Degree Type

Dissertation

Degree Name

Doctor of Philosophy (PhD)

Graduate Group

Chemical and Biomolecular Engineering

First Advisor

Dennis E. Discher

Keywords

cancer, CD47, cell migration, drug delivery, lamin A/C

Subject Categories

Chemical Engineering

This dissertation is available at ScholarlyCommons: <https://repository.upenn.edu/edissertations/761>

FROM ENGINEERING OF TUMOR SHRINKING DDS
TO
ENGINEERING THE NUCLEUS FOR TUMOR GROWTH

Takamasa Harada

A DISSERTATION

in

Chemical and Biomolecular Engineering

Presented to the Faculties of the University of Pennsylvania

in

Partial Fulfillment of the Requirements for the

Degree of Doctor of Philosophy

2013

Supervisor of Dissertation

Dennis E. Discher, Ph.D.

Professor of Chemical and Biomolecular Engineering

Graduate Group Chairperson

Raymond J. Gorte, Russell Pearch and Elizabeth Crimian Heuer Professor

Dissertation Committee

Dr. Matthew J. Lazzara, Assistant Professor of Chemical and Biomolecular Engineering

Dr. Daeyeon Lee, Assistant Professor of Chemical and Biomolecular Engineering

Dr. Kris Noel Dahl, Associate Professor of Chemical Engineering and Biomedical Engineering

To my family

ACKNOWLEDGMENT

First I would like to show my appreciation to Dennis as my advisor. His Hard work and dedication to science gave great influence on me throughout my time in graduate study. I also greatly appreciate Dr. Abdullah Mahmud for polymer synthesis in Chapter 2, Brian Baumann and others in Dr. Gary Cao/Dr. Jay Dorsey group for their help in radiation study in Chapter 2, Pia Rodriguez for polystyrene beads surface modifications in Chapter 3, Dr. Joe Swift for Mass Spectrometry analyses in Chapter 4, Tony Secreto and Joshua Glover for their helps in animal experiments throughout the work.

ABSTRACT

FROM ENGINEERING OF TUMOR SHRINKING DDS TO ENGINEERING THE NUCLEUS FOR TUMOR GROWTH

Takamasa Harada

Prof. Dennis E. Discher

Key questions in this study are how to shrink tumors in vivo and what physical property of cancer cell determines tumor invasiveness. Delivery of drug molecules to distant tumor tissue in the body is the highest challenge in any types of cancer therapies, and this goal was approached from two aspects in the first half of the study, namely using worm-like shaped drug delivery vehicle or Filomicelle and adding protein CD47 to the vehicle surface, which can send a stop signal to macrophage phagocytosing a foreign material. Drug-loaded Filomicelles applied for brain tumor treatment in combination with radiation therapy to obtain the access inside brain tissue by disrupting blood brain barrier. CD47-attached particle was tested for accumulation in tumor tissue, followed by subcutaneous tumor shrinkage study. Second half of the study focuses on cell nuclear physics in the context of cell migration and tumor progression as a physiological example where cell migration plays an essential role for progression. Nuclear stiffness was controlled by changing the expression of Lamin-A,C, a protein forming mesh structure underneath inner nuclear membrane to give a physical strength the nucleus. Relative expression of Lamin-A,C to its isoform Lamin-B nicely predicts behavior of nuclear shape after stress application and importantly cell migration sensitivity against Lamin-A,C change through physically constraining environment. This observation leads to quite simple viscoelastic model in which Lamin-A,C and -B are responsible for nuclear viscosity and elasticity, respectively.

LIST OF TABLES

Table. 3-1 List of papers studying with PEG-coated particles and showing opsonization (binding) with IgG	53
Table S4-1. Proteome of Lamin-A moderate knockdown A549 cells.....	117
Table S4-2. Proteomic difference between tumor vs. cultured cells	118-119

List of Illustrations

Figure 1-1. Overview of the thesis	10
Figure 2-1. Basic characterization of Filomicelles.....	27-28
Figure 2-2. Summary of cytotoxicity assay with TAX-loaded polymer formulations with distinct morphologies.....	29-30
Figure 2-3. Tumor shrinkage with TAX-loaded Filomicelles.....	31
Figure 2-4. Combination therapy of TAX-Filomicelle and focused radiation improved survival rate of orthotopic brain tumor-bearing mice.....	32-33
Figure 3-1. Cytotoxicity of TAX-loaded nanobeads with different surface modifications.....	47
Figure 3-2. ‘Self’-peptide and human-CD47 enhance tumor imaging by Near-Infrared particles.....	48-49
Figure 3-3. Estimation of the beads number in tumor/spleen/blood 40 min after injection.....	50-51
Figure 3-4. Tumor shrinkage with TAX-loaded nanobeads with CD47 or ‘Self’ peptide.....	52
Figure 4-1. 3D-migration is sensitive to Lamin-A levels even in the absence of major proteomic changes	86-88
Figure 4-2. Lamin-A plasticizes nuclei, with persistent shape changes correlating with both 3D-migration sensitivity to Lamin-A and also with the Lamin-A:B ratio.....	89-90
Figure 4-3. Variations in Lamin-A lead to cell sorting in 3D-migration, consistent with Lamin-A:B regulation of nuclear response time	91-92
Figure 4-4. 3D-migration enhances apoptosis, and ablation of Lamin-A compromises HSP90-dependent, stress protection	93-95
Figure 4-5. Cells in the tumor periphery show low Lamin-A:B in more deformed nuclei, consistent with enhanced tumor growth after moderate knockdown of Lamin-A	96-98
Figure S4-1. Matrix-dictated Stiffness of Tumor Tissue	99-100
Figure S4-2. Moderate changes in Lamin-A do not affect 2D migration, but 2D migration always correlates positively with 3D migration	101-102
Figure S4-3. Cells with distinct origins and Lamin profiles demonstrate varied 3D migration sensitivity to Lamin-A change	103-104

Figure S4-4. siLMNA's with distinct targets consistently increase 3D migration without affecting viability in 2D or in migration thru large pores, but cell numbers are reduced with small pores and with knockdown	105-106
Figure S4-5. Extent of nuclear deformation by small pore migration shows cell-type specificity	107-108
Figure S4-6. Micropipette aspiration reveals Lamin-A dependence of nuclear stiffness and elasticity	109-110
Figure S4-7. Transient Lamin-A knockdown causes little change in nuclear volume ...	111-112
Figure S4-8. Mosin II-dependent A549 migration	113
Figure S4-9. Deep Lamin-A knockdown Induces up-regulation of pluripotency markers	114-115
Figure S4-10. Label-free mass spectrometry distinguishes human- and mouse-specific proteins	116

TABLE OF CONTENTS

ACKNOWLEDGMENT	III
ABSTRACT	VI
LIST OF TABLES	V
LIST OF ILLUSTRATIONS	VI
CHAPTER 1: INTRODUCTIONS	1
1-1. Tumor Shrinkage with Flexible Filomicelles	1
1-2. Enhanced Circulation via Avoidance of Immune Cell Clearance.....	3
1-3. Cell Migration and Cancer Progression	4
1-4. Nuclear Lamin Overview.....	5
1-5. Nuclear Mechanics.....	7
1-6. Thesis Overview.....	9
1-6. Reference	12
CHAPTER 2: Filomicells for Tumor Shrinkage	16
2-1. Introduction.....	16
2-2. Results and Discussion	19
2-3. Conclusions	21
2-4. Materials and Methods.....	22
2-5. Reference	34
CHAPTER 3: Enhanced Tumor Accumulation with Nanoparticle with CD47	37
3-1. Introduction.....	37

3-2. Results and Discussion	40
3-3. Conclusions	43
3-4. Materials and Methods.....	44
3-5. Reference	53
CHAPTER 4: LAMIN-A LEVELS LIMIT 3D-MIGRATION BUT PROTECT AGAINST MIGRATION-INDUCED APOPTOSIS.....	56
4-1. INTRODUCTION	56
4-2. RESULTS.....	58
4-3. DISCUSSION	70
4-4. CONCLUSIONS	76
4-5. SUPPLEMENTAL DISCUSSION	78
4-6. MATERIALS AND METHODS	80
4-7. REFERENCE.....	119
CHAPTER 5: CONCLUSIONS.....	127
5-1. LONG-CIRCULATING NANO-PARTICLES FOR CANCER THERAPIES	127
5-2. NUCLEAR PHYSICS OF CANCER CELLS AND TUMOR PROGRESSION	128

Chapter 1: Introduction

1-1. Tumor Shrinkage with Flexible Filomicelles

Delivering therapeutic agents specifically to tumor tissue is the ultimate goal in targeted therapeutics for cancer (Allen and Cullis, 2004). One important approach to this goal is to invent a nano-sized delivery carrier that has capabilities to load a cargo stably and to circulate in blood stream for extended period of time without losing the cargo until it reaches the target site. One of the most common types of nano-sized carrier studied is a self-assembled particle composed of amphiphilic co-polymers (Discher and Eisenberg, 2002; Kataoka et al., 2001). Amphiphilic copolymer is generally composed of hydrophilic (in most cases poly(ethylene glycol) or PEG) and hydrophobic segments, and can self-assemble in aqueous condition via hydrophobic interaction. Hydrophobic core of the self-assembled particle serves as a reservoir for various kinds of therapeutic reagents such as hydrophobic anti-cancer drug paclitaxel. Various kinds of chemical modifications are possible to improve the capabilities of delivery system, from conjugation of drug molecules to polymers via stimulus sensitive linkers for stable loading and controlled release of cargo (Ganta et al., 2008; Gupta et al., 2002), to modification of carrier surface with ligand molecules to increase specificity to target cells (Torchilin). Chemical modifications for the building polymer have been extensively studied, but recently a lot of attention has been paid to the shape (i.e. non-spherical shape) and physical properties for delivery carriers.

Sub-micron particles with non-spherical shape can be prepared by various methods such as physically deforming spherical particle to non-spherical shape (Champion and Mitragotri,

2006) or top-down lithography (Gratton et al., 2008). Previous works in Discher lab tried to prepare non-spherical particle by careful tuning of the molecular weight ratio of hydrophobic/hydrophilic segments in amphiphilic diblock copolymers so that the polymers can self-assemble into mainly three morphologies: conventional spherical micelles, spherical polymer vesicles or polymersomes and importantly cylindrical worm-like micelles or Filomicelles (Rajagopal et al.). Although depending on the chemical properties of comprising polymer's hydrophobic segment, it is possible to prepare Filomicelles with remarkable flexibility both in static condition and under flow. The flexibility and resulting vigorous movement of Filomicelles allow them to interact with phagocytic immune cells, which are responsible for the clearance of injected foreign material from blood circulation (discussed more in 1-2), for only a short time. Flexible Filomicelles showed surprisingly longer blood circulation time in comparison with spherical polymersome that also has PEG layer on surface (Geng et al., 2007).

Basic mechanism for the accumulation of injected particles in tumor tissue is diffusion through leaky walls of tumor vasculature and lack of clearance from the tumor tissue due to deficient lymphatic drainage, which are collectively called enhanced permeability and retention (EPR) effect (Maeda et al., 2000). Previous study showed that Filomicelle, which has 10~20 nm cross-section diameter, could permeate into porous hydrogel (Kim et al., 2005), while 100 nm spherical vesicle could not. Combined with the extended blood circulation time, it is reasonable to expect Filomicelles to show higher probability of eventually reaching the tumor tissue and interact with target cancer cells. Indeed, a model study showed that flexible 8 μm Filomicelles could successfully suppressed the growth of subcutaneous tumor, almost 2-fold higher efficiency than short 1 μm cylindrical micelle loaded with the same amount of anti-cancer drug paclitaxel.

1-2. Enhanced Circulation via Avoidance of Immune Cell Clearance

Long circulation of drug delivery carriers is beneficial in increasing the probability of the particles to go throughout the body, reaching organs that could have a tumor highly difficult to be removed by surgery. Biggest barrier for achieving long circulation is recognition and following clearance by immune cells such as macrophages in spleen and liver . PEG brush on the outer surface of many of self-assembled nano-particles can physically repel the attachment of various proteins in blood called opsonins, which can trigger the recognition and uptake by immune cells. However, most of the PEG-coated particles eventually get attached with those opsonin molecules ('opsonized,' see table 3-1) and cleared within time scale of hours to days from circulation. To maximize the therapeutic effect of drug-loaded delivery particles in a single injection, it is beneficial to add capabilities to (i) avoid the attachment of opsonin molecules by having PEG brush on surface, and (ii) to have a way to send a signal to immune cells to stop the process of uptake or phagocytosis.

Previous study from Discher lab showed that macrophages do not phagocytose particles in contact when nano to micron sized particles have a protein called CD47 on the surface (Tsai and Discher, 2008). CD47 is known to interact with receptor protein on macrophages called SIRP α , sending a signal to stop the myosin II-dependent contraction and the start membrane protrusion, which is an initial step for phagocytosis (Oldenborg et al., 2000). Few studies have aimed for achieving drug delivery system that can actively avoid the clearance by immune cells rather than only having PEG to prevent the opsonization. Therefore it is essential to investigate if CD47 can serve as a clearance-avoiding moiety on the surface of synthetic nano-particle in blood circulation as it did on red blood cell in mice.

1-3. Cell Migration and Cancer Progression

Cancer prognosis, or precise estimation of how quickly the disease progresses, is an essential part of cancer therapy. Motility of cancer cells can be an important indicator of tumor propagation, considering that in adult animals it underlies a wide range of critical processes, including tumor dissemination and stem cell homing. In the early stages of the “invasion-metastasis cascade” (Weinberg, 2007), cells in the tumor periphery crawl through surrounding extracellular matrix (ECM) and acquire space to divide, with some cells entering blood capillaries in metastasis to distant tissues. Successful migration requires cells to survive large distortions as they squeeze their way through ECM or across a basement membrane, and the largest single organelle in every cell is typically the nucleus, which tends to be stiff in many cell types (Lammerding et al., 2006; Pajerowski et al., 2007). In light of cytoskeletal-generated stresses in cell crawling, we hypothesized key roles for nuclear mechanics, which is largely determined by protein called Lamin-A,C as explained in detail in the next section, in 3D migration and cell survival.

Gradually accepted is the idea that cancer, of particular interest in this study, shows notable difference in Lamin-A,C profiles from healthy cells, depending on the disease type. The altered expression of Lamin-A,C in neoplastic cells is expected to be a promising biological marker for early diagnosis as well as key protein for disease progression. Mounting evidence suggests that different types of cancer cells have altered Lamin A/C expression levels, often leading to higher malignancy (Foster et al., 2010; Kaufmann et al., 1991). Recent reports have shown that stage II and III colon cancer tumors with low Lamin-A,C expression led to higher rates of disease recurrence (Belt et al., 2011). Contrarily, Lamin-A,C expression in squamous cell carcinoma, basal cell carcinoma and colorectal cancer positively correlated with its malignancy (Foster et al., 2010; Tilli et al., 2003). Thus current evidence for the involvement of Lamin-A,C in

cancer leads to contradicting conclusions, probably due to the complexity of interactions that involve Lamins.

1-4. Nuclear Lamin Overview

Nuclear Lamina is a protein meshwork residing right underneath the inner nuclear membrane. Main components of the meshwork are nuclear Lamins, which are grouped into two isoforms: A-type and B-type Lamins. Lamins are categorized as a type V intermediate filament (Shin et al.) protein, which is composed of α -helical coiled-coil rod domain flanked by head and tail domains like all the other IF proteins. The N-terminal globular head domain has a highly charged non- α -helical structure, whereas also highly charged tail domain at C-terminal is containing highly conserved 105 amino acid region with immunoglobulin (Ig)-fold structure as well as nuclear localization signal (Ben-Harush et al., 2009; Broers et al., 2006; Zastrow et al., 2004). Lamin molecules form a dimer by making coiled-coil structure in their rod domain, which serves as a fundamental building block for further polymerization into filamentous *head-to-tail* assembly. Two dimers associate together through electrostatic interaction in anti-parallel manner. This tetramer further polymerizes into a strand, eight of which eventually stack into a filament of 10 nm in diameter (figure 1-1).

A-type Lamins (Lamin-A, -C, -A Δ 10 and -C2) are found in most of differentiated cells with involvement in chromatin organization, transcription, translation, cell differentiation and many other functions (Andres and Gonzalez, 2009; Zastrow et al., 2004). Alternative splicing of mRNA of a single gene LMNA produces all A-type Lamin proteins (spliceforms), among which strong focus is placed on Lamin-A,C in this study. In addition to involvement in the various biological roles, Lamin-A,C makes remarkable contribution to the physical properties of cell

nucleus in expression depending manners (Pajerowski et al., 2007). The work furthermore measured increase of nuclear stiffness in the time course of differentiation in pluripotent human embryonic stem cells, which have initially undetectable Lamin-A,C level and increase the expression along differentiation pathway. Interestingly, not only reflecting the differentiation status, but Lamin-A,C expression (Swift. et. al.) and nuclear stiffness of various cells with distinct origins seems indicative of the tissue stiffness in which those cells reside. Underlining mechanism for strong correlation between nuclear and tissue stiffness could be the strong connection from extracellular environment to cell nucleus. Lamin-A,C is connected to the cytoskeleton (actin filaments, microtubules and cytoskeletal IFs) thorough the LINC (linker of nucleus and cytoskeleton) complex (Mejat and Misteli), thus making it a transducer of mechanical stimuli from the environment to the nucleus (Chancellor et al.). B-type Lamins, Lamin-B1 and -B2, are transcribed by separate genes, LMNB1 and LMNB2, respectively. Lamin-Bs are expressed in all types of cells in any developmental stage, and known to be involved in cell viability and tissue development but showing less obvious contribution to nuclear rigidity (Lammerding et al., 2006).

In addition to the significant influence of expression levels of Lamins on early development and maturation, particularly Lamin-A,C functions show surprising sensitivity against mutations. So far, over 200 different mutations in LMNA gene are reported, and the diseases derived from LMNA mutations are collectively called Laminopathies. Among Laminopathies with diverse disease phenotypes, Hutchinson-Gilford progeria syndrome (HGPS), which essentially causes premature aging, is especially intriguing. Lamin-A,C of HGPS patients possesses C-terminal farnesyl group, which is cleaved in the course of post-translational modifications, causing altered interactions between Lamin-A,C proteins and inner nuclear membrane. Due to this altered interaction, fibroblasts from HGPS patients showed notable phenotype of irregular nuclear morphology (Scaffidi and Misteli, 2006). Observation of HGPS

cell nuclei also supports the idea that Lamin-A,C is an important factor for nuclear morphology, and possibly the mechanics. Mutation in LMNBs is yet to be connected to any disease possibly due to the involvement of Lamin-Bs in cell viability.

1-5. Nuclear Mechanics

Nucleus experiences significant deformation while the cells is migrating through physically constraining environment (Friedl et al.). Once the cell is released from the constraints, the nuclear shape could go back to the relaxed state (ellipsoidal shape as usually observed in static culture) but with the rate dominated by the physical nature of the nucleus. In polymer physics, the all materials are categorized as viscoelastic. When a stress is applied to an ideal viscous material, the shape of the material slowly changes and the energy of the applied stress dissipates as the material perpetually deforms. In contrast, an ideal elastic material instantaneously responds to the stress applied. The energy from the stress is stored in the material, and shape will go back to the original one once the force application is ceased. When stress is applied to viscoelastic polymer material, part of the energy is stored but remaining part is consumed for terminal deformation. How quickly a polymer material responds to force or how quickly the material changes its shape back to the normal state after releasing stress depend on the balance of the extent of viscosity and elasticity.

To migrate through the transwell filter, cells require time scale of ~hours (figure 2-2C) with significant nuclear deformation in the circular column-shaped transwell pore. Terminal observation after 24 hours looks at the shape of nucleus that have had time scale of ~hours for turning back the shape to relaxed state in stress-free condition. Therefore, comparison of nuclear shape of cells on top (before migration) and bottom (after migration) sides of the transwell filter

should give the insight on how viscous/elastic the nucleus of particular cell line is. That is, cells with more viscous nucleus should greater difference in nuclear shape between two sides of the transwell membrane. The extent of nuclear shape change after migration is correlated first to the Lamin-A,C:B ratio to see if Lamin isoform dominance affects the viscoelastic nature of the cell nucleus, particularly under stress in long time scale (~hours).

For shorter time scale analysis of nuclear viscoelasticity, partial deformation induced by micropipette aspiration is suitable to measure the response time of nucleus against aspirating pressure. In micropipette aspiration experiments, nucleus of cytoskeleton-disrupted cells is put under constant negative pressure in glass needle. Under the pressure, the nuclear membrane extension into the glass pipette is monitored to evaluate the deformability of nucleus. As shown in previous work (Dahl et al., 2005; Pajerowski et al., 2007), physical property of nucleus is largely determined by nuclear Lamina, which is a meshwork structure composed of polymerized filament of Lamin molecules. As regular viscoelastic polymeric material, cell nucleus shows creep behavior in pipette under pressure, and creep compliance of the nuclear membrane under negative pressure can be calculated by

$$J(t) = (4\pi/3) \Phi (L/D) (1/\Delta P)$$

, where constant Φ is 2.1 (Theret et al., 1988), L is a length of nuclear membrane extension inside micropipette, D is an internal diameter of the pipette and ΔP is an applied aspiration pressure.

From nuclear creep compliance, one can calculate elastic stiffness of the nucleus:

$$E(t) = (\sin(\alpha\pi)/\alpha\pi) (1/J(t))$$

, where α is a power obtained by fitting nuclear compliance data to the power law.

1-6. Thesis Overview

One of the two main goals of this study is to validate the advantage of long circulating capability of the drug delivery carrier in two aspects: shape of the particle and ability to escape the immune cell clearance. In chapter 1, long circulating Filomicells with loaded drug was applied for the treatment of brain cancer cells. After basic characterization, the TAX-loaded Filomicelles were tested for tumor shrinkage in two distinct system: model subcutaneous tumors and orthotopic intracranial tumors. To overcome the strict physical barrier in brain vasculature wall, radiation therapy was combined to maximize the therapeutic effects of drug loaded Filomicelles. In the following chapter 2, the effect of CD47 attached on model particle was studied in the context of tumor accumulation and shrinkage. TAX-loaded particles with CD47 were tested for their cytotoxicity in vitro and for tumor shrinkage in vivo after visualization of enhanced tumor accumulation using hydrophobic near infrared dye loaded on those particles.

The second main goal of this thesis is to expand the understanding of Lamin-A/C roles in cell migration. First, the dependence of cell migration efficiency is explored in vitro using a technique called transwell migration assay, where cells are induced chemotactic migration through pores of certain sizes, with Lamin-A,C expression modified by genetic methods (RNA interference or overexpression). Three cell lines with distinct natures including origin, migration capacity and Lamin expression profile are tested to achieve broad understanding of the influence of Lamin-A/C on cell migration. Based on this observation, in-depth biophysical analyses of nuclei in the three cell lines are tried by applying basic viscoelastic model of polymer physics. Then, another aspect of nuclear Lamina in the context of cell migration was explored: the physical protection against migration-associated mechanical stress. In this part, one mechanism for resisting stress during cell migration process is revealed with the help of mass spectrometry.

Lastly the effect of Lamin-A,C knockdown in tumor propagation is explored using tumor xenograft, as a model study of in vivo function of Lamin-A,C.

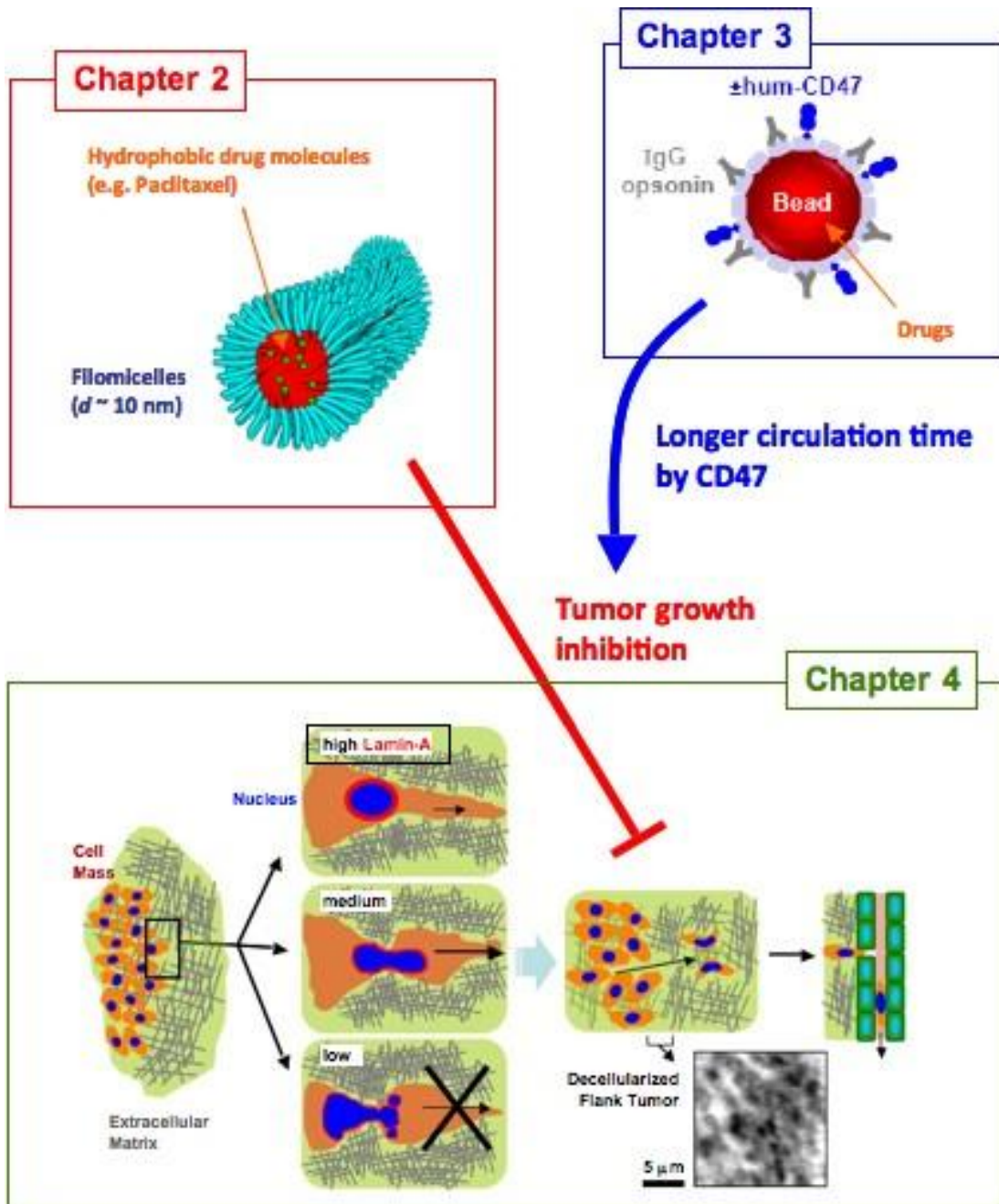


Figure 1-1. **Overview of the thesis** The main aims of this thesis is to obtain new insight into (i) how tumors can be effectively killed using synthetic drug delivery carrier and (ii) how the physical properties of individual cancer cells affect overall growth of tumor. In chapter 2, long-circulating drug delivery vehicle with unique morphology, Filomicelle, was tested for the use in treatment against brain tumor in conjunction with radiation. For the achievement of even longer circulation, the advantage of attaching CD47 on nano-particle was validated using various imaging techniques in chapter 3. Chapter 4 reveals important insight on how cell physics, particularly focusing on cell nuclear stiffness and flexibility, affects the cancer cell migration, which is important in many processes involved in cancer progression.

1-7. Reference

Allen, T. M. and Cullis, P. R. (2004). Drug delivery systems: entering the mainstream. *Science* **303**, 1818-22.

Andres, V. and Gonzalez, J. M. (2009). Role of A-type lamins in signaling, transcription, and chromatin organization. *J Cell Biol* **187**, 945-57.

Belt, E. J. T., Fijneman, R. J. A., van den Berg, E. G., Bril, H., Delis-van Diemen, P. M., Tijssen, M., van Essen, H. F., de Lange-de Klerk, E. S. M., Belien, J. A. M., Stockmann, H. B. A. C. et al. (2011). Loss of lamin A/C expression in stage II and III colon cancer is associated with disease recurrence. *European Journal of Cancer* **47**, 1837-1845.

Ben-Harush, K., Wiesel, N., Frenkiel-Krispin, D., Moeller, D., Soreq, E., Aebi, U., Herrmann, H., Gruenbaum, Y. and Medalia, O. (2009). The supramolecular organization of the *C. elegans* nuclear lamin filament. *J Mol Biol* **386**, 1392-402.

Broers, J. L. V., Ramaekers, F. C. S., Bonne, G., Ben Yaou, R. and Hutchison, C. J. (2006). Nuclear lamins: Laminopathies and their role in premature ageing. *Physiological Reviews* **86**, 967-1008.

Champion, J. A. and Mitragotri, S. (2006). Role of target geometry in phagocytosis. *Proc Natl Acad Sci U S A* **103**, 4930-4.

Chancellor, T. J., Lee, J., Thodeti, C. K. and Lele, T. Actomyosin tension exerted on the nucleus through nesprin-1 connections influences endothelial cell adhesion, migration, and cyclic strain-induced reorientation. *Biophys J* **99**, 115-23.

Dahl, K. N., Engler, A. J., Pajerowski, J. D. and Discher, D. E. (2005). Power-law rheology of isolated nuclei with deformation mapping of nuclear substructures. *Biophysical Journal* **89**, 2855-2864.

Discher, D. E. and Eisenberg, A. (2002). Polymer vesicles. *Science* **297**, 967-73.

Foster, C. R., Przyborski, S. A., Wilson, R. G. and Hutchison, C. J. (2010). Lamins as cancer biomarkers. *Biochemical Society Transactions* **38**, 297-300.

Friedl, P., Wolf, K. and Lammerding, J. Nuclear mechanics during cell migration. *Curr Opin Cell Biol* **23**, 55-64.

Ganta, S., Devalapally, H., Shahiwala, A. and Amiji, M. (2008). A review of stimuli-responsive nanocarriers for drug and gene delivery. *J Control Release* **126**, 187-204.

Geng, Y., Dalhaimer, P., Cai, S., Tsai, R., Tewari, M., Minko, T. and Discher, D. E. (2007). Shape effects of filaments versus spherical particles in flow and drug delivery. *Nat Nanotechnol* **2**, 249-55.

Gratton, S. E., Ropp, P. A., Pohlhaus, P. D., Luft, J. C., Madden, V. J., Napier, M. E. and DeSimone, J. M. (2008). The effect of particle design on cellular internalization pathways. *Proc Natl Acad Sci U S A* **105**, 11613-8.

Gupta, P., Vermani, K. and Garg, S. (2002). Hydrogels: from controlled release to pH-responsive drug delivery. *Drug Discov Today* **7**, 569-79.

Kataoka, K., Harada, A. and Nagasaki, Y. (2001). Block copolymer micelles for drug delivery: design, characterization and biological significance. *Adv Drug Deliv Rev* **47**, 113-31.

Kaufmann, S. H., Mabry, M., Jasti, R. and Shaper, J. H. (1991). Differential Expression of Nuclear-Envelope Lamin-a and Lamin-C in Human Lung-Cancer Cell-Lines. *Cancer Research* **51**, 581-586.

Kim, Y., Dalhaimer, P., Christian, D. A. and Discher, D. E. (2005). Polymeric worm micelles as nano-carriers for drug delivery. *Nanotechnology* **16**, S484-91.

Lammerding, J., Fong, L. G., Ji, J. Y., Reue, K., Stewart, C. L., Young, S. G. and Lee, R. T. (2006). Lamins A and C but not lamin B1 regulate nuclear mechanics. *Journal of Biological Chemistry* **281**, 25768-25780.

Maeda, H., Wu, J., Sawa, T., Matsumura, Y. and Hori, K. (2000). Tumor vascular permeability and the EPR effect in macromolecular therapeutics: a review. *J Control Release* **65**, 271-84.

Mejat, A. and Misteli, T. LINC complexes in health and disease. *Nucleus* **1**, 40-52.

Oldenborg, P. A., Zheleznyak, A., Fang, Y. F., Lagenaur, C. F., Gresham, H. D. and Lindberg, F. P. (2000). Role of CD47 as a marker of self on red blood cells. *Science* **288**, 2051-4.

Pajerowski, J. D., Dahl, K. N., Zhong, F. L., Sammak, P. J. and Discher, D. E. (2007). Physical plasticity of the nucleus in stem cell differentiation. *Proceedings of the National Academy of Sciences of the United States of America* **104**, 15619-15624.

Rajagopal, K., Mahmud, A., Christian, D. A., Pajerowski, J. D., Brown, A. E., Loverde, S. M. and Discher, D. E. Curvature-coupled hydration of Semicrystalline Polymer Amphiphiles yields flexible Worm Micelles but favors rigid Vesicles: polycaprolactone-based block copolymers. *Macromolecules* **43**, 9736-9746.

Scaffidi, P. and Misteli, T. (2006). Lamin A-dependent nuclear defects in human aging. *Science* **312**, 1059-1063.

Shin, J. W., Swift, J., Spinler, K. R. and Discher, D. E. (2011). Myosin-II inhibition and soft 2D matrix maximize multinucleation and cellular projections typical of platelet-producing megakaryocytes. *Proceedings of the National Academy of Sciences of the United States of America* **108**, 11458-11463.

Theret, D. P., Levesque, M. J., Sato, M., Nerem, R. M. and Wheeler, L. T. (1988). The application of a homogeneous half-space model in the analysis of endothelial cell micropipette measurements. *J Biomech Eng* **110**, 190-9.

Tilli, C. M. L. J., Ramaekers, F. C. S., Broers, J. L. V., Hutchison, C. J. and Neumann, H. A. M. (2003). Lamin expression in normal human skin, actinic keratosis, squamous cell carcinoma and basal cell carcinoma. *British Journal of Dermatology* **148**, 102-109.

Torchilin, V. P. Passive and active drug targeting: drug delivery to tumors as an example. *Handb Exp Pharmacol*, 3-53.

Tsai, R. K. and Discher, D. E. (2008). Inhibition of "self" engulfment through deactivation of myosin-II at the phagocytic synapse between human cells. *J Cell Biol* **180**, 989-1003.

Weinberg, R. A. (2007). *The biology of cancer*. New York: Garland Science.

Zastrow, M. S., Vlcek, S. and Wilson, K. L. (2004). Proteins that bind A-type lamins: integrating isolated clues. *J Cell Sci* **117**, 979-87.

Chapter 2: Filomicells for Tumor Shrinkage

Portion of this work contributes to Baumann *et. al.*, submitted.

In this chapter, anti-cancer drug-loaded polymeric micelle with worm-like shape, Filomicelle is tested for its therapeutic efficacy against glioblastoma multiforme, a type of brain tumor cells, both in vitro and in vivo. The objective of this chapter is to show the importance of long blood circulation for drug delivery carriers to achieve substantial tumor shrinkage. Orthotopic brain tumors represent one of the hardest tumor types to treat due to the physical blocking in their vascular walls. These tumors were treated with drug-loaded Filomicelles in combination with radiation therapy, which is known to disrupt the brain endothelium, to test if the capacity of long blood circulation is sufficient to treat brain tumors once the particles acquire the access to the tissue.

2-1. Introduction

Although showing strong cytotoxicity against cancer cells, many approved drugs have a problem in reaching target disease site such as solid tumor tissue, which results in still high mortality of cancer in general. Achieving delivery of anti-cancer drug molecules to target site with high specificity is a key to successful cancer therapy. Solid tumors often have leaky vascular systems with holes of 200-300 nm and have impaired blood flow compared to the circulation through normal tissue. Structural characteristics of tumor vascularity such as increased tortuosity, irregular shape and dilation of blood vessels coupled with endothelial fenestrations result in

leakage of blood plasma macromolecules and injected drugs into tumor tissue through molecular diffusion. The phenomenon of enhanced permeation of macromolecules, followed by retention and concentration of these macromolecules within tumor tissue due to deficient lymphatic drainage, is referred to as the enhanced permeability and retention (EPR) effect (Iyer et al., 2006; Luo and Prestwich, 2002). The EPR effect is the basis, for example, of preferential uptake of gadolinium contrast agents into tumors, compared to normal brain tissue, as observed by magnetic resonance imaging (MRI). The anatomical and physiological factors promoting the EPR effect that leads to increased intravasation of circulating molecules however are not uniformly distributed throughout tumors (Ewing et al., 2006; Muldoon et al., 2007). The EPR effect is often maximal at core regions within a tumor, regions frequently characterized by necrosis, while the EPR effect is diminished at the peripheral zones of a tumor. These peripheral areas may contain many viable cancer cells.

Over 20,000 Americans are diagnosed annually with glioblastoma multiforme (GBM). Standard treatment usually consists of surgery, radiation therapy (RT), and temozolomide chemotherapy, but median survival is only about 14.6 months (Stupp et al., 2005). Given these unsatisfactory results, new therapeutic approaches are clearly needed. Although other chemotherapeutic drugs such as paclitaxel are effective against GBM cells *in vitro*, they are clinically ineffective against GBM (Langer et al., 2001). The limited efficacy of such drugs has been attributed to an inability to achieve therapeutic concentrations of these drugs in the tumor due to the presence of the blood-brain barrier (BBB) – specifically the BBB within the tumor. Modulation of both drug delivery and the integrity of the BBB thus represent intriguing strategies for enhancing treatment efficacy.

A novel approach to maximize EPR-driven concentration of chemotherapeutic agents within tumors is utilization of drug-loaded nanocarriers (DLNs) that stably incorporate drug

molecules and thereby minimize both excretion and generic permeation in healthy tissues. Filomicelles are one type of recently developed DLN, composed of amphiphilic diblock copolymer that can self-assemble through hydrophobic interaction into filamentous particle, with capability incorporate hydrophobic molecules including widely variety of anti-cancer drugs in its hydrophobic core. Filomicelles avoid rapid clearance by the mononuclear phagocytic system (MPS) of the liver and spleen through outer poly(ethylene glycol) (PEG) layer physically repelling the attachment of opsonin molecules, resulting in increased serum half-life and maximal drug delivery to subcutaneous tumor xenografts with improved anti-tumor efficacy (*Geng et al., 2007*). Flexibility of the filaments was also shown to be important to circulate through blood stream crowded with blood cells, and the crystalline rigidity of past polymer assemblies is suppressed here with novel hydrophilic-*linked*-hydrophobic block copolymers of poly(ethylene oxide)-*block*-poly(ϵ -caprolactone-*random-D,L*-lactide) (OCLA), that randomize the packing in the hydrophobic, polyester core. Filomicelles have been shown to even flow through the brain vasculature, but like other DLN they do not permeate the BBB (*Christian et al., 2009*). Therefore disruption of the BBB might enhance the effectiveness of DLNs for treating intracranial tumors. Conventional approaches for disrupting the BBB transiently before delivery of chemotherapy, such as efflux transporter inhibitors, bradykinins, and intra-arterial infusions of osmotic disruption agents (e.g. mannitol) lack specificity against tumor-associated vasculature, which can potentially result in serious side effects (*Doolittle et al., 2000; Guillaume et al.; Jahnke et al., 2006; Neuwelt et al., 2008*). In contrast, targeted radiation therapy (RT) offers an ideal solution for focally disrupting the tumor BBB and avoiding normal brain (*Cao et al., 2005; Deeken and Loscher, 2007; Lemasson et al.*).

In this chapter, filomicelles are studied for the delivery of model drug paclitaxel (TAX), which is a widely used anti-cancer agent against many different types of cancer including breast,

ovarian and lung cancer (Rowinsky and Donehower, 1995). Basic characterization of drug loading and release is followed by in vitro toxicity assay and in vivo tumor shrinkages studies. Therapeutic efficacy of TAX-loaded Filomicelle was tested against two tumors models: subcutaneous and intracranial tumors. Combination therapy of TAX-Filomicelle and Radiation was tested against intracranial tumors, which requires the penetration of drug-loaded particles through BBB in brain tissue vascular walls.

2-2. Results and Discussion

2-2-1. Paclitaxel-loaded Filomicelles Effectively Kills Glioblastoma

To efficiently deliver therapeutic agents to target sites, DLNs need to avoid interaction with MPS and physical trap in tissues (Geng et al., 2007). Our Filomicelles are composed of novel diblock copolymer OCLA, forming PEGylated outer layer for the particle to avoid opsonization or binding of certain groups of proteins, which eventually causes immune recognitions. In addition to the “stealth” property by PEG, it also essential for Filomicelles to retain flexibility to crawl through crowd of circulating cells in blood vasculature. The hydrophobic core of the OCLA polymer is composed of random copolymer of ϵ -caprolactone and *D,L*-lactide, both of which are FDA-approved materials, to inhibit the crystal structure formation of Poly(caprolactone) that happened with our previous Filomicelle studies with PEG-*b*-Poly(ϵ -caprolactone).

OCLA polymers successfully form long filomicelles with average length of 12.5 μm (Fig. 2-1A and B), and can be loaded with widely used anti-cancer drug paclitaxel (TAX), which binds to microtubule to cause failure in mitosis and eventually growth arrest and apoptosis. TAX

molecules loaded in the core of Filomicelles go through two distinct phases of release from the carrier, showing burst release over first 1 hour followed by sustained release.

Paclitaxel-loaded filomicelles were tested for in vitro cytotoxicity against glioblastoma cells, as well as polymersomes with different concentration of salts in their aqueous lumen, mixture of short cylinders/spherical micelles (OCL3) and free drug control (Fig. 2-2A). Increased salt concentration was loaded in polymersome lumen to see if release of the excess salts inside endosome can cause the rupture of the lipid vesicle membrane due to osmotic pressure. 48-hour treatment with TAX-loaded formulations resulted in very similar IC50 values for all the tested particles, giving $< 0.1 \mu\text{g/mL}$ for two glioblastoma lines U251 and SF767. For T98G cell line (Fig. 2-2B), OCLA2-12 derived filomicelles showed the highest therapeutic effect, even > 4 -fold higher than free drug control. Interestingly, polymersomes from OCLA2-7.5 containing 2-fold higher salt concentration than physiological condition showed increased cytotoxicity effect against 2 (out of 3) tested cell lines.

2-2-2. Paclitaxel-loaded Filomicelles Effectively Shrank Glioblastoma-derived *Subcutaneous* Tumors, but Combination Therapy with Radiation is required for Intracranial Tumor Shrinkage

Since U251 cells showed high sensitivity against TAX-treatment and stable tumor growth in nude mice, subcutaneous tumor was established with U251 cells to evaluate the in vivo therapeutic efficacy of TAX-loaded Filomicelles. Treatment with TAX-loaded Filomicelles successfully suppressed the subcutaneous tumor growth for over 4 weeks (Fig. 2-3).

As aforementioned, crossing through BBB is an essential step for drug delivery into a brain tumor. Although flexible Filomicelles showed blood circulation long enough to reach brain

vasculature, they fail to intravasate into surrounding tissues due to BBB's tight regulation of material transport as previously shown with near-infrared dye-loaded Filomicelles localized in the blood vessel 24 hours after administration. Considering the previous work showing disruption of BBB including vasculature in brain tumor tissue by radiation therapy (Cao et al., 2005), we hypothesized that radiation-induced disruption of the BBB might enhance retention of vascular-delivered therapeutic reagents within the targeted tumor tissue. As a proof of principle, it was shown that TAX-loaded Filomicelle itself could not suppress the growth of GBM-derived tumor in brain tissue (intracranial tumor) (Fig. 2-4A), whose cells can be killed by the drug-loaded particles when they form a tumor in subcutaneous tissue. Only when combined together, Filomicelles with highest possible TA loading and focused radiation against brain tumor tissue could suppress the intracranial tumor growth and increased survival of the tumor-bearing mice (Fig. 2-4B)).

2-4. Conclusions

Flexible Filomicelles composed of novel amphiphilic diblock copolymer OCLA is shown to be an effective delivery vehicle for widely used chemotherapeutic Paclitaxel (TAX), and resulting drug delivery system successfully suppressed the tumor growth at flank sites where tumor tissue is composed of leaky vasculature and therefore holds EPR effect. The issue of poor therapeutic effect by TAX-loaded Filomicelles against intracranial tumor due to physical block of BBB can be overcome by directly disrupting the BBB by focused radiation therapy. The presented results here successfully show extended survival of intracranial tumor-bearing mice. Although detailed study with complete set of controls is required, combination therapy of drug-loaded nanoparticles and radiation therapy represents a promising treatment for still detrimental brain cancer.

2-4. Materials and Methods

Cells

Human lung carcinoma A549 cells were purchased from ATCC (Manassas, VA) and cultured using Ham's F-12 medium (Invitrogen) supplemented with 10% fetal bovine serum (FBS, Sigma) and 1% penicillin/streptomycin (P/S, Invitrogen) at 37 °C with 5% CO₂. Human glioblastoma multiforme (GBM) U251 cells were kind gift from Dr. Jay Dorsey's lab at Radiology department of the University of Pennsylvania. U251 cells are grown in high glucose DMEM with 10% FBS.

Polymer Synthesis and Characterizations

Amphiphilic di-block copolymer denoted as OCLA corresponds to poly(ethylene glycol)-

block-poly(ϵ -caprolactone-*random-D,L*-lactide) (PEG45-*b*-P(CL92-*r*-LA21)), where the subscript for each polymer block indicates the degree of polymerization of respective blocks. In terms of molecular weights, PEG MW is 2000 and the polyester block is 12,000 g/mol, denoted as OCLA. Copolymers were synthesized by standard ring opening polymerization of ϵ -caprolactone and *D,L*-lactide monomer using MePEO (2000 g/mol) as initiator and stannous octoate as catalyst. Briefly, freshly distilled ϵ -caprolactone (2.19 g, 1.92 x 10⁻² M), *D,L*-lactide (0.312 g, 2.15 x 10⁻³ M) and Me-PEO (2000 g/mol) (0.4166 g, 2.17 x 10⁻⁵ M) calculated based on the desired PEO45-*b*-P(CL92-*r*-LA21) block ratio and stannous octoate (15 mg, 3.7 x 10⁻⁵ M) were taken in a previously flamed, argon -purged glass ampule (10 mL). The ampule with reactants was further argon -purged for a few minutes, vacuumed for 15-20 minutes to eliminate the trace amount of moisture and sealed under vacuum. The polymerization reaction was allowed to proceed for 6

hours at 140 °C in oven. The reaction was terminated after cooling the ampule to room temperature.

The newly synthesized OCLA polymer was assessed from ¹H NMR spectra obtained from a Bruker NMR360 spectrometer using deuterated chloroform (CDCl₃) as solvent. The molecular weight distribution of the synthesized polymer was determined by gel permeation chromatography using a Waters GPC system equipped with a Waters 1215 binary pump and Waters 2414 refractive-index detector. Separation was performed using Styragel HR2 column, calibrated with polystyrene standards and tetrahydrofuran as solvent.

Filomicelle preparation and paclitaxel loading

A solvent evaporation method was then used to generate the filomicelles, which were combined with paclitaxel in methanol, dialyzed against PBS and filtered by extrusion to remove any paclitaxel aggregates to thus generate the drug-loaded nanocarrier formulation. Detailed information on the synthesis, purification, and analysis of the paclitaxel-loaded nanocarrier is provided in the Supplemental Section. For DLN preparation, the polymer concentration was 4 mg/ml and paclitaxel was added to achieve polymer/paclitaxel ratio (w:w) of 20:1. HiDLN started with 20 mg/ml with paclitaxel added to 32:1. Increased addition of paclitaxel does not lead to better loading because of precipitation of polymer and paclitaxel.

Paclitaxel quantitation in Formulations

A Shimadzu HPLC system (Shimadzu Corporation, Japan) equipped with an inline DGU-

20A3 vacuum degasser, LC-20AB binary high pressure pump, SIL-20AC high speed autosampler and a pinnacle® DB C18 reverse-phase column (4.6 Å~ 150 mm) was used to detect and quantify paclitaxel in worm formulation. Briefly, 20 µL of sample was injected to the HPLC system and eluted by a mobile phase consisting of acetonitrile and water with 0.1% of trifluoroacetic acid at a flow rate of 1 ml/min at 35 °C. In gradient elution, the starting acetonitrile concentration was 50% and increased to 60% within 15 min at a constant rate. The detection was performed at $\lambda=228$ nm and quantified using a diode array detector (SPD M20A, Shimadzu). A standard curve was prepared from paclitaxel at concentration of 0.002, 0.01, and 0.05 mg/ml. Data was acquired and processed with LC solution chromatography software from Shimadzu Corporation. Paclitaxel - loaded OCLA worm micelles was mixed with acetonitrile and water at a ratio of 50:50 to break the micelle structure and solubilize the paclitaxel followed by the HPLC analysis using the standard curve described above.

In vitro cytotoxicity assay

24 hours prior to starting TAX treatment, 5000 glioblastoma cells were seeded into wells of 96-well plate (Corning). Dilution series of Fillomicells, polymersomes and free TAX drug were added to wells and incubated at 37 °C with 5% CO₂ for 48 hours. Cell viability was tested using conventional MTT assay. Briefly, cells were incubated at 37 °C with 5% CO₂ for 4 hours after adding 20 µL of 5 mg/mL Thiazolyl Blue Tetrazolium Bromide (Sigma) to 100 µL of cell solution. After discarding the solution, 100 µL DMSO was added to dissolve crystal of reduced Thiazolyl Blue Tetrazolium Bromide. After incubation on a rocker at room temperature, absorbance at 565 nm was read corresponding to the number of viable cells in a well.

Flank and Intracranial tumor establishment

Mice were injected subcutaneously with U251 cells with firefly luciferase gene at a site superficial to the scapulae bilaterally and superficial and medial to the hip joints bilaterally. The mice were anesthetized with an IP injection of ketamine/xylazine at a dose of 140mg/kg and 10mg/kg respectively and then placed on their stomach with their limbs symmetrically arranged such that their feet are pointed cephalad. Once the mouse was sufficiently anesthetized so that no response was elicited from a light pinch of the rear foot, the site of injection was cleaned with alcohol. Using aseptic technique, an injection of 100 microliters of a cell suspension containing 2×10^6 tumor cells along with DMEM media was administered using a 26 gauge 5/8" needle into each site. No closure was necessary.

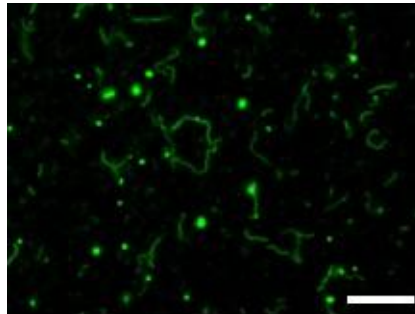
In vivo treatment of GBM-derived tumors with TAX-loaded Filomicelles

In experiments to test the efficacy of paclitaxel-loaded nanobiopolymer combined with fractionated radiation therapy, DLN was given as a 1 mL intraperitoneal (IP) injection every other day for 17 days. Mice received up to 29% of the daily maximum tolerated dose (MTD) of IP paclitaxel (Kozler and Pokorny, 2003; Weissleder and Pittet, 2008), or 5.89 mg/kg, per treatment. For tumor evaluation, the fully anesthetized mice received a subcutaneous injection of 60 microliters of pharmaceutical-grade D-luciferin (50 mg/mL). Imaging via the IVIS Lumina II bioluminescence imaging system system commenced at 5 minutes after the luciferin injection. The mice were repeatedly imaged over a span of 30 minutes to determine the maximum luminescence intensity in photons/second, a surrogate marker for the size of the tumor(s). A volume of interest (VOI) was drawn around each tumor and a background VOI was drawn on the

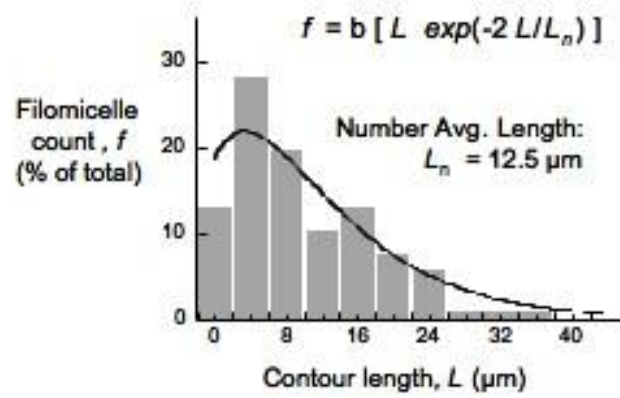
animal in an area known to be free of tumor to generate a background corrected bioluminescence flux value for each tumor at each given time point.

Focused radiation was applied against mice in a custom-made plastic mouse bed equipped with a stereotactic head immobilizer that integrates with the Small Animal Radiation Research Platform (SARRP) (Xstrahl, Surrey, United Kingdom). The anatomy of the skull and brain was calibrated via the onboard cone-beam CT. The location of the tumor was determined by bioluminescent imaging, and the skull was tattooed to define the beam location. Radiation was administered as four daily fractions of 3 Gy each with a rate of 0.1 Gy/min after anesthesia with ketamine/xylazine at a dose of 140 mg/kg and 10mg/kg, respectively. All these techniques helped ensure day-to-day reproducibility and allowed optimally precise radiation therapy. Mice were given 1 mL IP injections every other day for 34 days (17 total treatments) beginning on day 1 of radiation. TAX dosage corresponds to 48% of the daily MTD of intraperitoneal paclitaxel, or 9.55 mg/kg per treatment. This dose was roughly equivalent to 42% of the MTD given to human GBM patients undergoing concurrent treatment with free paclitaxel and RT.

A



B



C

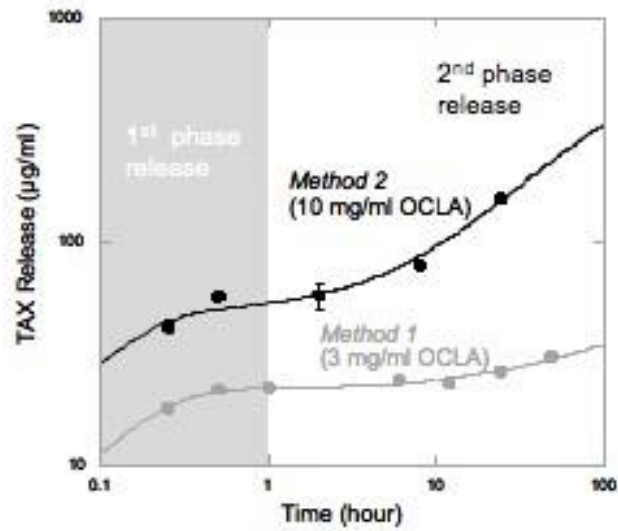
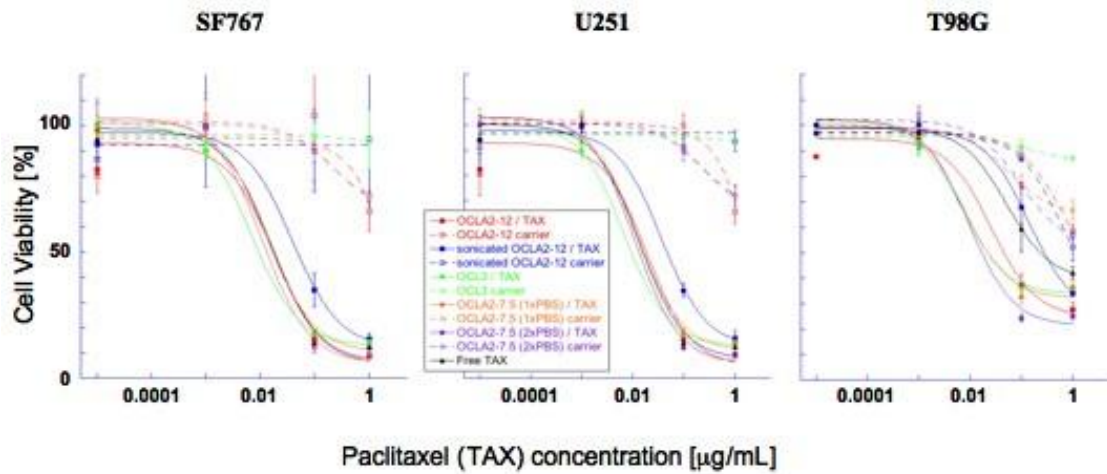


Figure 2-1. **Basic characterization of Filomicelles**

Representative fluorescence microscopy snapshot of wormlike filomicelles made with OCLA and labeled with fluorescent dye. Scalebar 10 µm. (C) Contour length distribution of several hundred OCLA (2, 12) Filomicelles. (D) Taxol loading and release by two different methods fitted with two first order functions for a burst release phase.

A



B

Formulations	IC ₅₀ ± S.E. [µg/ml]		
	SF767	U251	T98G
OCLA2-12	0.063 ± 0.004	0.065 ± 0.005	0.079 ± 0.0004
sonicated OCLA2-12	0.062 ± 0.015	0.074 ± 0.003	0.338 ± 0.240
OCL3	0.051 ± 0.005	0.064 ± 0.009	0.459 ± 0.382
OCLA2-7.5 1xPBS	0.058 ± 0.003	0.066 ± 0.005	1.441 ± 1.369
OCLA2-7.5 2xPBS	0.034 ± 0.023	0.067 ± 0.010	0.086 ± 0.015
Free TAX	0.070 ± 0.011	0.064 ± 0.005	0.340 ± 0.250

Figure 2-2. Summary of cytotoxicity assay with TAX-loaded polymer formulations with distinct morphologies

(A) Three cell lines of glioblastoma were incubated with various TAX-loaded polymer formulations with distinct shapes: spherical micelles, polymersomes and Filomicelles as well as

unloaded carriers. IC50 was measured using the fitting curve and summarized in (B).

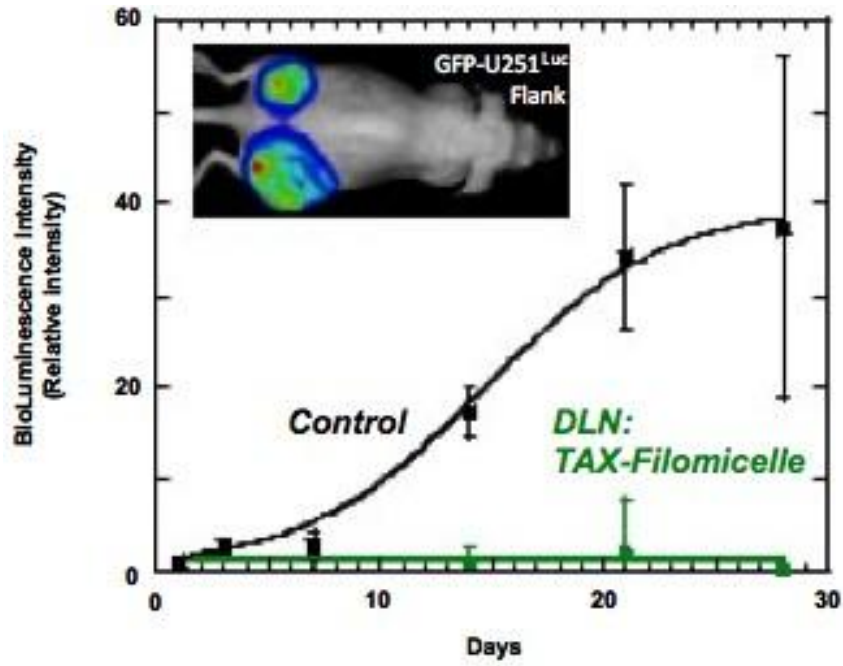
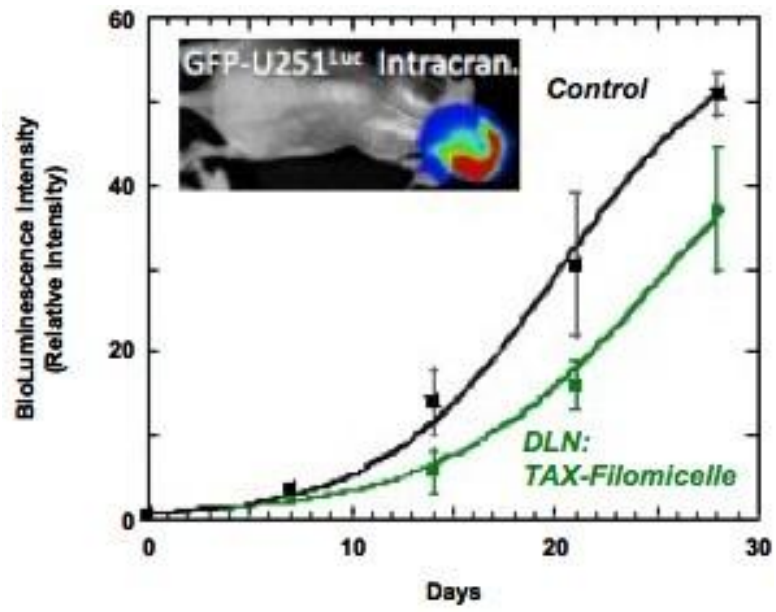


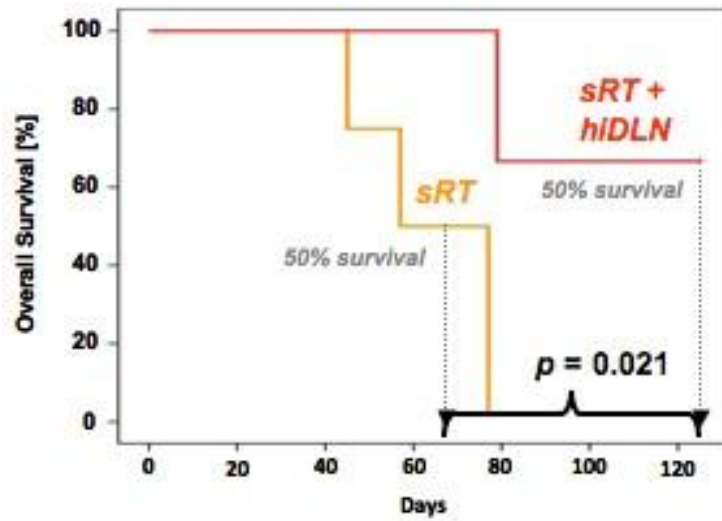
Figure 2-3. Tumor shrinkage with TAX-loaded Filomicelles

Nude mice with two flank tumors made of U251 cells were treated with TAX-loaded Filomicelles over a month when the treatment completely suppressed the growth of tumors.

A



B



Treatment Group	Median Survival	Mean Survival
sRT + hiDLN	125*	110*
sRT	57	64

Figure 2-4. **Combination therapy of TAX-Filomicelle and focused radiation improved survival rate of orthotopic brain tumor-bearing mice**

(A) Unlike the case with tumors in subcutaneous tissue, TAX-loaded Filomicelles almost failed to cure the mice with intracranial tumors, which requires circulating particles to cross over blood brain barrier in brain endothelia for effective treatment. (B) Graph showing overall survival of mice with brain tumors that received treatment with optimized radiation therapy techniques alone (“sRT”) or sRT in conjunction with higher dose DLN (“hiDLN”) incorporating paclitaxel. The table below lists the median and mean survival of each group of treated mice. The combined DLN and optimized radiation therapy techniques resulted in significantly improved mean and median survival compared to mice receiving the radiation therapy alone ($p < 0.05$). (* Most of the mice treated with combined hiDLN and sRT remained alive, in excellent condition, gaining weight, and with no detectable tumor, and thus have not yet reached maximal survival. Therefore, the listed median and mean survivals for “sRT + hiDLN” are those calculated at the end of 120 days).

2-5. Reference

Cao, Y., Tsien, C. I., Shen, Z., Tatro, D. S., Ten Haken, R., Kessler, M. L., Chenevert, T. L. and Lawrence, T. S. (2005). Use of magnetic resonance imaging to assess blood-brain/blood-glioma barrier opening during conformal radiotherapy. *J Clin Oncol* **23**, 4127-36.

Christian, D. A., Cai, S., Garbuzenko, O. B., Harada, T., Zajac, A. L., Minko, T. and Discher, D. E. (2009). Flexible filaments for in vivo imaging and delivery: persistent circulation of filomicelles opens the dosage window for sustained tumor shrinkage. *Mol Pharm* **6**, 1343-52.

Deeken, J. F. and Loscher, W. (2007). The blood-brain barrier and cancer: transporters, treatment, and Trojan horses. *Clin Cancer Res* **13**, 1663-74.

Doolittle, N. D., Miner, M. E., Hall, W. A., Siegal, T., Jerome, E., Osztie, E., McAllister, L. D., Bubalo, J. S., Kraemer, D. F., Fortin, D. et al. (2000). Safety and efficacy of a multicenter study using intraarterial chemotherapy in conjunction with osmotic opening of the blood-brain barrier for the treatment of patients with malignant brain tumors. *Cancer* **88**, 637-47.

Ewing, J. R., Brown, S. L., Lu, M., Panda, S., Ding, G., Knight, R. A., Cao, Y., Jiang, Q., Nagaraja, T. N., Churchman, J. L. et al. (2006). Model selection in magnetic resonance imaging measurements of vascular permeability: Gadomer in a 9L model of rat cerebral tumor. *J Cereb Blood Flow Metab* **26**, 310-20.

Geng, Y., Dalhaimer, P., Cai, S., Tsai, R., Tewari, M., Minko, T. and Discher, D. E. (2007). Shape effects of filaments versus spherical particles in flow and drug delivery. *Nat Nanotechnol* **2**, 249-55.

Guillaume, D. J., Doolittle, N. D., Gahramanov, S., Hedrick, N. A., Delashaw, J. B. and Neuwelt, E. A. Intra-arterial chemotherapy with osmotic blood-brain barrier disruption for aggressive oligodendroglial tumors: results of a phase I study. *Neurosurgery* **66**, 48-58; discussion 58.

Iyer, A. K., Khaled, G., Fang, J. and Maeda, H. (2006). Exploiting the enhanced permeability and retention effect for tumor targeting. *Drug Discov Today* **11**, 812-8.

Jahnke, K., Doolittle, N. D., Muldoon, L. L. and Neuwelt, E. A. (2006). Implications of the blood-brain barrier in primary central nervous system lymphoma. *Neurosurg Focus* **21**, E11.

Kozler, P. and Pokorny, J. (2003). Altered blood-brain barrier permeability and its effect on the distribution of Evans blue and sodium fluorescein in the rat brain applied by intracarotid injection. *Physiol Res* **52**, 607-14.

Langer, C. J., Ruffer, J., Rhodes, H., Paulus, R., Murray, K., Movsas, B. and Curran, W. (2001). Phase II radiation therapy oncology group trial of weekly paclitaxel and conventional external beam radiation therapy for supratentorial glioblastoma multiforme. *Int J Radiat Oncol Biol Phys* **51**, 113-9.

Lemasson, B., Serduc, R., Maisin, C., Bouchet, A., Coquery, N., Robert, P., Le Duc, G., Tropres, I., Remy, C. and Barbier, E. L. Monitoring blood-brain barrier status in a rat model of glioma receiving therapy: dual injection of low-molecular-weight and macromolecular MR contrast media. *Radiology* **257**, 342-52.

Luo, Y. and Prestwich, G. D. (2002). Cancer-targeted polymeric drugs. *Curr Cancer Drug Targets* **2**, 209-26.

Muldoon, L. L., Soussain, C., Jahnke, K., Johanson, C., Siegal, T., Smith, Q. R., Hall, W. A., Hynynen, K., Senter, P. D., Peereboom, D. M. et al. (2007). Chemotherapy delivery issues in central nervous system malignancy: a reality check. *J Clin Oncol* **25**, 2295-305.

Neuwelt, E., Abbott, N. J., Abrey, L., Banks, W. A., Blakley, B., Davis, T., Engelhardt, B., Grammas, P., Nedergaard, M., Nutt, J. et al. (2008). Strategies to advance translational research into brain barriers. *Lancet Neurol* **7**, 84-96.

Rowinsky, E. K. and Donehower, R. C. (1995). Paclitaxel (taxol). *N Engl J Med* **332**, 1004-14.

Stupp, R., Mason, W. P., van den Bent, M. J., Weller, M., Fisher, B., Taphoorn, M. J., Belanger, K., Brandes, A. A., Marosi, C., Bogdahn, U. et al. (2005). Radiotherapy plus concomitant and adjuvant temozolomide for glioblastoma. *N Engl J Med* **352**, 987-96.

Weissleder, R. and Pittet, M. J. (2008). Imaging in the era of molecular oncology. *Nature* **452**, 580-9.

Chapter 3: Enhanced Tumor Accumulation with Nanoparticle with CD47

Portion of this work contributes to Rodriguez *et. al.*, submitted.

In this chapter, the surface of polystyrene beads is modified to achieve longer blood circulation with integrin-associated protein called CD47. CD47-attached beads with hundreds of nanometer in size were loaded with anti-cancer drug paclitaxel (TAX), and the drug-loaded particle was tested first for in vitro cytotoxicity against human lung carcinoma A549. A549 cell was injected into immune-deficient mouse, whose spleen-derived immune cells can still recognize human CD47, to establish subcutaneous tumor. TAX-loaded polystyrene beads with CD47 or CD47-derived peptide were injected into tumor bearing mice for testing their capability to suppress the tumor growth. Anti-tumor effect of our modified beads was compared with the conventional formulation of Cremophor EL.

3-1. Introduction

Macrophages engulf invading microbes and dying cells in a highly coordinated and active process that evolved over eons and occurs also now in foreign body responses to injected particles and implants. This clearance function of phagocytes is delayed but not eliminated by dense 'Stealth' brushes such as with polyethylene glycol (PEG) on circulating nanoparticles and liposomes used in therapeutics and imaging (Bartlett et al., 2007; Klibanov et al., 1991; Photos et al., 2003). Coating with PEG of (<500 nm) indeed helps to delay rapid clearance and to thereby provide

more time for circulation through disease sites such as tumors, but neither PEG nor targeting groups stops the adsorption of serum proteins such as IgG (Table S3-1) nor the subsequent clearance of particles from the circulation by macrophages in the spleen and liver (Bartlett et al., 2007; Klibanov et al., 1991; Photos et al., 2003; Rossin et al., 2008; Turk et al., 2004). Delivery to disease sites can also be limited by phagocytic uptake by tumor-associated macrophages for example (Turk et al., 2004), and the acquired immunity to foreign polymers has become an additional concern (Armstrong et al., 2007). In contrast, ‘self’ cells and tissues are in constant contact *with* and well-tolerated *by* macrophages, which has suggested critical mechanisms of self recognition. Here we describe a reductionist approach to a synthetic but humanized ‘Active Stealth’ peptide that specifically binds and signals ‘Self’ to phagocytes in blocking clearance of particles as small as viruses.

CD47 glycoprotein is a putative ‘Marker of Self’ (Oldenborg et al., 2000) normally expressed on all cell membranes in humans, mice and other higher organisms (Bentley and Adams), and it often associates in *cis* with integrins (Brown and Frazier, 2001) and in other *species-specific*, immunogenic macrocomplexes on cells (Bruce et al., 2003; Mouro-Chanteloup et al., 2003; Subramanian et al., 2006). Mouse knockouts of CD47 (mCD47) are surprisingly viable, but when red blood cells from these mice (mRBCs) are injected into the circulation of control mice, the deficient cells are cleared within hours by macrophages of the spleen compared to normal mRBC that circulate for weeks (Oldenborg et al., 2000). CD47’s extracellular domain interacts with CD172a (SIRP α : Signal Regulatory Protein α) on phagocytes (Brown and Frazier, 2001), and the binding proves species-specific (Subramanian et al., 2006) in part because SIRP α is highly polymorphic within a species (Takenaka et al., 2007). Indeed, NOD.SCID strains of mice happen to express one variant of mouse-SIRP α that cross-reacts with human-CD47, which explains why *human* hematopoietic cells engraft and circulate in NOD.SCID better than any other

mouse strain (Strowig et al.; Takenaka et al., 2007). *In vitro*, the CD47-SIRP α interaction inhibits mouse macrophage uptake of antibody-coated mRBCs (Oldenborg et al., 2000) as well as human macrophage uptake of both human-RBC and human-CD47 (hCD47)-coated microparticles (Tsai and Discher, 2008).

Minimizing the 117 amino acid, recombinant hCD47 domain to a binding site peptide could provide, we thought, the clearest evidence that binding and signaling of hCD47 to mSIRP α is the molecular mechanism of inhibition *in vivo*. Our first guess design was a 21 amino acid ‘Self’-peptide, which was simulated for stability and then synthesized with the aims of (i) minimizing species specificity (Subramanian et al., 2006), (ii) eliminating the glycosylation of CD47 that impedes binding (Subramanian et al., 2007), and (iii) developing Scrambled, inactive peptides. Biotinylation on an amino-terminal PEG linker provided a means of attachment to Streptavidin-beads for *in vivo* studies.

We address whether human-CD47 and a synthetic ‘Self’ peptide on such small particles can minimize phagocytic uptake and thereby enhance delivery to tumor *in vivo* here using NOD.SCID/Il2rg^{-/-} mice (NSG). TAX was loaded into the sub-micron polystyrene particles modified with human-CD47 or ‘Self’ peptide on surface. Extended blood circulation of the particles with CD47 or ‘Self’ peptide is expected to lead increased tumor accumulation due to EPR effect. Therefore those particles were tested for *in vitro* cytotoxicity and *in vivo* tumor shrinkage using subcutaneous tumor model. Our reductionist approach eliminates confounding, biological factors on cell membranes (eg. integrins), and the results with a minimal ‘Self’ peptide constitute a first example of a synthetic, human ligand that binds and signals to phagocyte receptors to passivate macrophages.

3-2. Results and Discussion

3-2-1. CD47 Enhances Tumor Accumulations of the Opsonized Particles In Vivo

Polystyrene beads were pre-labeled with hydrophobic near infrared dye (DiR) to enable non-invasive detection of particles in mice at different time points after injection. Since NSG mouse cannot produce immunoglobulin (Friedl et al.), which is one of the most common opsonin (table 3-1), the beads with strept-avidin coating on the surface was always attached with anti-avidin antibodies to mimick the opsonized state. Opsonized beads was injected into NSG mice in the presence of CD47 or ‘Self’ peptide also on the surface to see if those beads could result in increased tumor accumulation compared to beads with only IgG. Although still large part of the injected beads trapped in spleen and liver (Fig. 3-2A), CD47 and ‘Self’ peptide enhanced the tumor accumulation in the similar level. As early as 10 min after tail vein injection of nanoparticles, CD47- and ‘Self’ peptide-attached beads gave mean tumor intensities 2-fold above those of non-injected mice while control beads gave background-level signal (Fig. 3-2B). With CD47- and ‘Self’ peptide beads, the fluorescence at every time point is significantly higher than control beads ($p < 0.05$), and the increase fits to first order kinetics ($\tau = 52$ min), consistent with enhanced perfusion that is limited by progressive clearance. Notably, at 40 min, both CD47- and ‘Self’ peptide beads give ~10-20 fold higher signals than controls.

Tumors and other major organs in one experiment were subsequently excised at 35 min post-injection and imaged in order to remove background from nearby tissue in the region-of-interest (Fig. 3-2C). The ‘Self’-beads and CD47-beads show 16- to 22-fold enhancement above the very low signals obtained with control opsonized beads, with no statistical difference between ‘Self’-peptide and hCD47. The fraction of nanobeads in the blood within the tumor is small (Fig. 3-2C, inset), and so the majority of signal derives from beads that have accumulated in the tumor,

most likely by Enhanced Permeation and Retention (EPR) through the leaky vasculature characteristic of many solid tumors (Cabral et al.; Matsumura and Maeda, 1986).

Scrambled peptide showed rapid clearance, with only 0.2% of injected particles still in circulation after 40 min post-injection. Total number of injected beads was estimated 10^7 from flow cytometry analysis, which was correlated with their intensity of DiR using LICOR Imaging system. DiR signals from both blood and tissues, which were collected at 40 min post-injection, were nicely detected under LICOR (Fig. 3-3A). Tumors composed of tdTomato-expressing A549 cells emits detectable fluorescence at 700 nm under LICOR measurement, with intensity having linear correlation with both tumor mass and intensity at 800 nm (Fig. 3-3B). This made possible to estimate background level at 800 nm emission and the number of DiR-labeled beads accumulated in tumors and other organs (Fig. 3-3C). This represents the peptide sequence specificity for the capability of avoiding immune cell clearance, requiring the specific interaction between CD47 or its binding site sequence and SIRP α on immune cells.

3-2-2. In Vitro Cytotoxicity of TAX-loaded Nano-beads with Surface Modifications

The ultimate goal of this study is to see if CD47 or 'Self' peptide can avoid the clearance by immune cells during circulation and eventually improve the drug delivery capacity for the nano-sized particles. Paclitaxel (TAX) as a model drug was successfully loaded into polystyrene beads used in this study through hydrophobic interactions. Various surface modifications were applied to the particles with IgG and other molecules such as CD47, PEG, and antibody against hCD47. The attachment of CD47 does not affect cytotoxicity of the TAX-loaded particles (Fig. 3-1), showing similar IC₅₀ as beads with only IgG (IC₅₀ = 0.5 μ g/mL). Anti-hCD47 antibody was attached on the beads' surface via biotin to see if the antibody can recognize CD47 molecule

expressed on the surface of tumor-comprising A549 cells, thereby serving as a targeting moiety in vivo. Interestingly, beads with anti-CD47 showed slightly high cytotoxicity similar to widely used TAX formulation using Cremophor EL, essentially constituted with small molecule surfactant. Free TAX showed the lowest IC50 among the tested samples, while PEG-coated beads showed the highest value (or lowest cytotoxicity) possibly because of the steric repulsion by PEG blush on the surface.

3-2-3. Enhanced Tumor Shrinkage with TAX-loaded Beads with CD47 or ‘Self’ Peptide

Lastly, clearance-avoiding nanobeads loaded with anti-cancer drug TAX were injected into the tail vein of tumor bearing mice to see if those drug-loaded particles can deliver their cargo to the tumor tissue and release drug molecules to kill the cancer cells. TAX is very potent anti-cancer drug as shown in Fig. 3-2, and even opsonized beads could suppressed the growth of A549 subcutaneous tumor after 3 daily doses (Fig. 3-4A). CD47 beads showed successful shrinkage of the tumor, almost similar level to the conventional TAX formulation with Cremophor EL. TAX/Cremophor EL formulation is known to cause adverse effects on healthy cells, and we also observed necrosis in the tail. All mice injected with TAX-loaded CD47 beads showed no evidence of significant side effects, giving consistent shrinkage of the tumors with statistically significant difference from opsonized beads. ‘Self’ peptide-attached beads could also show similar capacity for tumor shrinkage, and with the help of targeting capability of anti-hCD47 they achieved quicker anti-tumor effect compared to TAX/Cremophor EL detected at 1 day post-injection. Although further study for optimizing dosing pattern is required, the presented result suggests the remarkable advantage of the combination of targeting moiety and CD47 to achieve quick tumor shrinkage.

3-3. Conclusions

Phagocytes are found in all tissues of the body in addition to the spleen and liver, and they have key roles in recognizing and clearing foreign cells and particles as well as contributing to inflammatory responses with cytokine release and oxidative burst. Recently study from Discher lab showed that implantation of polyurethane slabs coated with hCD47 will inhibit oxidation of the polymer [30], indicating a general capacity of this 'Marker of Self' to passivate *via* active signaling to Macrophages – a form of 'Active Stealth,' via interaction between CD47 and its receptor SIRP α on Macrophages.

Understanding of the CD47-SIRP α interactions is beginning to find application in disease, with blocking of CD47 on tumor cells allowing tumor-associated macrophages to attack the tumor (Willingham et al.). CD47 or even 'Self' peptide, which is designed from CD47 binding sites, on nanoparticles should likewise limit uptake by tumor-associated macrophages of nano-particle imaging agents and therapeutics and thus improve delivery to cancer cells. The presented study using CD47- or even 'Self' peptide-coated nanobeads loaded with anti-cancer drug TAX showed similar level of cytotoxicity *in vitro* to conventionally used TAX formulation with Cremophor EL but superior tumor shrinkage capacity *in vivo*, consistent with the improved accumulation of Active Stealth beads in tumor tissue, proved by non-invasive imaging study with near infrared dye. Presented results encourage the use of CD47 or even 'Self' peptide for avoiding the clearance by immune cells, which has been under-studied area probably due to strong belief in PEG stealthiness, for the achievement of advanced drug delivery system. The combination use of PEG for avoiding opsonization and CD47/'Self' peptide for avoiding clearance of delivery particle after eventual opsonization may contribute to the new step toward clinical use of drug delivery system for cancer therapies.

3-4. Materials and Methods

Beads sample preparation

Streptavidin-coated polystyrene beads of 160 nm radius (Spherotech) were washed and blocked 3x in PBS plus 0.4% BSA. First, beads were labeled with near infrared dye DiR at room temperature. After washing, recombinant, biotinylated human-CD47 or 'Self' peptide was attached to the beads and then rabbit anti-streptavidin conjugated with FITC was added as an Opsonizing IgG-antibody (Rockland Immunochemicals). Anti-hCD47 antibody was added afterwards, if necessary. Beads were incubated at room temperature for 30-45 min to let those molecules attach to the beads surface, then washed and re-suspended in PBS for injection.

Live and ex vivo imaging of DiR beads

Human lung carcinoma A549 cells (10^6) were suspended in PBS with 25% Matrigel (BD Bioscience) and injected subcutaneously into flank sites of each NSG mouse. After about 5 weeks, the tumor-bearing mice received tail vein injections of DiR dye-coated beads with surface modifications as above. Fluorescent intensity from DiR dye in tumor areas was monitored at 10min, 40min, 90min and 120min, using Xenogen IVIS Spectrum Imaging System (Caliper Life Science) and Living Image Software (Cliper Life Sciences) for later analysis. After 120 min post-injection, the mice were sacrificed for harvesting tumors and blood. Harvested tumors and blood were imaged with the LICOR Odyssey imaging system to measure the number of DiR-labeled beads.

Paclitaxel loading on beads

10⁸ polystyrene beads were suspended in 300 µL Milli-Q water. 5 µL of 4.5 mg/mL paclitaxel (LC Laboratories) in methanol was added to the beads to achieve 75 µg/mL concentration. After overnight incubation at room temperature and following spin-down, beads were re-suspended in 20 µL of PBS for concentration. 10 tubes prepared in the same way were combined to achieve 10⁹ particles suspension in 200 µL PBS for a single injection. If necessary, beads surface was modified by attaching molecules as shown above.

MTT Assay

5000 A549 cells were seeded on wells of 96-well plate, 24 hours prior to drug treatment. Cells were treated with series dilution of beads samples loaded with paclitaxel, starting from 7.5 µg/mL. After 24 hours incubation at 37°C with 5% CO₂, cells were washed once with PBS and added with 100 µL growth medium and 20 µL of 5 mg/mL Thiazolyl Blue Tetrazolium Bromide (Sigma). After 4 hours incubation at 37°C with 5% CO₂, purple crystal in the cells were solubilized by adding 100 µL DMSO. Absorbance was read at 560 nm.

Tumor treatment study

About a month after A549 cell inoculation, tumor-bearing mice were treated with 4 daily injections (i.v.) of paclitaxel-loaded beads with surface modifications at a dose of 7.5 mg/kg. Tumor size was measured on daily basis, making an estimation of volume with

$$\text{Tumor volume} = \frac{1}{2} * (\text{major axis}) * (\text{minor axis})^2$$

45

As a positive control for tumor shrinkage, paclitaxel solubilized with Cremophor EL (Sigma) was injected at 22 mg/kg.

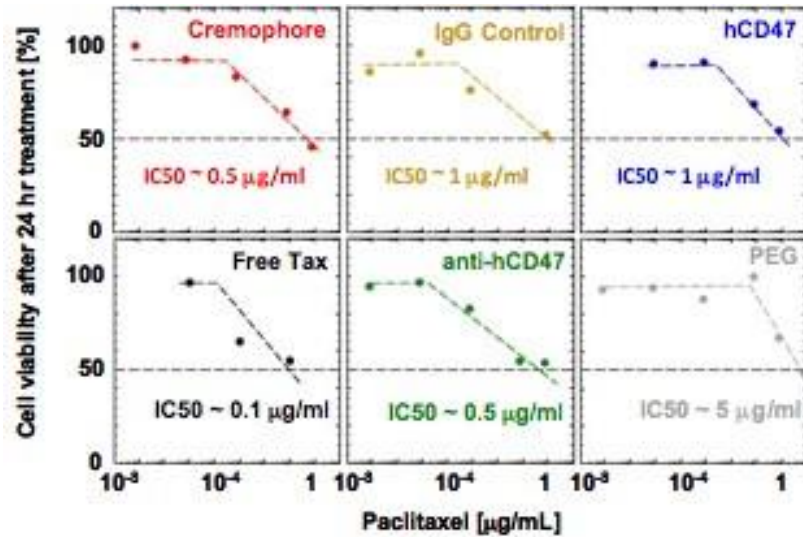
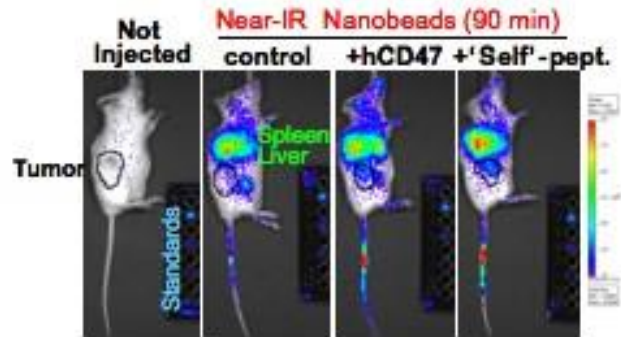


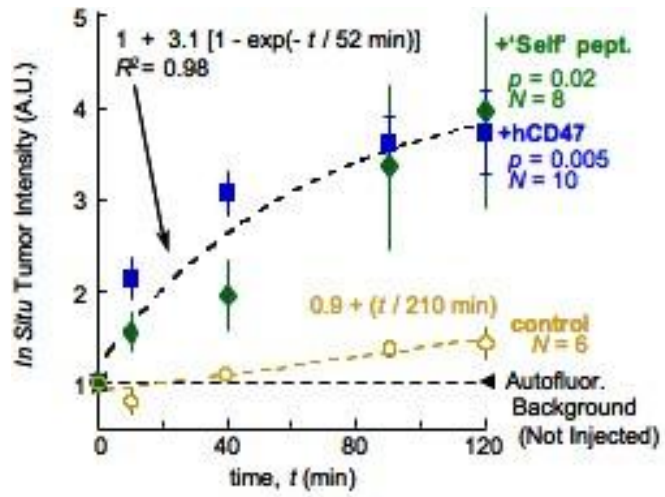
Figure 3-1. Cytotoxicity of TAX-loaded nanobeads with different surface modifications

A549 cells were incubated with TAX-loaded polystyrene beads for 24 hours to test their cytotoxicity, as well as control TAX formulation with Cremophor EL or free TAX. Beads were attached with IgG and additional molecule as specified in the upper right of the panels ('IgG' represents no additional molecule). IC50 of each sample was roughly determined by the trend line as shown in each panel.

A



B



C

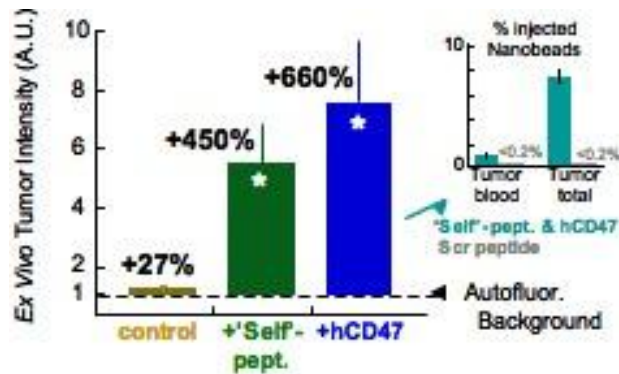
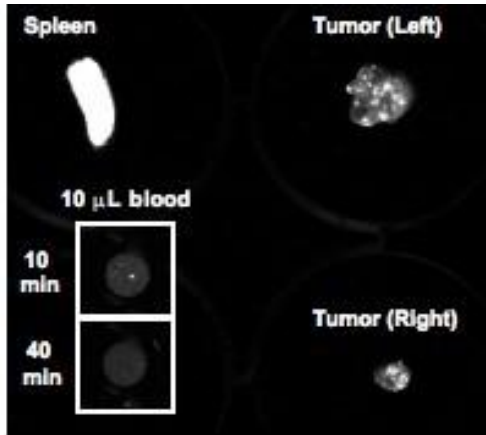


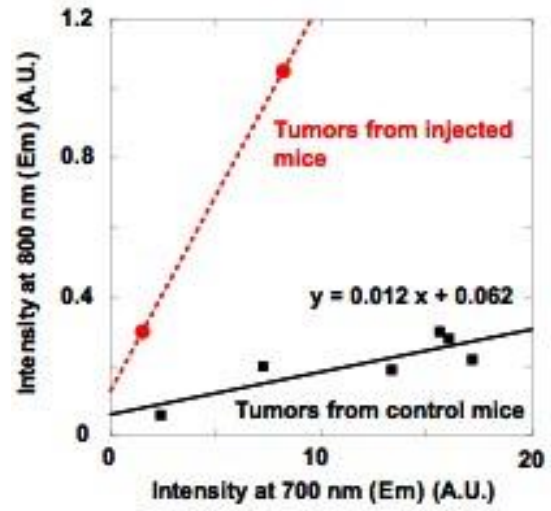
Figure 3-2. ‘Self’-peptide and human-CD47 enhance tumor imaging by Near-Infrared particles

(A) NSG mice with flank tumors of A549 lung-derived cells (black circles) received tail vein injections of nanobead mixtures in which one bead type is labeled with DiR fluorophore. Images of live mice and calibration standards were taken with a Xenogen imager. Tumor-bearing mice have persistence ratios of particles in blood at 35 min, even though many particles are seen in spleen and liver. (B) The tumor region was estimated in the brightfield image for quantitation of total fluorescence at each time point, and all results for ‘Self’-peptide and CD47 were combined in the fit. Results are cumulated from all tumors from three different sets of tumor-bearing mice. N , Number of tumors. (C) Tumors were harvested from one set of tumor-bearing mice for *ex vivo* quantitation by an Odyssey imaging system. For control, $N = 2$; for ‘Self’-peptide, $N = 4$; and for CD47, $N = 6$ tumors. Inset bargraph shows the high percentage of nanobeads in the tumor compared to an upper bound for the nanobeads in the blood vessels within the tumors ($n = 2$).

A



B



C

	Intensity
Left Tumor	0.89
Right Tumor	0.22
Spleen	309.69
1mL Blood (Calc.)	6.08

$$\frac{1\text{mL blood}}{\text{Spleen}} = \frac{6.08}{309.69} = 2\%$$

240.41 == 10^6 beads

Spleen: 1.29×10^6 beads (~13% of injected/assuming 10^7 beads injected)

In blood ~0.26% of injected beads circulating after 40 min = 26,000 beads in blood

Tumor signal is 0.1 to 0.3% of Spleen ~ 2000 beads

Figure 3-3. Estimation of the beads number in tumor/spleen/blood 40 min after injection

(A) Representative image of tumor, spleen and blood (in 96-well plate) from the mice injected with opsonized beads with Scrambled peptide, taken by LICOR imaging system. 10 μ L of blood sample was diluted with 90 μ L of PBS to avoid too strong local intensity and saturation. Blood was collected at 10 and 40 min post-injection to compare the number of beads remaining in the circulation. (B) Tumor of tdTomato-expressing cells were measured for fluorescence emission at both 700 and 800 nm. 700 nm represents the signal from tdTomato, nicely correlating with tumor mass (not shown) and therefore background at 800 nm. The background subtraction was performed based on the estimation from the equation shown in the graph. (C) Emission intensity at 800 nm was used for the estimation of the number of beads. The calculation indicates remarkable clearance by spleen macrophages of beads with Scrambled peptide, leading to the idea that specific interaction between CD47 (or 'Self' peptide) and SIRP α is needed for strong accumulation in tumors.

A

B

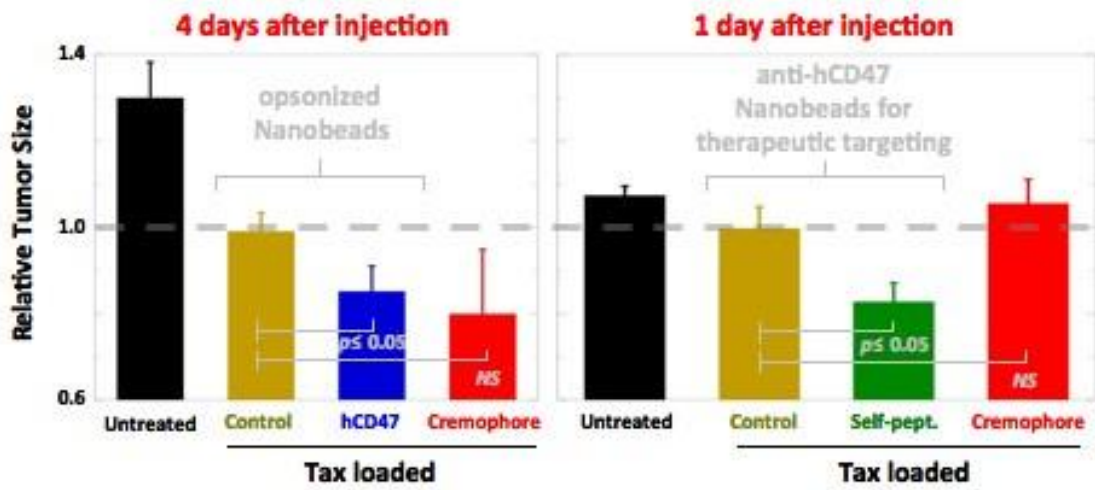


Figure 3-4. Tumor shrinkage with TAX-loaded nanobeads with CD47 or ‘Self’ peptide

NSG mice were injected with TAX-loaded nanobeads as well as positive control formulation of TAX/Cremophor EL, (A) with 3 daily doses and tumor size monitoring every day until day 4 or (B) single injection and observation on following day in case of beads also attached with anti-hCD47. Tumor size (volume) was estimated as shown in Method section and relative value was calculated with the tumor size from mice injected with control IgG beads.

PEGylated particle	IgG opsonized?	Reference
Poloxamer-stabilized liposome	yes	T. M. Goppert and R. H. Muller. Int. J. Pharm., 2005, 302, 172–186
	yes	S. Tamilvanan, ... S. Benita Eur. J. Pharm. Biopharm., 2005, 59, 1–7
PEG-PHDCA	yes	M. T. Peracchia, ... P. Couvreur Biomaterials, 1999, 20, 1269–1275
	yes	H. R. Kim, ... P. Couvreur Biomacromolecules, 2007, 8, 793–799
	yes	H. R. Kim, ... M. Taverna Electrophoresis, 2007, 28, 2252–2261
PEG-PLA-PEG	yes	M. Luck, ... T. Kissel J. Controlled Release, 1998, 55, 107–120
PEG-coated latex	yes	M. Luck, ... R. H. Muller J. Biomed. Mater. Res., 1998, 39, 478–485
PEG-nevirapine	yes	R. Shegokar, ... R. H. Muller Nanomed. Nanotechnol., Biol. Med., 2011, 7, 333–340
PEG-PCL	yes	C. Lemarchand, ... P. Couvreur Biomaterials, 2006, 27, 108–118
Poloxamer-coated polystyrene	yes	T. Blunk, ... R. H. Muller Electrophoresis, 1993, 14, 1382–1387

Table. 3-1 List of papers studying with PEG-coated particles and showing opsonization (binding) with IgG

3-5. References

Armstrong, J. K., Hempel, G., Koling, S., Chan, L. S., Fisher, T., Meiselman, H. J. and Garratty, G. (2007). Antibody against poly(ethylene glycol) adversely affects PEG-asparaginase therapy in acute lymphoblastic leukemia patients. *Cancer* **110**, 103-11.

Bartlett, D. W., Su, H., Hildebrandt, I. J., Weber, W. A. and Davis, M. E. (2007). Impact of tumor-specific targeting on the biodistribution and efficacy of siRNA nanoparticles measured by multimodality in vivo imaging. *Proc Natl Acad Sci U S A* **104**, 15549-54.

Bentley, A. A. and Adams, J. C. The evolution of thrombospondins and their ligand-binding activities. *Mol Biol Evol* **27**, 2187-97.

Brown, E. J. and Frazier, W. A. (2001). Integrin-associated protein (CD47) and its ligands. *Trends Cell Biol* **11**, 130-5.

Bruce, L. J., Beckmann, R., Ribeiro, M. L., Peters, L. L., Chasis, J. A., Delaunay, J., Mohandas, N., Anstee, D. J. and Tanner, M. J. (2003). A band 3-based macrocomplex of integral and peripheral proteins in the RBC membrane. *Blood* **101**, 4180-8.

Cabral, H., Matsumoto, Y., Mizuno, K., Chen, Q., Murakami, M., Kimura, M., Terada, Y., Kano, M. R., Miyazono, K., Uesaka, M. et al. Accumulation of sub-100 nm polymeric micelles in poorly permeable tumours depends on size. *Nat Nanotechnol* **6**, 815-23.

Friedl, P., Maaser, K., Klein, C. E., Niggemann, B., Krohne, G. and Zanker, K. S. (1997). Migration of highly aggressive MV3 melanoma cells in 3-dimensional collagen lattices results in local matrix reorganization and shedding of alpha 2 and beta 1 integrins and CD44. *Cancer Research* **57**, 2061-2070.

Klibanov, A. L., Maruyama, K., Beckerleg, A. M., Torchilin, V. P. and Huang, L. (1991). Activity of amphipathic poly(ethylene glycol) 5000 to prolong the circulation time of liposomes depends on the liposome size and is unfavorable for immunoliposome binding to target. *Biochim Biophys Acta* **1062**, 142-8.

Matsumura, Y. and Maeda, H. (1986). A new concept for macromolecular therapeutics in cancer chemotherapy: mechanism of tumorotropic accumulation of proteins and the antitumor agent smancs. *Cancer Res* **46**, 6387-92.

Mouro-Chanteloup, I., Delaunay, J., Gane, P., Nicolas, V., Johansen, M., Brown, E. J., Peters, L. L., Van Kim, C. L., Cartron, J. P. and Colin, Y. (2003). Evidence that the red cell skeleton protein 4.2 interacts with the Rh membrane complex member CD47. *Blood* **101**, 338-44.

Oldenburg, P. A., Zheleznyak, A., Fang, Y. F., Lagenaur, C. F., Gresham, H. D. and Lindberg, F. P. (2000). Role of CD47 as a marker of self on red blood cells. *Science* **288**, 2051-4.

Photos, P. J., Bacakova, L., Discher, B., Bates, F. S. and Discher, D. E. (2003). Polymer vesicles in vivo: correlations with PEG molecular weight. *J Control Release* **90**, 323-34.

Rossin, R., Muro, S., Welch, M. J., Muzykantov, V. R. and Schuster, D. P. (2008). In vivo imaging of ⁶⁴Cu-labeled polymer nanoparticles targeted to the lung endothelium. *J Nucl Med* **49**, 103-11.

Strowig, T., Rongvaux, A., Rathinam, C., Takizawa, H., Borsotti, C., Philbrick, W., Eynon, E. E., Manz, M. G. and Flavell, R. A. Transgenic expression of human signal regulatory

protein alpha in Rag2^{-/-}-gamma(c)^{-/-} mice improves engraftment of human hematopoietic cells in humanized mice. *Proc Natl Acad Sci U S A* **108**, 13218-23.

Subramanian, S., Boder, E. T. and Discher, D. E. (2007). Phylogenetic divergence of CD47 interactions with human signal regulatory protein alpha reveals locus of species specificity. Implications for the binding site. *J Biol Chem* **282**, 1805-18.

Subramanian, S., Parthasarathy, R., Sen, S., Boder, E. T. and Discher, D. E. (2006). Species- and cell type-specific interactions between CD47 and human SIRPalpha. *Blood* **107**, 2548-56.

Takenaka, K., Prasolava, T. K., Wang, J. C., Mortin-Toth, S. M., Khalouei, S., Gan, O. I., Dick, J. E. and Danska, J. S. (2007). Polymorphism in Sirpa modulates engraftment of human hematopoietic stem cells. *Nat Immunol* **8**, 1313-23.

Tsai, R. K. and Discher, D. E. (2008). Inhibition of "self" engulfment through deactivation of myosin-II at the phagocytic synapse between human cells. *J Cell Biol* **180**, 989-1003.

Turk, M. J., Waters, D. J. and Low, P. S. (2004). Folate-conjugated liposomes preferentially target macrophages associated with ovarian carcinoma. *Cancer Lett* **213**, 165-72.

Willingham, S. B., Volkmer, J. P., Gentles, A. J., Sahoo, D., Dalerba, P., Mitra, S. S., Wang, J., Contreras-Trujillo, H., Martin, R., Cohen, J. D. et al. The CD47-signal regulatory protein alpha (SIRPa) interaction is a therapeutic target for human solid tumors. *Proc Natl Acad Sci U S A* **109**, 6662-7.

Chapter 4: Lamin-A levels limit 3D-migration but protect against migration-induced apoptosis

Cell migration through dense tissue and matrix requires a cell and its nucleus to contort and flow. A strong dependence of 3D migration on the variably expressed nucleoskeletal protein Lamin-A is revealed here across widely different normal and cancerous cell types relevant to regeneration and disease. Crawling through tissue is modeled by motility through micro-pores, with small decreases in Lamin-A producing large increases in net migration. Surprisingly, the largest effects occur when Lamin-A is low relative to constitutive Lamin-B's. Nuclear shape changes after micro-pore migration as well as nuclear response times in micropipette aspiration scale strongly with the ratio of Lamin-A:Lamin-B across cell types, revealing Lamin-A's role in nuclear plasticity and Lamin-B's role in nuclear elasticity. Lamin-A also protects against apoptosis induced by micro-pore migration, with deeply deficient cells showing defects in stress-resistance. Xenografts provide *in vivo* insight and show moderately low Lamin-A levels promote growth of the graft. The nuclear lamina thus acts as a physical impediment to motility and also promotes survival in withstanding the mechanical stresses of migration.

4-1. Introduction

Cell motility in adult animals underlies a wide range of critical processes, including trafficking in tissue repair and disease. In the "invasion-metastasis cascade" (Weinberg, 2007), for example, cells in the tumor periphery crawl through surrounding tissue and extracellular matrix (ECM) to

divide or perhaps metastasize by squeezing into narrow vessels. Multipotent stem cells in the bone marrow likewise transmigrate into blood and other tissues far from their usual niche and have potential roles in tissue regeneration (Pittenger and Martin, 2004) as well as cancer (Houghton et al., 2004; Nakamizo et al., 2005). Successful migration requires cells to survive large distortions as they make their way through ECM or across a basement membrane (**Fig. 4-1A**), and the largest single organelle in every cell is typically the nucleus, which tends to be solid-like and stiff (Dahl et al., 2005; Lammerding et al., 2006; Pajeroski et al., 2007). In light of the high stresses generated by the cytoskeleton in crawling through matrix (Mierke et al.), we hypothesized key roles for nuclear mechanics in 3D-migration and cell survival.

Lamins are intermediate filaments (IFs) in the nuclei of most adult animal cells and have multiple roles as they modulate gene expression and also provide physical support akin to other IF proteins (eg. keratins in nails) (Dechat et al., 2008). A meshwork of Lamins assembles in nearly all cells with expression from three genes: *LMNA* which is alternatively spliced to Lamins -A and -C, and *LMNB1* and *LMNB2*. An instructive exception is the highly motile polymorphonuclear leukocyte (PMN) that lacks A-type Lamins (Olins et al., 2001). PMNs migrate through micron-sized pores of the endothelium and through dense tissues, as modeled *in vitro* with chemotactic gradients that induce PMN transmigration through cell monolayers (Nash et al., 1987), and the flexibility of the multi-segmented nucleus is thought to facilitate such motility (Olins et al., 2001). Terminal differentiation to PMNs involves downregulation of Lamins, but PMN-neutrophils also survive for only days (Pillay et al., 2010). Lamin-A is generally the most variable Lamin isoform in comparisons of normal tissues (eg. Jung et al., 2012), and so altered Lamin-A levels in tumors (Kaufmann et al., 1991; Willis et al., 2008) are perhaps understandable and perhaps tempting to view from a PMN perspective. Higher rates of colon cancer recurrence indeed associate with low Lamin-A (Belt et al., 2011). However,

malignancy of squamous cell and basal cell carcinomas as well as colorectal cancer are all associated with *elevated* Lamin-A (Foster et al., 2010; Tilli et al., 2003). In light of such seemingly contradictory correlations, we sought to clarify mechanistic roles for Lamin-A in 3D migration across a broad range of cell types that exhibit mesenchymal-type motility.

Mouse knockouts for all of the Lamins are surprisingly viable in early development, but all animals succumb prematurely. Lamin-A knockout mice develop all tissues, but death at age 5-6 weeks with evidence of dystrophic heart and muscle (Sullivan et al., 1999) indicates more severe defects than the prototypical *mdx* dystrophic mice that survive for almost 100 wks (Chamberlain et al., 2007). Lamin-B1, B2 knockouts have been studied recently and once again show all embryonic lineages develop, but mice die at birth with poorly innervated diaphragm, small body size, and a brain that fails to develop past embryonic day 18.5 (Coffinier et al., 2011; Kim et al., 2011). Apoptosis of neuroprogenitors was particularly apparent in migration from the inner cortex through the dense mid-cortex, which is notable because in wildtype migration of neuroblasts through the developing cortex, the nucleus can be stretched by almost 5-fold for many minutes at a time (Pajeroski et al., 2007; Tsai et al., 2005). Likewise with invasive migration of glioblastoma, the nucleus appears distorted by at least 2-fold as these cells exert contractile forces to push or pull nuclei through tissue (Beadle et al., 2008). Lamin isoform ratios ultimately prove here to be predictive of the Lamin- A sensitivity of 3D-migration through tissue-like, small diameter pores both *in vitro* and *in vivo*.

4-2. Results

4-2-1. 3D migration is sensitive to Lamin-A levels and can be biphasic

The three human cell types in focus here are highly diverse in their mesenchymal-type motility (**Fig. 4-1B, left**). Glioblastoma-derived U251 cells migrate 35-fold faster through 3 μm pore transwell filters than lung carcinoma derived A549 cells while bone marrow-derived, primary mesenchymal stem cells (MSCs) are almost 8-fold faster than A549s. Rigid, micro-porous filters (3-8 μm pores) seem appropriate based on measurements of the elasticity of flank xenografts, which are indeed stiff (**Fig. S4-1**) relative to a typical nucleus (Pajeroski et al., 2007), and also based on the apparent micro-porosity of decellularized xenografts as well as known capillary diameters (Fig. 4-1A inset). In 2D-migration, speeds of these same cell types vary by just 2-fold but do follow the same trend as in 3D-migration: U251 > MSC > A549 (**Fig. S4-2**). While 2D speeds are 10-20 $\mu\text{m}/\text{hr}$, very few cells cross the 22 μm -thick filters on the same time scale, consistent with impeded migration through 3 μm pores.

The three cell types also have highly distinct Lamin profiles (**Fig. 4-1B, right**). We used mass spectrometry (Maloney et al.) to measure for A549s as mean Lamin-A:B ratio of 2.3 (Fig. 4-1B), which is a measurement that cannot be done by antibody methods and indicates of course that Lamin-A is the dominant isoform in A549s. MSCs have 3.5-fold higher A:B while the U251 cells have 3.1-fold less (**Fig. S4-3**), so that Lamin-A:B varies by more than 10-fold across cell types: MSC > A549 > U251. Additional studies show that this ratio scales with the stiffness of the tissue of origin, with brain being softer than lung, and lung softer than bone (Swift, submitted). Quantitative immunofluorescence measurements for B-type Lamins as well as quantitative Western blots further show that A549 have the lowest Lamin-B while MSCs express the most, although variations in Lamin-A are larger. From the A:B ratio and the normalized amounts of Lamin-B, total Lamins (A + B) are also readily calculated (Fig. S4-3). The various measurements thus establish that wildtype migration and Lamin abundance are significantly

different between the three cell types. Nonetheless, the Lamin profiles are shown below to predict a surprising trend in the *sensitivity* of 3D migration to Lamin changes.

Knockdown of Lamin-A by transient transfection of short interfering RNA (siLMNA) was again followed by migration studies. While 2D-migration was unaffected by partial knockdown (Fig. S4-2), A549 cells showed a net migration efficiency through 3 μ m pores that is biphasic in its dependence on Lamin-A expression. Relative to scrambled siRNA-treated cells in the same experiment, a partial knockdown of ~50% (siLMNA+) produced the greatest increase in 3D-migration of more than 4-fold (**Fig. 4-1C**), a trend confirmed with a second siLMNA (**Fig. S4-4A**). Overexpression of Lamin-A strongly impeded migration of A549 cells, and followed the same trend in migration established with partial knockdown: just ~10% more Lamin-A suppressed migration by 90%. Knockdown of these over-expressing cells increased as expected the net migration (**Fig. S4-4B**), but further overexpression reached the same minimum level of net migration (see sorting discussion below). Combined with partial knockdown, the range of net migration seen throughout these studies of A549 cells varies systematically by about 50-fold.

To assess specificity of Lamin-A knockdown, label-free MS was used to quantify the levels of the most abundant structural proteins after partial knockdown (**Fig. 4-1D**, **Table S4-1**): 148 of 169 proteins (88%) differed from control by less than 25%. The transient, siRNA knockdown of cells was preferred over methods such as transduction with short hairpin RNA (shRNA), because sustained disruption of Lamins can impact a broad range of cell processes (Hutchison and Worman, 2004). Lamin-A knockdown here also did not perturb proliferation of A549 cells (**Fig. S4-4C**), which is consistent with past findings (Elbashir et al., 2001). In sum, the partial, transient knockdown revealed only one obvious phenotype, namely enhanced migration through small micro-pores.

Knockdown of Lamin-A by ~50% in both U251 cells and MSCs also showed significant increases in net migration (Fig. 4-1C). While the fold-increase relative to wildtype cells is smallest for U251s and intermediate for MSCs, to understand the sensitivity to Lamin changes it is necessary to account for the motility of wildtype cells as well as the real change in total Lamin levels (Fig.4-1C, inset plot; Fig. S4-3). The slope for each cell type in such a plot reveals the net *migration sensitivity to a Lamin-A change* ($m_{3D-sens}$) after partial knockdown and overexpression, and this cell-type specific $m_{3D-sens}$ is seen to vary by almost 20-fold. For a small amount of change to Lamin-A levels in U251, for example, the net number of U251 cells that migrate through the constraining pores is much higher than for the other cell types. U251 cells thus show the greatest sensitivity and MSCs show the least sensitivity ($m_{3D-sens}$: U251 > A549 > MSC). This is the same trend as the Lamin-A:B ratio in wildtype cells (Fig. 4-1B), which will be explained mechanistically in the next section.

One additional and striking feature in Fig.1C is the *biphasic* dependence of 3D migration on Lamin-A levels. Very deep knockdown (siLMNA++ treatment) *decreases* the net migration of cells through the fibronectin-coated filters by 50% relative to wildtype, without affecting 2D migration (Fig. S4-2). The biphasic effect is also apparent without fibronectin pre-coating of the filter and was confirmed with a second siLMNA (Fig. S4-4A). As elaborated in detail below, 3D-migration through small pores but not large pores leads to a net loss in total cell number and in proportion to knockdown (**Fig. S4-4D**).

Shape changes of high Lamin-A nuclei are sustained after migration through 3 μ m pores

In counting cells on the bottom of the 3 μ m filters, we noticed that nuclear shapes on the bottom surfaces of the 3 μ m transwell filters were strikingly elongated and distinct compared to the

typical elliptical shapes on the top surface (**Fig. 4-2A**). With 8 μm transwell filters, nuclei on the top and bottom of the filters appeared in shape indistinguishable from healthy 2D cultures and cells migrating in 2D (Fig. 4-2A, right; **Fig. S4-5A**), and Lamin-A knockdown had no effect on net cell migration (Fig. 4-2A, lower right inset graph). For both 3 and 8 μm transwell filters, images showed nuclei partially or fully inside pores, but only for the 3 μm pores did we observe Lamin-A segregation from Lamin-B as the former but not the latter outlines the pore exit (Fig. 4-2A, lower left inset image). Since the 3 μm pores are only about 3% of the average projected nuclear area of A549 cells ($220 \pm 50 \mu\text{m}^2$ for A549 nuclei on Top) compared to 23% of 8 μm pores, nuclear shape changes appear far greater in entering the smaller pores. Sustained deformation of nearly all nuclei is apparent with 3 μm pores, regardless of whether Lamin-A was knocked down or not. However, for 8 μm pores, Lamin-A knockdown had no effect on nuclear shapes on the bottom of the filters, and knockdown also had no effect on the net migration of cells (Fig. 4-2A, lower inset). These findings together with those in 2D provided strong evidence that the moderate perturbations of Lamin-A do *not* greatly perturb the cytoskeleton, which is consistent with the proteomic analyses (Fig. 4-1D). More importantly, for the three tested cell types, sustained changes in nuclear shape correlate with 3D migration sensitivity to Lamin-A.

Importantly, U251 nuclei did not change shape after migration through 3 μm pores, whereas MSCs showed the most extreme elongation of nuclei (**Fig. 4-2B** inset images; **Fig. S4-5B, C**). Changes in circularity of nuclei after migration through 3 μm pores were therefore quantified for the three different cell types, with more distorted nuclei on bottom producing a negative value for the characteristic ‘ $\Delta\text{Circularity of Nucleus}$ ’ (Δ_{Circ}). Fig. 4-2B reveals a remarkably strong, exponential correlation between this structural characteristic and the functional measure $m_{3\text{D-sens}}$ for 3D-migration sensitivity to Lamin-A in Fig. 4-1C. The different Lamin-A:B ratios for the various cell types seemed a more explicit structural basis for both $m_{3\text{D}}$.

Δ_{Circ} and Δ_{Circ} , and **Fig. 4-2C** confirms the excellent correlation. In particular, wildtype MSCs have the highest Lamin-A:B and show the greatest nuclear deformation, with strong attenuation after Lamin-A knockdown (Fig. 4-2C, inset).

These results suggest that A- and B-type Lamin isoforms play separate roles in nuclear shape and viscoelasticity. When Lamin-B is the dominant isoform as in the U251 cells, the nucleus readily recovers after deformation through a small pore, behaving reversibly like an elastic spring (Fig. 4-2C, upper inset schematic). When Lamin-A is the dominant isoform as in the A549 cells and MSCs, the nucleus deforms in a plastic manner after migration through a small pore, behaving irreversibly like a viscous fluid in the Lamina. This mobility of Lamin-A can also help explain its lagging segregation in A549 nuclei (Fig. 4-2A, lower inset). Past photobleaching studies of GFP fusions of the Lamins had shown Lamin-B1 to be immobile whereas both Lamin-A and Lamin-C appeared mobile (Shimi et al., 2008), which seems consistent with the long-time, elastic *versus* fluid contributions of the Lamins to nuclear shape changes described here. We had previously quantified the irreversible plasticity of nuclei after aspiration of a nucleus into a micropipette (Dahl et al., 2005; Pajerowski et al., 2007), and our mass spectrometry method now allows us to calibrate the Lamin-A:B ratios and determine which isoform dominates in any given cell type. Thus the plasticity shown here not only results from *active* cell migration and correlates exponentially with the sensitivity of 3D migration to Lamin-A, but the trends can all be understood – and will be shown predictable below – from Lamin-A:B ratios.

Cell sub-populations sort in 3D migration, with more flexible nuclei promoting migration

Lamin-A:B levels are naturally variable within cell populations, with a standard deviation/mean of ~ 0.25 for the A549 cell line ($n > 150$). We therefore examined more carefully the Lamin intensities and nuclear shapes on both sides of the 3 μm filters and discovered that A549 cells on the bottom generally had lower Lamin-A:B levels as well as more distorted nuclei (**Fig. 4-3A**). Importantly, similar changes were not observed with the 8 μm pores (Fig. 4-2A, S4-5A). Cell sub-populations with lower Lamin-A thus migrate more quickly through constraining pores.

Previous studies of individual nuclei with micropipette aspiration after Lamin-A knockdown showed Lamin-A to be important to nuclear elasticity and stability for short times and high stresses (Pajerowski et al., 2007). Here we tested the Lamin-A dependence of nuclear deformation using aspiration pressures (**Fig. 4-3B**) that deform the wildtype nucleus at rates close to cell migration speeds reported for physically constraining tissue models such as fibrosarcoma cells in a 3D collagen lattice ($\sim 0.75 \mu\text{m}/\text{min}$; Wolf et al., 2003). The \sim kiloPascal pressures used are also similar in magnitude to traction stresses that migrating cells apply to stiff substrates (Dembo and Wang, 1999). The resulting linear increase in nuclear membrane extension (after 5 min for several pressures) is 3.6-fold steeper after partial knockdown of Lamin-A compared to control cells (Fig. 4-3B, bottom). This is similar to the ~ 4 -fold difference seen above in active migration through pores (Fig. 4-1C) of diameter similar to the micropipette and seems consistent with the migration-based sorting through the 3 μm filter of the low Lamin-A sub-population of cells.

For an even broader examination of the Lamin-A dependence of nuclear mechanics, micropipette aspiration was applied to all three cell types together with knockdowns and overexpressing cells (**Fig. S4-6A-C**). Once an aspiration pressure is applied, the nucleus is extended to some length over time, and one can either (*i*) determine the response time, τ , needed

to achieve the same extension length for all nuclei, or else (ii) pick a common time and determine the different aspirated lengths as done above. For the physical plasticity model of Fig. 2C, it is readily shown that

$$\tau = (\text{viscosity} / \text{elasticity}) \quad \text{Eq.1}$$

and based on the idea of separate viscoelasticity contributions from Lamin isoforms, we plot τ versus Lamin A:B ratios. For the 10-fold range in Lamin-A:B ratio between cell types, including cells where A-type Lamins dominate B-type Lamins, τ varies by more than 100-fold, with a similarly strong effect for A549 cells overexpressing Lamin-A (**Fig. 4-3C**). A steeply positive power law fit

$$\tau \sim [\text{Lamin-A} : \text{Lamin-B}]^{2.5} \quad (R^2 \geq 0.85) \quad \text{Eq.2}$$

reveals the primary contribution of Lamin-A to nuclear viscosity, whereas Lamin-B's contribute predominantly to nuclear elasticity. The range of apparent viscosity measurements with knockdown cells in Fig. 3C is almost 10^4 -fold, which is similar to the fold-difference in the viscosities of honey and water.

For the plasticity model of Fig. 4-2C, an effective stiffness $E(t)$ is obtained by re-scaling the imposed aspiration pressure (or stress) by the aspirated length, which depends on time. $E(t)$ should increase even if the viscosity increases with higher Lamin-A, but the power law scaling should be weak if Lamin-A is predominantly contributing as a fluid and indeed: $E(t) \sim [\text{Lamin-A}:\text{B}]^{0.5}$ (**Fig. S4-6D**). Thus, a moderate decrease in Lamin-A leads to an overall increase in the flexibility of nuclei and more rapid 3D migration even in the absence of perturbations either to migration speed in 2D culture (Fig.S4-2) or to other abundant cellular proteins (Fig. 4-1D).

Lamin-A protects against 3D-migration induced apoptosis

In addition to observing sustained, plastic deformation of nuclei after migration through small pores, we noticed that the total number of cells on the 3 μm filters after 24 hours decreased with increasing level of Lamin-A knockdown (Fig. S4-4D). No such changes were observed with 8 μm filters. These observations and the decreased migration after deep knockdown of Lamin-A (Fig. 4-1C) prompted the hypothesis that mechanical stresses of migration could induce apoptosis. A protective role for Lamin-A is reasonable since enhanced apoptosis and necrosis is reported *in vivo* with Laminopathies and in *in vitro* studies (reviewed in: Dahl et al., 2008). Cells on both sides of the filters were therefore immunostained for cleaved caspase-3, an apoptosis marker downstream of multiple stress pathways, including mechanical stress (Cheng et al., 2009; Shive et al., 2002), and activatable within a few hours of insult (eg. staurosporine Zhang et al., 2004). This is a minimum time scale for cells to migrate the 22 μm thickness of the pores (Fig. S4-2). Imaging indeed showed apoptotic cells with their nuclei still in the pore (Fig. 4-4A images), which illustrates the coincidence of apoptosis and 3D-motility. With scrambled siRNA-treated cells, only ~1% or fewer cells on top of the filter were apoptotic compared to ~12% of cells that had migrated to the bottom of the filter (Fig. 4-4A, plot). Fibronectin had no statistically significant effect on apoptosis throughout these studies, which suggests that loss of anchorage from the bottom surface is limiting. The results thus reveal a significant wildtype level of 3D-migration enhanced apoptosis.

Partial knockdown of Lamin-A led to a significant increase in apoptosis on the bottom of the filter (Fig. 4-4A, plot), consistent with the > 10% decrease in total cell number after migration (Fig. S4-4D). Since partial reduction of Lamin-A in A549 cells showed negligible perturbation to the proteome (Fig. 4-1D), the results support the hypothesis that the nuclear Lamina protects physically against stress. In this case ‘stress’ is the mechanical stress generated by each cell

during its migration. Of course, despite these stresses and an increase in %-apoptotic cells, partial knockdown also produced a 4-fold increase in the net number of migrated cells, which indicates that the flexibility gains are considerably greater than the compromised stress response.

Deep knockdown of Lamin-A to <10% of wildtype A549 cells showed an average of 30% apoptotic cells that had migrated through the pores (Fig. 4-4A, plot). Decreased Lamin-A had no significant effect on apoptosis of cells in culture or on the top of the 3 μ m filters, but apoptosis in 3D-migration is consistent with the large decrease in total cell number after migration (Fig. S4-4D). More frequent apoptosis of cells with deep knockdown of Lamin-A helps to explain the suppressed migration of these cells (Fig. 4-1C star in main plot).

Deep knockdown cells also showed major changes to the proteome (**Fig. 4-4B**), which is not surprising given the many interactions of Lamin-A (Broers et al., 2006). Among the abundant, stress-related proteins that showed large decreases with deep knockdown of Lamin-A was HSP90, which is a molecular chaperone that accounts for about 2% of protein mass in most normal cell types. Western blots validated the decrease of HSP90 (**Fig. 4-4C**). HSP90 interacts with >200 proteins as well as being involved in responses against DNA damage (Trepel et al., 2010), which can be caused by applying mechanical stress to cells in culture (Mayr et al., 2002). Although other proteins of potential relevance changed (see Supplemental Discussion), we hypothesized that HSP90 provides critical protection against apoptosis induced by 3D-migration stresses that lead to protein unfolding and/or DNA damage. Cells were pre-treated for one day with the HSP90 inhibitor 17-AAG (Maloney et al., 2007) and allowed to migrate through 3 μ m pores in the presence of the drug. The drug caused 4-fold more apoptosis in sparse cultures of wildtype cells (**Fig. 4-4D**). This is significant but much less than half the apoptosis caused by migration through a pore, which suggests additional apoptotic mechanisms in migration. After deep knockdown of Lamin-A, additional treatment with 17-AAG increased apoptosis to a level

similar to that caused by migration through a pore and suggests HSP90 deficits are a major aspect of apoptotic mechanisms in migration. Importantly, drug treated cells, including both wildtype and knockdown cells, appeared to enter pores on the top filter but were not detectable on the bottom side of the transwell filter, whereas control cells gave results included in Fig. 4-4A. HSP90 is thus downstream of Lamin-A, with inhibited function being a major impediment to migration as well as cell death.

Lamin-A is low in the periphery of xenografts, and Lamin-A moderation enhances growth

For insights into Lamin levels in *in vivo* microenvironments, A549 cells were injected into the flanks of immuno-deficient NSG mice, and after 4 weeks xenografts were harvested and quickly sectioned into core and periphery sections. Collagenase treatment was followed by immunostaining of suspended A549 cells for human-specific Lamin-A and Lamin-B. Flow cytometry measurement of Lamin levels consistently showed that cells in the cores of tumors (n = 6 tumors) had higher Lamin-A:B than those from the peripheries of tumors (**Fig. 4-5A**). These results suggest that cells with more deformable nuclei (due to lower Lamin-A:B) more efficiently invade into the surrounding tissue, whereas cells with stiffer nuclei remain in the core. Cleaved caspase-3 in these freshly-derived cells was also measured, but only slightly more cells appeared apoptotic compared to the small fraction on the upper side of the transwell filters (Fig. 4-4A). There are of course mechanisms *in vivo* (eg. macrophages) to rapidly remove apoptotic cells that do not exist in reductionist culture studies above.

Because partial knockdown of Lamin-A produced a net increase in 3D-migration without significant changes to the proteome and without offsetting increases in cell death, we next sought

to assess the possible impact of partial knockdown on *in vivo* tumor growth. The lung tumor-derived A549 cells were first transduced with lentivirus to express the deep red fluorescent protein tdTomato which allows non-invasive monitoring of tumors at wavelengths where tissue autofluorescence is low (Winnard et al., 2006). A549^{tdTomato} cells with transient knockdown to one-third of wildtype Lamin-A levels were then injected into the flanks of immuno-deficient NSG mice, and similar numbers of control cells were injected into the contralateral sites (**Fig. 4-5B**) with 10-fold range in day-0 xenograft intensity (data not shown). Compared to untreated and scrambled siRNA-treated control cells, tumors with partial *LMNA* knockdown cells grew more rapidly (**Fig. 4-5C**). Importantly, the rates at which tumors doubled in normalized size were significantly higher within the first week (up to 3-fold) for knockdown tumors compared to controls (Fig. 4-5C inset), but the growth rates become similar, consistent with recovery from the transient knockdown (Fig. 4-4B, S4-7). The results provide a clear measure of the tumor propagation advantage for what *in vitro* studies show are more flexible nuclei.

Day-10 after cell injection, *LMNA* knockdown tumors remained significantly larger than controls. However, the difference was due only to the initial difference in growth rates because calculated doubling rates became similar between knockdown and control tumors after about one week. The timescale for recovery of *LMNA* expression after transient knockdown *in vitro* (**Fig. S4-7A**) is similar to the timescale here for the loss of difference in tumor growth rates (Fig. 4-5C inset), and Western blotting of late tumors indeed confirms human-*LMNA* expression similar to control levels (**Fig. 4-5D** inset). A transient knockdown thus produced a transient bulk tumor response, consistent with expectations.

Tumor cryo-sections were fixed and immunostained for human-LMNA and not only revealed a general co-localization of positively stained nuclei with tdTomato fluorescence but also showed a range of A549 nuclear shapes (Fig. 4-5D). Nuclei in the periphery of these dense

tissues appeared more elongated in comparison to nuclei in the tumor core within the same slice, consistent with *in vitro* observations of plastically elongated nuclei after migration through micropores (Fig. 4-2, 4-3A). Nuclear circularity was quantified and found to be statistically smaller at the periphery for knockdown nuclei relative to the tumor cores of both control and knockdown tumors ($p < 0.01$); control nuclei had an intermediate circularity, which perhaps indicates the slower growth (Fig. 4-5E). A mean circularity of about 0.82-0.83 for knockdown and control nuclei in the core compares well with the *in vitro* results of 0.83-0.84 for wildtype nuclei on the top of the micro-filter, and knockdown nuclei in the tumor periphery showed a decrease ($\Delta_{\text{Circ}} \approx -0.04$) similar to that seen *in vitro* (Fig. 4-2C).

4-3. Discussion

A cell and its nucleus contort and displace in diverse 3D-migration processes of development and regeneration as well as diseases such as cancer (Beadle et al., 2008; Pajeroski et al., 2007). Lamin-A varies more widely than Lamin-B's in health and disease (eg. Fig. 4-1B), and surprisingly the migratory cells here with the lowest levels of Lamin-A (U251 glioblastoma cells) show that moderate decreases in Lamin-A produce the greatest increase in 3D-migration (Fig. 4-1C inset). A549's express an intermediate level of Lamin-A:B, and moderate knockdown has an intermediate effect on their 3D-migration. Importantly, 2D-migration was unaffected for any cell type, and at least for the A549 cells migration was also unaffected through 8 μm pores that require much less distortion of the nucleus (i.e. $(\frac{3}{8})^2$). Past work had demonstrated a dependence of 3D- but not 2D- migration on cytoskeletal contractility with inhibition of myosin-II compromising migration of U251 cells through 3 μm pores but not through 8 μm pores or on surfaces (Beadle et al., 2008). Very similar effects of myosin-II inhibition were also

demonstrated here with A549 cells with Lamin-A knockdown or not (**Fig. S4-8**), which indicates that cytoskeletal forces actively push and pull the nucleus – whether wildtype or lamina softened – through a constraining pore. Key roles for the Lamins in 3D-migration are perhaps understandable intuitively, but scaling concepts from polymer physics help clarify the Lamin-A:B dependence as appears relevant to both biphasic motility with migration-coupled apoptosis and *in vivo* tumor growth.

4-3-1. Lamina polymer physics and distinct mechanical roles for Lamin isoforms

Previous fluorescence correlation spectroscopy (FCS) studies of GFP-Lamin fusion constructs had indicated that Lamin-A is mobile whereas Lamin-B's are relatively immobile (Shimi et al., 2008). Such findings are consistent with the basic results here that Lamin-A contributes as a viscous fluid to nuclear mechanics whereas Lamin-B contributes more as an elastic solid. However, FCS measurements had not suggested any dependence of mobility on Lamin-A concentration, whereas the nuclear response time correlation in Eq.2 here reveals a very strong power law scaling (exponent of 2.5) for the apparent viscosity contributed by Lamin-A. Importantly, the correlation (Fig. 4-1C) was obtained across multiple cell types that show some variation in Lamin-B, and it was also obtained with Lamin-A overexpressing A549 cells with constant Lamin-B. As mentioned, the data range spans viscosities as different as water and honey.

The response time τ for a viscoelastic system such as that schematized here (Fig. 4-2C inset) provides a measure of the time required for the energy stored upon rapid stretching of the elastic element to be dissipated by the viscous element. A response time for a typical oil is nanoseconds, whereas polymer melts have response times typically in the range of seconds to minutes

(Barnes 2000). In the present context, a rapid response time is expected of the oily hydrophobic core of the lipid bilayers that make up the nuclear envelope, whereas the dense network of interacting Lamins are rightly considered to be high molecular weight polymers that respond more slowly. Indeed, with high polymer concentration c in solution: viscosity $\sim c^{3.7}$ (Rubinstein and Colby, 2003). On the other hand, specific interactions of Lamin-A with Lamin-B (Schirmer and Gerace, 2004) provide a likely basis for the weak power law increase in the effective elasticity of the network with Lamin-A: $E(t) \sim c^{0.5}$ (Fig. S4-6D). These scaling results from simple polymer physics considerations thus suggest (viscosity/elasticity) $\sim c^{3.2}$, which is remarkably close to the $\sim c^{2.5}$ results obtained here for the Lamin-A:B ratio (Eq.2). Lamin-A thus contributes to nuclear mechanics as a highly concentrated, high molecular weight polymer that flows slowly and irreversibly like a plastic when stressed. This explains why the high Lamin-A:B ratio of MSCs produces the most elongated, extruded nuclei after hours-long migration through small pores.

Lamina polymer physics can also help explain the most fundamental observation here that moderate changes in Lamin-A have the *greatest effect on cells with the lowest levels of Lamin-A*. The nucleus is the rate-limiting factor in migration through small micro-pores, and so one can consider an Arrhenius-type model in which the rate k of a nucleus crossing the transwell filter is slowed exponentially by the work required ΔG by the cell to deform its nucleus: $k = k_0 \exp(-b \Delta G)$ with b as a constant. Importantly, higher Lamin-A:B gives a stiffer, more viscous nucleus (Fig. 4-3B, C, S4-5) that requires more work (ΔG) to deform. For simplicity, we assume a dependence of ΔG on [Lamin-A:B] that is close to the geometric mean of the effective elasticity $E(t)$ and the apparent viscosity of the nucleus, which gives the linear approximation: $\Delta G \sim$ [Lamin-A:B]. The ‘3D-migration sensitivity to Lamin-A’ defined in Fig.1C-inset is simply the

derivative of the rate, $\partial k / \partial \Delta G$, which is again an exponential. The prediction is thus that 3D-migration sensitivity to Lamin-A:

$$m_{3D-sens} \sim \exp(-b [\text{Lamin-A:B}]). \quad \text{Eq. 3}$$

Fig. 4-2C illustrates the predicted exponential decay. For similar reasons, the change in circularity of the nucleus (Δ_{Circ}) is also expected to depend exponentially on Lamin-A:B as shown (Fig. 4-2C, inset).

4-3-2. An optimal lamina for 3D-migration: low lamins limit survival under stress but high lamins immobilize cells

Stiffer materials generally withstand more stress before they break: they are stronger. Since wildtype cells generate sufficient stress in migration through small pores to apoptose and die (~12%; Fig. 4-4A, S4-4D), it is not surprising that Lamin-A knockdown (Fig. S4-6D) which softens nuclei (Fig. 4-2B,C) leads to an increasing proportion of both apoptotic cells and total cell loss (up to ~3-4 fold). The relevant molecular stresses were hinted at in proteomics analyses, which showed that although moderate knockdown of Lamin-A perturbs the proteome to a minimal extent (Fig. 4-1D), deep knockdown causes many major changes (Fig. 4-4B). The B-type Lamins change minimally as expected, and detected integrins increase about 2-fold which suggests that adhesion is adequate. The range of expression changes (see Supplemental Discussion) and the fact that embryonic stem cells also have very low Lamin-A and are very soft nuclei prompted an examination of at least a couple of core transcription factors, with both Oct-4 and Sox-2 appearing to increase about 2-fold after deep knockdown of Lamin-A (**Fig. S4-9**). However, the protein that is most obviously indicative of compromised stress resistance is

HSP90, which was suppressed almost as much as the transient knockdown of Lamin-A (4-fold or more). HSP's are involved in stabilizing or refolding proteins under stress conditions that could include the mechanical unfolding of proteins within contractile cells (Johnson et al., 2007). HSP90 also has a role chromatin or DNA repair (Dote et al., 2006), and a failure to repair DNA damage in 3D-migration would certainly promote apoptosis. Indeed, the HSP90 inhibitor 17-AAG increased apoptosis in the cells on the top of the filter that were just beginning to crawl through a pore, and apoptosis was even higher after Lamin-A knockdown (Fig. 4-3D). Moreover, this drug blocked migration through the pores regardless of Lamin-A level. The efficacy of 17-AAG as an anti-cancer agent in clinical trials (Goetz et al., 2005) may reflect some of these mechanisms of stressed migration.

For the xenografts, an initial proteomic analysis that distinguishes between proteins of human and mouse origin (Fig. S4-10, Table S4-2), indicated aberrant expression of the stress pathway proteins HSP90, STIP1 and AIFM1. These proteins all showed increased expression at 28 days in tumors generated after moderate Lamin-A knockdown compared to controls, although by this time point the transient knockdown had recovered (Fig. 4-5D inset) and slightly exceeded wildtype levels (Fig. 4-4B, Table S4-2). Apoptotic cell numbers in tumors could be low (Fig. 4-5A, right) for these reasons, but it is also likely that dead cells were rapidly cleared by tumor-associated macrophages.

Poor survival with low lamins and susceptibility to stress is likely to dominate the advantage in 3D-migration of a low Lamin-A nucleus which is easier to push or pull through a narrow constraint. PMNs (polymorphonuclear leukocytes) provide another important example of a cell type with very low lamins, a highly flexible nucleus, and an ability to invade any tissue during an infection, but these cells apoptose in days (Olins et al., 2001). In the opposite extreme, a nucleus that is simply too stiff for a given cell (with its characteristic cytoskeleton) to push or

pull the nucleus through a small opening will simply anchor the cell in place, as seen with Lamin-A overexpression in A549 cells here (Fig. 4-1C). Nonetheless, the large decrease in net migration from moderate to deep knockdown of Lamin-A (Fig. 4-1C) probably reflects additional defects here, especially in the cytoskeleton since inhibition of myosin-II also significantly impedes 3D-migration regardless of knockdown (Fig. S4-8). Nesprin-2 is substantially lower in Lamin-A knockdown (Fig. 4-4B,C), and although direct knockdown of this linker between cytoskeleton and nucleus impedes 2D-migration (Luxton et al., 2010), there are no reports yet linking Nesprin-2 to apoptosis. With Lamin-A knockdown tumors, α -actinin-4 is also low (Table S4-2 bottom), and knockdown of α -actinin-4 suppresses invasiveness of oral squamous carcinoma cells (Yamada et al., 2010). From these basic biophysical considerations of nucleus and the interconnected cytoskeleton emerges an expectation for biphasic 3D-migration *versus* Lamin-A levels, with implications for lamin variations in differentiation as well as disease.

Malignancies associated with increased levels of Lamin-A (Foster et al., 2010; Tilli et al., 2003) could therefore reflect the pro-survival function of Lamin-A in stressful 3D-migration of these cells. Xenograft studies here indeed show that Lamin-A levels can vary within a tumor (Fig. 4-5A), and Lamin-A levels can also impact the rates of tumor growth (Fig. 4-5C). The A549 cells studied here have more Lamin-A than Lamin-B (Fig. 4-1B), but there is also sufficient variation within a wildtype or knockdown cell population to produce more rapid 3-D migration of low Lamin-A cells, thus causing segregation *in vitro* (Fig. 4-3A). *In vivo* studies here likewise showed Lamin-A levels are lower in the growing periphery of the tumor than in the core (Fig. 4-5A), correlating with nuclear shape *in vivo* (Fig. 4-5D,E) despite the much more complex microenvironments than that used *in vitro* to reach similar conclusions (Fig. 4-3A). These latter findings seem especially pertinent to the low Lamin-A levels that have been associated with the recurrence of colon cancers (Belt et al., 2011). Explanations for both increases and decreases in

Lamin-A in processes such as tumorigenesis thus have a basis in the biphasic motility response (Fig. 4-1C).

Lastly, nuclear Lamins are of great interest not only in the context of disease, but also in aging, development and differentiation of stem cells (Akter et al., 2009; Frock et al., 2006; Scaffidi and Misteli, 2006). Specific or direct roles of Lamin isoforms seem controversial, with recent Lamin-B knockouts appearing surprisingly viable until birth when apoptosis in migration through the brain is apparent (Kim et al., 2011). Since Lamin-A is low in the brain and does not compensate, the fundamental insight here into lamina stabilization of the nucleus in 3D-migration explains the phenotype. Further understanding of the roles for both isoforms in cell migration speed and cell viability could be useful in fine-tuning cell behaviors *in vivo*, similar to PMNs, thereby contributing to cancer diagnostics as well as cell therapy with MSCs and perhaps other stem cells.

4-4. Conclusions

Biphasic dependence of cell migration on Lamin-A expression suggests complicated and contradictory roles of nuclear stiffness in cell behaviors. The results seem to imply the optimal nuclear stiffness for cell migration in dense tissue, whereas excessively stiff nucleus physically impedes migration while cells with too soft nuclei suffer from migration-induced mechanical stress and resulting apoptosis. This result may explain surprisingly short life span of PMNs after transmigrating into tissue, for these highly motile cells are known to possess significantly low lamins and are considered to be affected by migration-associated mechanical stress in tissues. Ex vivo analysis of growing tumors indicated slightly higher cell death frequency compared to base

line level determined with cell populations on the upper side of transwell filters. Smaller number of apoptotic cell in tumor in comparison with those found on the bottom side of transwell membrane could be explained by heterogeneous pore size of ECM mechwork since there should be a threshold for induction of migration-induced mechanical stress between 3 and 8 μm pore size, or rapid clearance of dead cells by tumor associated macrophages. Detailed mechanism of migration-induced cell death in constraining environment is still under investigation, but initial proteomic analyses indicated aberrant expression of stress-related proteins such as HSP90, STIP1 and AIFM1. Those stress-related proteins showed increased expression in siLMNA+ tumors after 28 days of in vivo growth and may explain suppressed elevation of growth rate observed in our in vivo experiments. The presented results here will help us understand the important roles of nuclear lamina serving at the same time as an obstacle against migration and as a resistance against mechanical stress to help completion of migrations.

4-5. Supplemental Discussion

Broad Proteomic Influences of Deep Lamin-A Knockdown

Among various changes, nesprin-2 down-regulation could be a part of the reason for suppressed migration. Nesprin-2 is linking nuclear lamina and cytoskeleton to coordinate nucleus and centrosome positioning, and previous study showed depletion of Nesprin-2 resulted in decreased 2D migration in fibroblasts (Luxton et al., 2010). The increase of expressions in integrin $\alpha 5$ and $\beta 1$, which form heterodimer to bind to fibronectin, could explain better migration of deep knockdown cells through fibronectin-coated filter compared to non-coating condition, matching the recent result where integrin $\alpha 5$ -downregulated lung carcinoma cells showed suppressed migration and tumor propagation (Roman et al., 2010). Although interaction between integrins $\alpha 5\beta 1$ and fibronectin is known to play important roles in various processes including migration and proliferation, one should be reminded that correlation of integrin expression level to the extent of those cell behaviors is still controversial due to contradictory results of previous works. Although contradictory to the hypothesis on suppressed migration with deep knockdown, the down-regulation of α -catenin is worth noting since reduced α -catenin is one of the markers of epithelial-mesenchymal transition (EMT) (Yang et al., 2004), in which carcinoma cells acquire mesenchymal cell-like properties and therefore become more migratory. Together with up-regulation of integrin $\beta 1$, which was previously shown to make migrating epithelial cells favor the mesenchymal-like motility (Friedl et al., 1997), A549 cells with significantly low lamin-A expression (particularly with deep knockdown ones) acquired more migratory mesenchymal-like phenotype, but with cytoskeletal defects that need to be elucidated, many of the cells failed to complete the migration. Those successfully left the monolayer on upper side of the transwell filter suffered from apoptosis caused by migration-associated mechanical stress. Proteome of lamin-A

deep knockdown A549 cells should need more detailed analysis to determine the mechanism of migration defect in those cells.

4-6. Materials and Methods

Cells and mice

Human lung carcinoma A549 and mesenchymal stem cells were purchased from ATCC and Lonza, respectively. Glioblastoma multiforme U251 cells were kind gift from Dr. Jay Dorsey. Cells were cultured in accordance with the supplier's instructions. Lentiviral particles encapsulating tdTomato-encoding plasmid were a kind gift from Dr. Carmine Carpenito. 10^5 A549 cells were incubated with lentivirus with MOI of approximately 7.5 for 24 hours. Cells were expanded following selection of tdTomato-positive cells, using a cloning cylinder (Bel-Art Products). Non-obese diabetic/severe combined immunodeficient (NOD/SCID) mice with null expression of interleukin-2 receptor gamma chain (NSG mice) were produced by the Stem Cell and Xenograft Core Facility at the University of Pennsylvania, using breeders obtained from the Jackson Laboratory (Bar Harbor). All animal experiments were planned and performed according to IACUC protocols.

Lamin-A knockdown and characterization

All siRNAs used in this study were purchased from Dharmacon. A549 cells were passaged 24 hours prior to transfection. A complex of siRNA (30 nM; siLMNA 1, 5'-GGUGGUGACGAUCUGGGCU-3' and siLMNA 2, 5'-AACUGGACUCCAGAAGAACAUC-3' (Elbashir et al., 2001)) and 1 μ g/mL Lipofectamine 2000 was prepared according to the manufacturer's instructions and incubated for 24 hrs per dose for up to three doses (in high glucose DMEM with 10% FBS for A549 and U251 and in low glucose DMEM with 10% FBS for MSC). Single 30 nM dose is denoted in this study as

“siLMNA+,” and three daily doses of 30 nM to achieve deep knockdown as “siLMNA++.” Results were compared with those using the same dose of scrambled siRNA. For untreated controls, an equal volume of opti-MEM (Invitrogen) was used. Knockdown efficiency was determined by Western blot following standard methods. Antibodies against Lamin-A (sc-7292) and β -Actin (sc-47778) were obtained from Santa Cruz Biotechnology (Santa Cruz). The effect of Lamin knockdown on cell proliferation was measured with thiazolyl blue tetrazolium (Sigma), following the standard MTT assay protocol.

2D and 3D migration assays

Stained cells were observed by epifluorescence microscope Olympus IX71 for all the experiments. 2D (wound healing assay): 10^5 A549 cells were seeded on 24-well plates. After 24 hrs, cells were treated with 1 dose of 30 nM siRNA (Lamin knockdown or scrambled) as described above. After 5 days, a scratch was made in the monolayer of cells and the width of the scratch measured in three places at 0, 3, 6 and 9 hrs. Lamin-A expression in migrating cells was measured by immunostaining cells at the wound frontiers. 3D (transwell migration assay): Multiwell inserts with filters of 3 μ m or 8 μ m pore were purchased from BD Biosciences. Fibronectin coating was achieved by incubation with 50 μ g/mL human fibronectin (BD Biosciences) solution for 2 hours at 37°C (Meng et al., 2009). 1×10^5 cells were seeded in serum-free medium in the upper well and DMEM supplemented with 20 % FBS was added to the bottom well to establish a nutrient gradient across the filter. For drug treatment during migration assay, 2 μ M of (-)-blebbistatin or 60 nM of 17-AAG (LC Laboratories) was added to both upper and bottom wells. In case of 17-AAG, cells were pre-treated with the drug for 24 hours before starting the assay. After incubation at 37°C with 5% CO₂ (24 hours for A549 and MSC, and 6

hours for U251 cells), cells were fixed with 3.7% formaldehyde (Fisher Scientific). Based on the necessity, cells were stained for: DNA with Hoechst 33342; Lamin-A (sc-7292); Lamin B (1° antibody sc-6217 from Santa Cruz Biotechnology); cleaved caspase-3 (1° antibody from Cell Signaling). After staining, filters were cut out from the insert, and mounted on cover slips using Fluoro-Gel (Electron Microscopy Sciences). 20x and 40x objectives were used for nucleus counting and caspase-3 observation, respectively.

Micropipette aspiration

Prior to aspiration experiment, cells were treated with 0.2 µg/ml of Latrunculin A (Sigma) for 1 hour at 37°C, detached with trypsin/EDTA, centrifuged and resuspended in aspiration buffer (135 mM NaCl, 5mM KCl, 5 mM HEPES, 1.8 mM CaCl₂, 2 mM MgCl₂, 2% BSA, 1:3000 propidium iodide (Molecular Probes)). Cell nuclei were stained with Hoechst 33342 (Molecular Probes). Nuclear compliance was measured as membrane extension under negative pressure inside a micropipette needle. Epifluorescence imaging was done with a Nikon TE300 inverted microscope coupled with a digital CCD camera (Roper Scientific), using a 60x oil immersion objective. Harvested A549 tumor tissues, pre-treated with collagenase (Sigma) or blebbistatin (Calbiochem) if necessary, were soaked in Ham's F-12 media (Invitrogen) during aspiration, visualized with 20x objective.

Quantitative proteomic profiling

Cell or tissue lysates were run on SDS-PAGE and the 60 – 80 kDa molecular weight range excised from the gel. Samples were prepared, run on LC-MS/MS (LTQ-Orbitrap, Thermo Fisher

Scientific) and analyzed by a combination of Elucidator (Rosetta Biosoftware) and in-house software, as described previously (Shin et al., 2011).

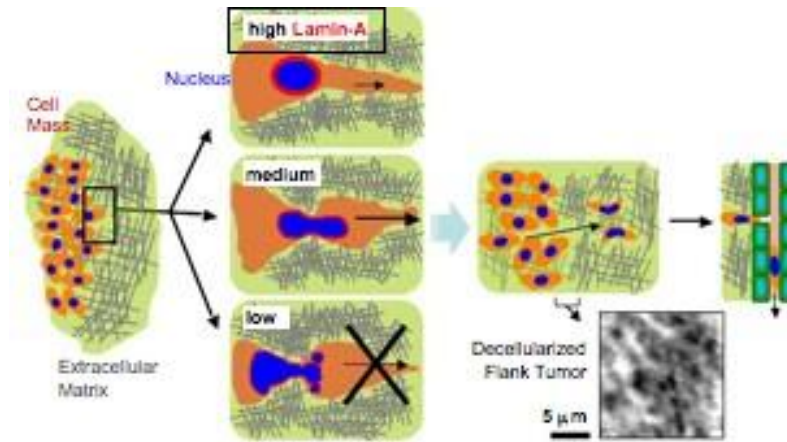
Establishment of A549 tumors in mice

tdTomato-expressing A549 cells were detached with trypsin, washed with PBS, and suspended in PBS containing 25% Matrigel (BD biosciences) at a concentration of 2×10^7 cells/mL. Each mouse received two injections of one million cells at two flank sites, siLMNA-treated cells on one side and control cells on the other. Tumor progression was evaluated by tdTomato fluorescence emission from tumors using an IVIS Spectrum Imaging System (Caliper Life Sciences), imaged with 535/640 nm excitation/emission. Image analysis was done with Living Image Software (Caliper Life Sciences). Tumors were grown for 28 days before harvesting. Tumor slices (10 μ m thick) were fixed with 3.7% formaldehyde, permeabilized with 0.25% Triton X-100, and blocked with BSA. Tissue was stained for human Lamin A and nuclei were counterstained with Hoechst 33342, and then observed with 40x objective. Tissue remaining after cryo-sectioning was lysed in RIPA buffer and prepared for MS and Western blotting following standard protocol found elsewhere. For tumor tissue decellularization, tissue was first soaked in 1% SDS (BIO-RAD) solution and incubated at r.t. overnight with one solution exchange. Then tissue was washed with 1% Triton X-100 solution for 30 min at r.t., followed by equilibration with PBS.

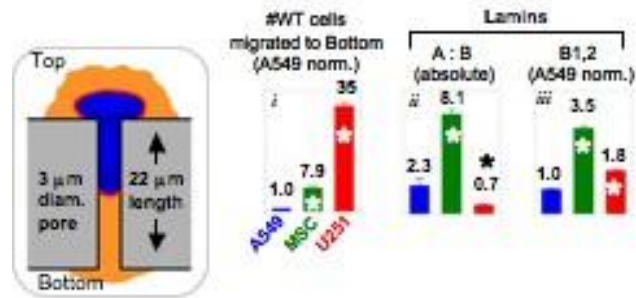
Intracellular staining of Lamins in tumor-derived A549 cells

After harvested, A549 tumors are separated into core and peripheral portions, further cut into smaller pieces of ~few mm³. Tumor tissue pieces were incubated in F-12 growth medium containing 0.2 mg/mL collagenase (Sigma) at 37°C with 5% CO₂ for 0.5-1 hour. Isolated cells were collected and fixed/permeablized using flow cytometry fixation/permeabilization buffer (R&D systems), following manufacturer's instructions. For cultured A549 cells, fixation and permeabilization was done using 3.7% formaldehyde and 0.25% Triton X-100 (MP Biomedicals) in PBS, respectively. Cells were stained for Lamin-A and B with Alexa-488 and -647 conjugated secondary antibodies (all samples were treated with antibodies of fixed concentration ratio), respectively, and intensities were measured with FACSCalibur (BD Biosciences). Apoptotic cells were detected based on positive signal for both Lamin-A (stained with Alexa 488 secondary antibody) and cleaved capasease-3 (Alexa 647) by microscopic observation with 20X objective lens.

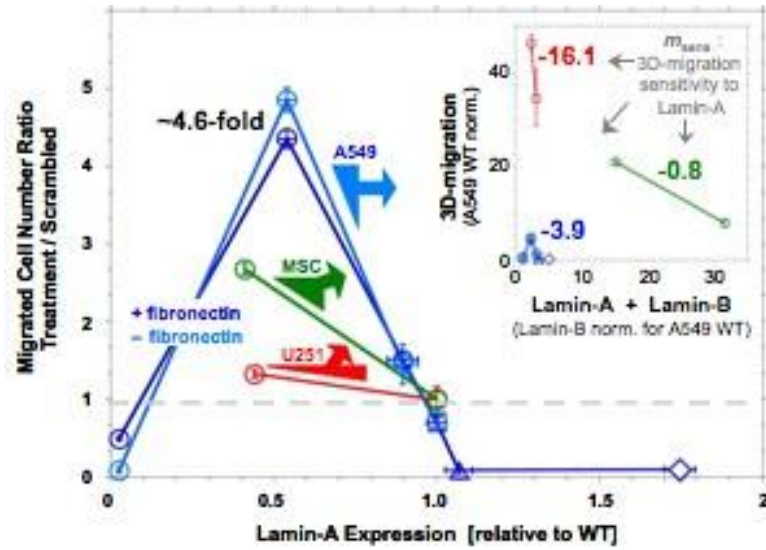
A



B



C



D

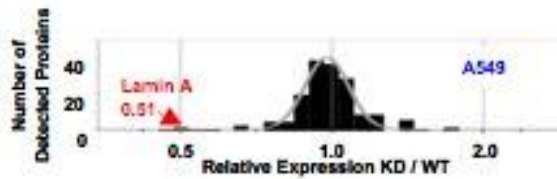
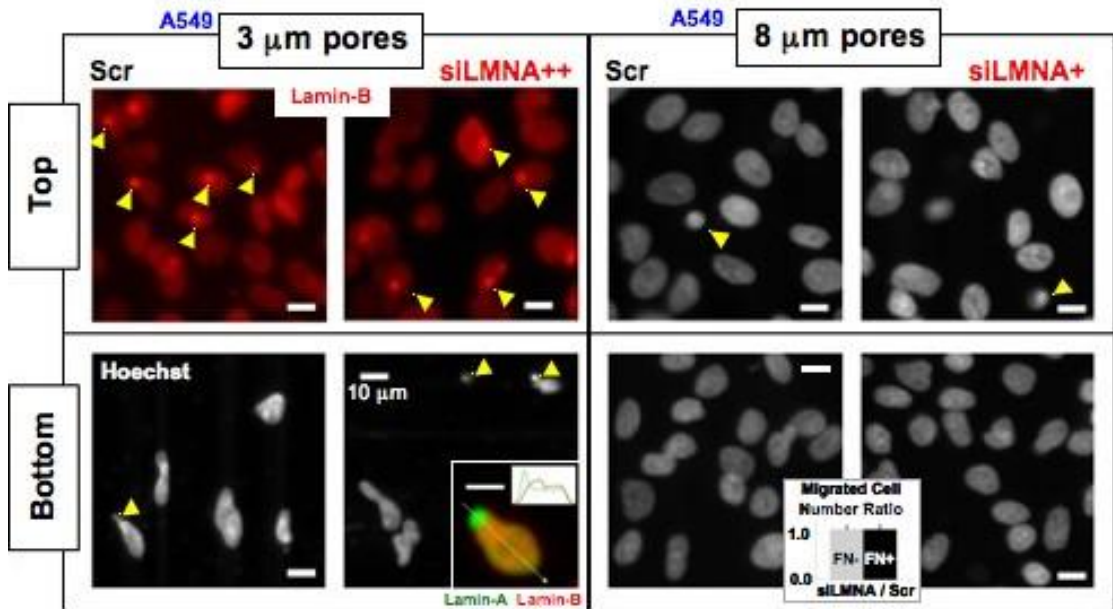


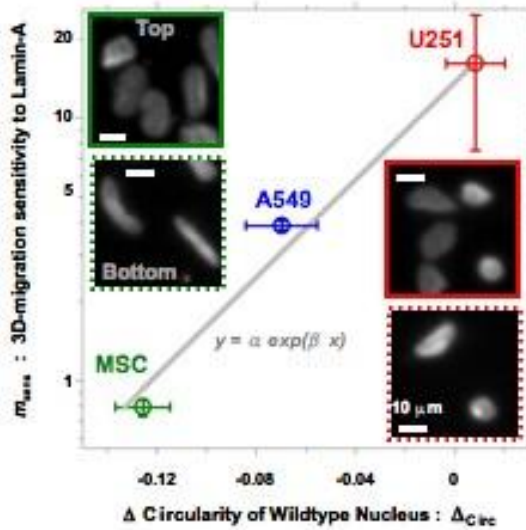
Figure 4-1. **3D-migration is sensitive to Lamin-A levels even in the absence of major proteomic changes.** (A) Hypothesis for the impact of Lamin-A levels on migrating cells. While moderate expression permits migration, cells with low levels cannot withstand the stress and high levels impede migration. Inset: brightfield image of detergent-decellularized tumor, where dark regions corresponding to pores. (B) Wildtype 3D-migration through transwell filter (*i*, schematic) and lamina parameters (*ii*, *iii*) for: A549 (blue), MSC (green) and U251 (red) cells. ($n \geq 3$; \pm SEM; $*p \leq 0.05$). Calculations of Lamin isoform levels are in Fig. S3C. (C) Lamin-A dependence of net cell migration to the Bottom of the filter (main plot, $n \geq 3$; \pm SEM). Normalization is done to scrambled siRNA-treated cells, with Lamin-A level determined by western blot. Filters were pre-coated with fibronectin coated unless indicated. Circles: siLMNA-

treated cells. Squares: untreated. Triangle and diamond: A549 cells transduced with GFP-Lamin-A with low and high levels, respectively. Inset plot, migration results rescaled to Lamin-(A+B) levels (also see Fig. S3C) and net migration relative to wildtype A549 cells (Fig. 1B left bargraph). The indicated slopes represent the 3D-migration sensitivity to a moderate Lamin-A change in each cell type. **(D)** Negligible disruption to the A549 proteome after 50% knockdown of Lamin-A is evident in a narrow, log-normal distribution relative to wildtype cells.

A



B



C

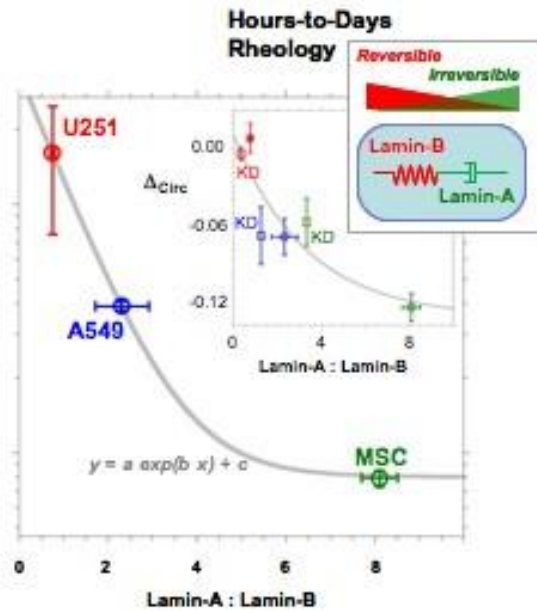
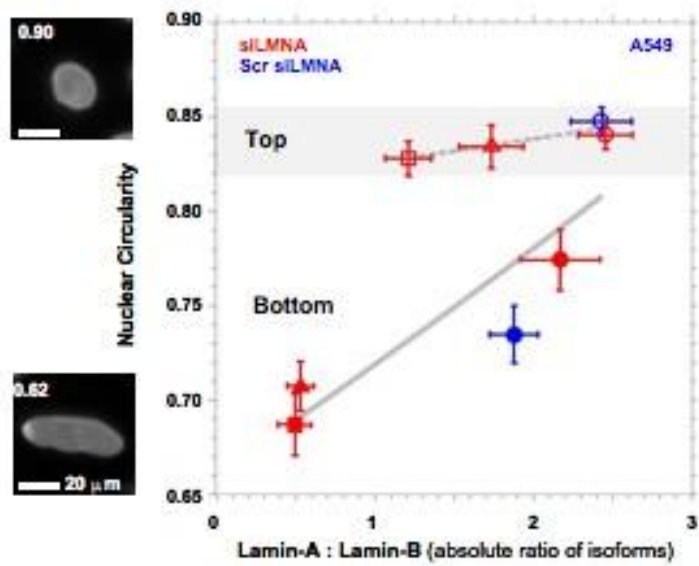
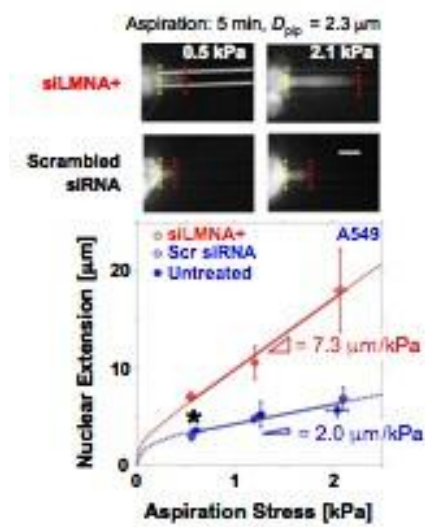


Figure 4-2. **Lamin-A plasticizes nuclei, with persistent shape changes correlating with both 3D-migration sensitivity to Lamin-A and also with the Lamin-A:B ratio.** (A) Images of nuclei on the micro-pore filters stained for either Lamin-B or DNA (Hoechst 33342). Arrowheads indicate a nucleus in a pore, either partially or completely. Knockdown with siLMNA was >95% (3 μm) or 60% (8 μm). Inset image of siLMNA cell with nucleus coming out of the bottom of 3 μm pore and showing segregation of lamin-A from lamin-B as clarified by line intensity profiles. Inset bargraph: net migration ratio with 8 μm pore filters shows no effects of Lamin-A knockdown for both fibronectin-coated and uncoated filters ($\pm\text{FN}$). (B) Exponential correlation between 3D-migration sensitivity to Lamin-A levels (values in Fig. 1C inset) and the difference in circularity of wildtype nuclei on the top versus the bottom of 3 μm filters ($n > 60$; $\pm\text{SEM}$). Inset images: nuclear shapes on top and bottom of filters. The three datapoints fit well with two parameters: $\alpha = 14$, $\beta = 23$ ($R^2 > 0.99$). (C) Exponential decay of migration sensitivity with Lamin-A:B ratio. Inset plot shows negative correlation of migration-induced nuclear circularity change with Lamin-A:B ratio. All data points fitted to exponential decay equation. Exponential fit is approximated from panel-(B), but with fit parameters: a ($\approx \alpha$) = 33, $b = -1$, c (≈ 0) = 0.8 ($R^2 > 0.99$). Inset scheme illustrates distinct physical roles of Lamin-A and Lamin-B as influencing, respectively, nuclear viscosity (dash pot) and nuclear elasticity (spring).

A



B



C

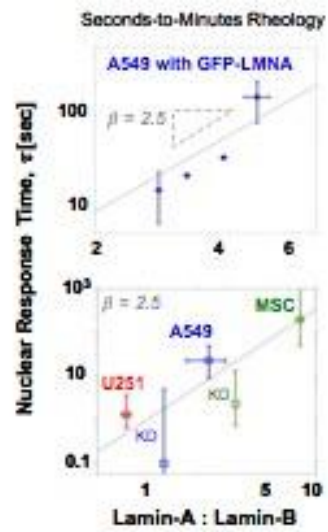
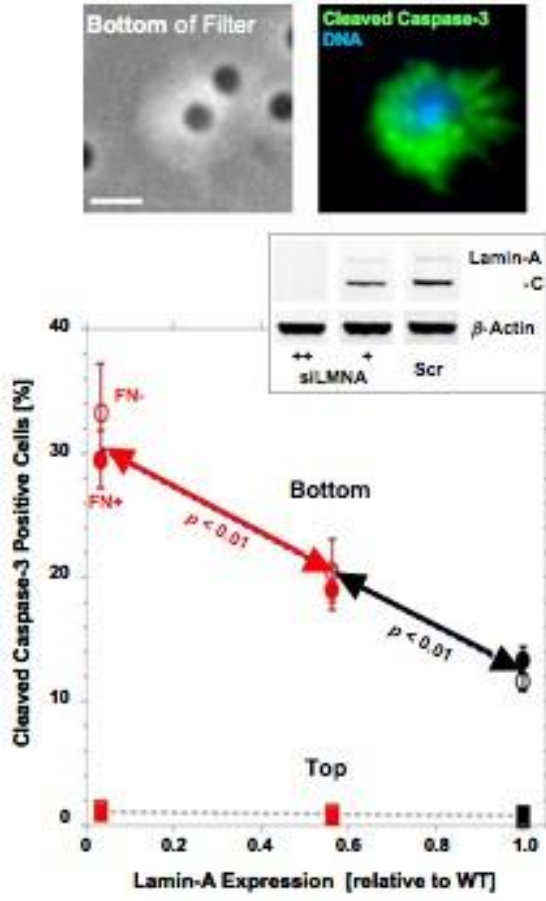


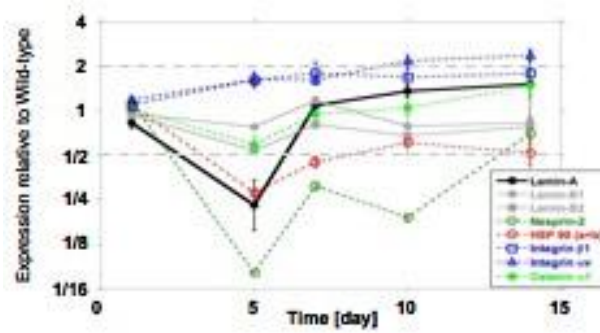
Figure 4-3. Variations in Lamin-A lead to cell sorting in 3D-migration, consistent with Lamin-A:B regulation of nuclear response time. (A) Nuclei on the bottom of the filters

compared to the top show a lower absolute ratio of Lamin-A:B and also lower nuclear circularity ($n \geq 50$; \pm SEM), consistent with segregation in 3D-migration based on softness of the nucleus. The immunofluorescence results for intensity of Lamin-A (shown) and Lamin-B were re-scaled to the absolute ratio of 2.3 (Fig. 1B-ii). Red circle, triangle and square symbols correspond to high, medium and low doses of siLMNA, respectively. Results are fit segmentally to exponentials: $y = 0.81 \exp(0.015 x)$ (top, $R^2 = 0.86$) and $y = 0.66 \exp(0.083 x)$ (bottom, $R^2 = 0.78$). (B) Fluorescent microscope images of aspirated nuclei stained with Hoechst 33342 under high (~ 2.1 kPa) and low (~ 0.5 kPa) pressure. Plot shows nuclear membrane extension under different aspiration pressures after 5 min ($n = 4$; \pm SEM; $*p < 0.01$). See Methods for cell treatments. Controls are both non-treated and scrambled siRNA-treated cells fitted to single line. Scale bar is 5 μ m. (C) Power law dependence of nuclear response time, τ , on Lamin-A:B for individual Lamin-A overexpressing cells (top) and the three cell lines including knockdown cells (bottom, $n \geq 4$; \pm SEM). Aspirated lengths were rescaled by pipette diameter and pressure (to J in Fig. S6A), and the various response times were obtained for 2.5 kPa^{-1} ($= J$ for upper plot) and 7 kPa^{-1} ($= J$ for lower plot). $\beta (= 2.5)$ is the fitted power law exponent.

A



B



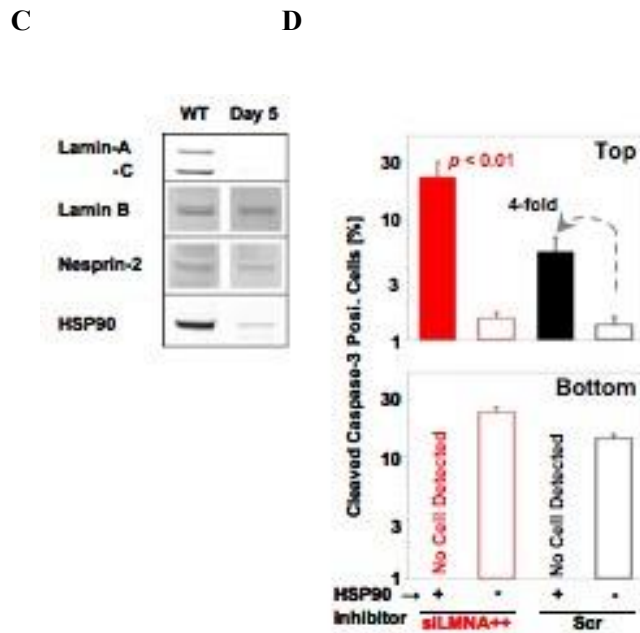
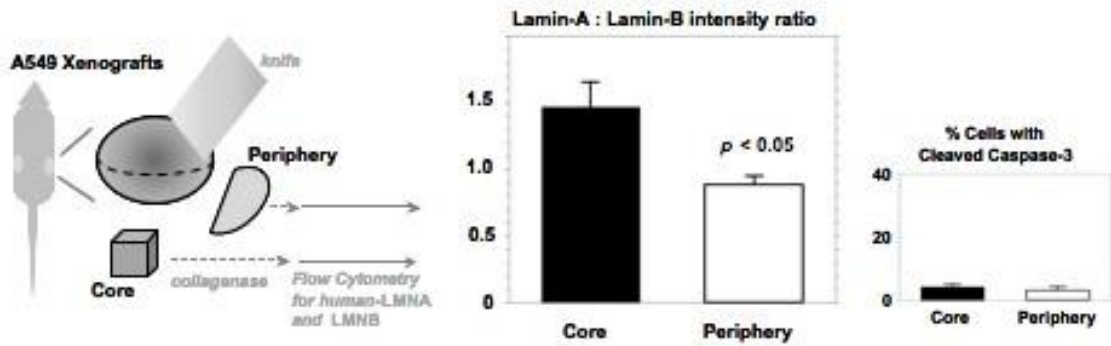


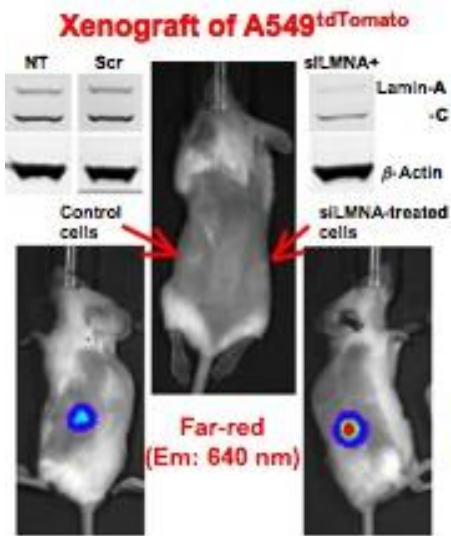
Figure 4-4. **3D-migration enhances apoptosis, and ablation of Lamin-A compromises HSP90-dependent, stress protection.** (A) Images show an A549 cell that is still partially in a 3 μm pore (left panel) and staining positive for the apoptosis marker cleaved caspase-3 (green, right panel; blue, DNA Hoechst 33342). Scale bar is 10 μm . The plot shows the increased frequency of apoptotic A549 cells on the bottom of 3 μm pore-filter after Lamin-A knockdown, as measured by Western blots (inset). Cells on the top show a negligible dependence of apoptosis on Lamin-A. ($n = 10$; $\pm\text{SEM}$). Filled and open symbols represent fibronectin-coated and uncoated filters, respectively. (B) Changes in the expression levels of proteins of interest, detected by quantitative mass spectrometry, following transient Lamin-A knockdown and recovery over 14 days ($n = 3$; $\pm\text{SEM}$). (C) Changes in Lamin-A, Lamin-B, Nesprin-2 and HSP90 were confirmed by Western blot for wild-type and 5-day post-knockdown cells. (D) Upper plot: Apoptosis in cells on top side

of 3 μm pore filter increased with 17-AAG treatment (filled bars, 60 nM) in comparison with DMSO control (open bars). Apoptosis was enhanced by Lamin-A knockdown. Lower plot: 17-AAG-treated cells were not found on the bottom of the filters, indicating a complete failure to migrate through 3 μm pores when HSP90 is inhibited. ($n = 10$; $\pm\text{SEM}$).

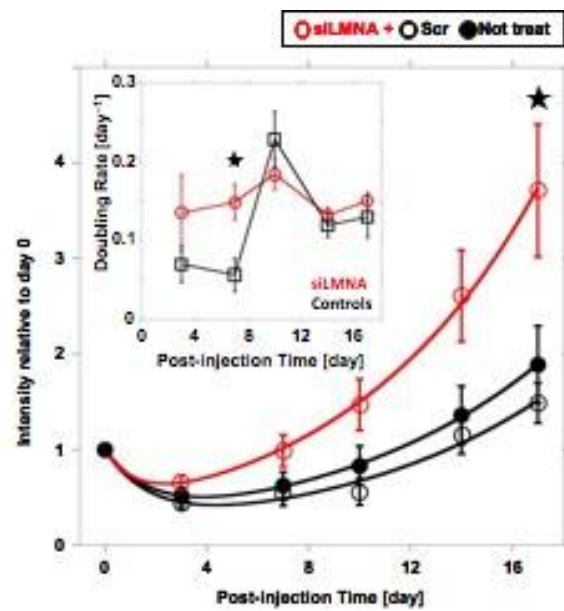
A



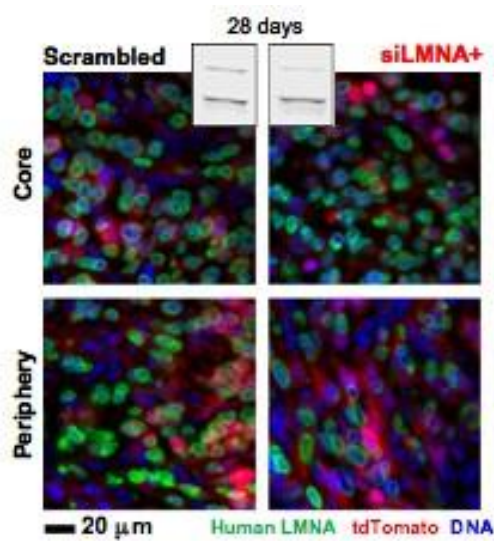
B



C



D



E

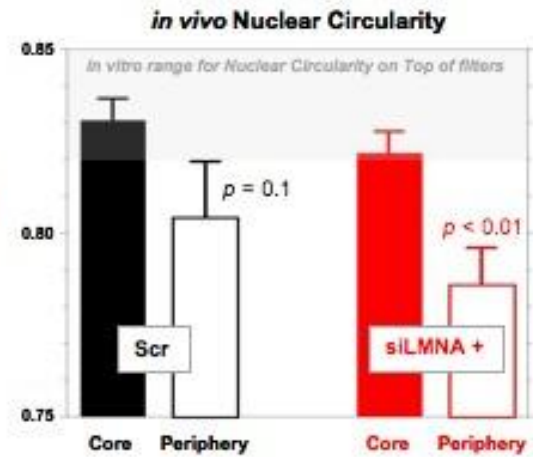
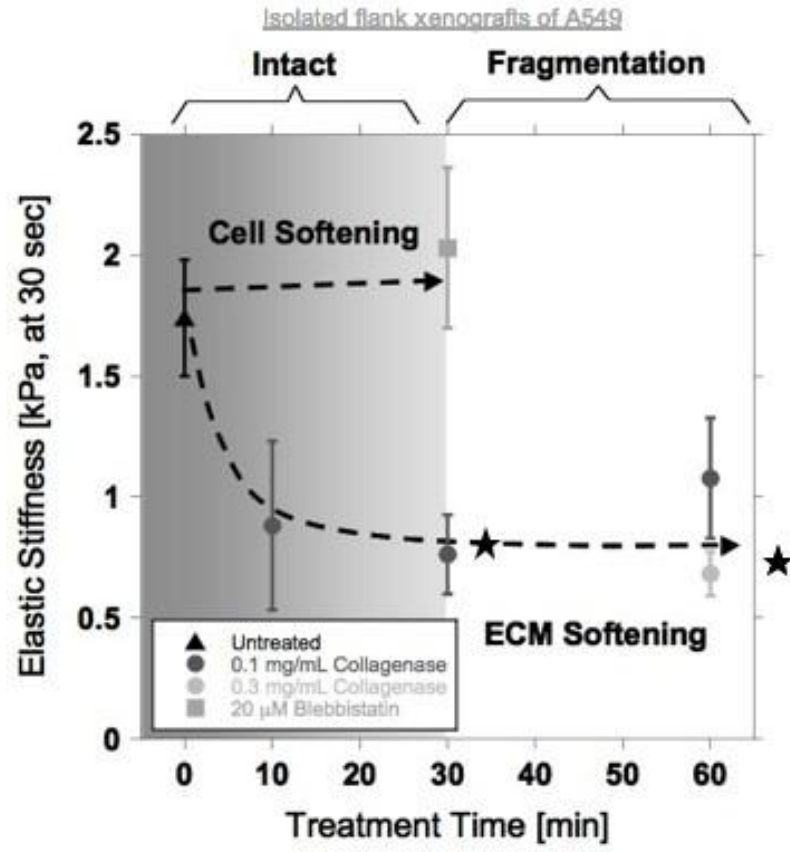


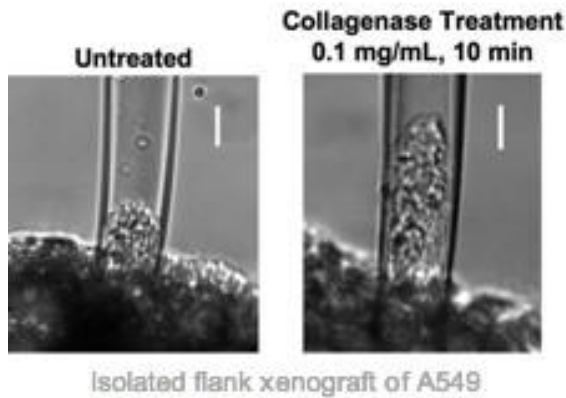
Figure 4-5. Cells in the tumor periphery show low Lamin-A:B in more deformed nuclei, consistent with enhanced tumor growth after moderate knockdown of Lamin-A. (A) (Left scheme) Intracellular immunostaining of lamins in A549 cells isolated from core and peripheral portions of wild-type tumors followed by flow cytometry measurements. (Center bargraph) A549 cells were distinguished from mouse cells based on positive staining with human specific Lamin-A primary antibody. Lamin-A:B intensity ratio showed a statistically significant difference between core and periphery-derived cells ($n = 6$; \pm SEM). (Right bargraph) Frequency of cleaved caspase-3 positive tumor-derived A549 cells were obtained by imaging cells positively stained for both human Lamin-A and cleaved caspase-3 ($n \geq 46$; \pm SEM). (B) *In situ* imaging of A549 cells that were stably expressing tdTomato and xenografted into subcutaneous flank sites of NSG mice. Each mouse received siLMNA-treated cells in one side and control cells, untreated (NT) or scrambled-RNA (Scr), on the opposite side. Lamin-A knockdown was confirmed by western blot

analysis. (C) Tumor propagation measured by tdTomato signal from tumors up to 17 days post-engraftment, with double exponential fits of growth ($n = 10$ for siLMNA+, $n = 5$ for NT and Scr; \pm SEM). Inset: Growth rates as reciprocal doubling times calculated from consecutive time points ($n = 10$; \pm SEM; $p < 0.05$). (D) Representative fluorescence images of cells in core and periphery regions of tumor tissue sections, stained for DNA (Hoechst 33342, blue) and anti-(human Lamin-A) (green) with red fluorescence from tdTomato. Inset: Westerns of tumors with anti-(human Lamin-A) and constant total protein show Lamin-A,C has recovered after moderate knockdown. (E) Circularity analysis of A549 nuclei in control or Lamin-A knockdown tumor tissue slices ($n \geq 25$; \pm SEM). Cell populations were divided into core and periphery as in (A). ($n = 4$ tumors).

A



B



C

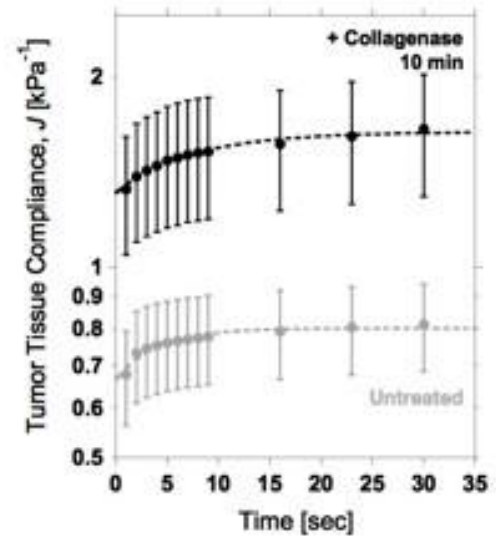
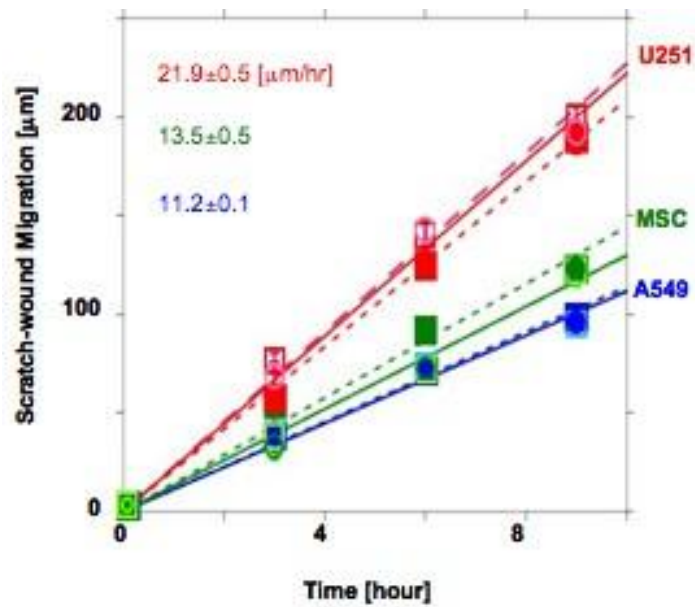


Figure S4-1. **Matrix-dictated Stiffness of Tumor Tissue** (A) In addition to untreated condition, tumors were either treated with collagenase (ECM degradation or softening) or blebbistatin (cell softening) with different concentration and treatment time ($n \geq 5$; \pm SEM). Stars represent statistically significant difference ($p < 0.05$) from untreated tissue. Elastic stiffness was calculated according to previous work (Dahl et al., 2005). (B) Representative images of aspirated tumor tissues with (right) or without (left) 0.1 mg/mL collagenase treatment for 10 min. Scale bar is 20 μm . (C) Averaged compliance of aspirated tumor tissues under constant pressure (19.8 ± 0.8 kPa for untreated tissues and 19.4 ± 0.6 kPa for collagen treated tissues), measured over 30 sec of aspiration ($n \geq 5$; \pm SEM).

A



B

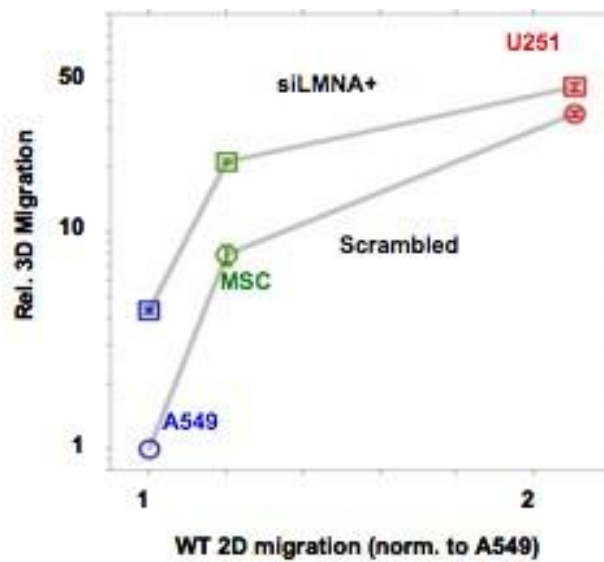
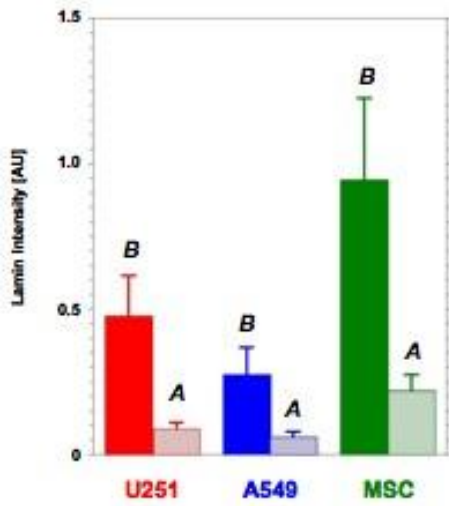


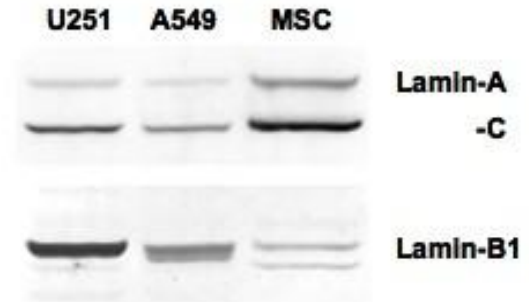
Figure S4-2. Moderate changes in Lamin-A do not affect 2D migration, but 2D migration always correlates positively with 3D migration (A) Wound scratch healing assay for Lamin-A

knockdown (open circles) as well as untreated (open squares) and scrambled siRNA-treated (filled squares) A549, MSC and U251 cells ($n > 3$; \pm SEM). (B) Relative migration efficacy of siLMNA+ and control siRNA-treated cells is plotted against relative migration velocity on surface measured in Fig. S2A for A549, MSC and U251. Control siRNA-treated A549 is set as 1 for both axes.

A



B



C

	Relative to A549			
	A : B (WB)	B (IF)	A	A+B
U251	0.74	1.75	1.30	3.05
A549	2.30 (MS)	1.00	2.30	3.30
MSC	8.10	3.48	28.17	31.64

Lamin-A = A:B (1st column) × B (2nd)

A+B = B (2nd) + A (3rd)

A:B was measured by mass spectrometry for A549, and calculated based on Western blot results for MSC and U251.

B was measured by immunofluorescence, and relative values were calculated with A549 as 1.0.

D

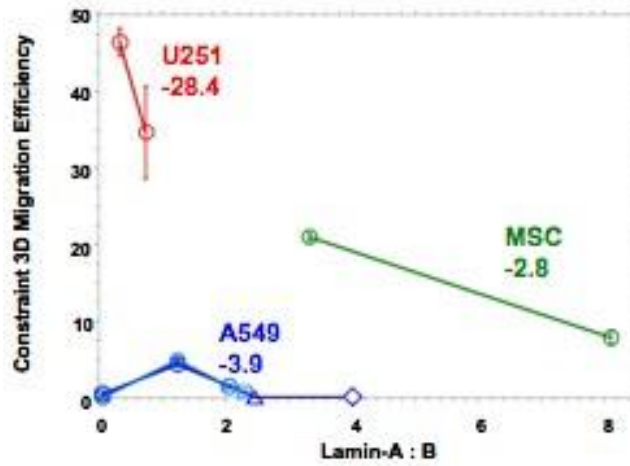
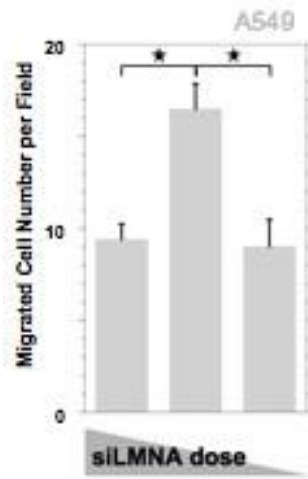
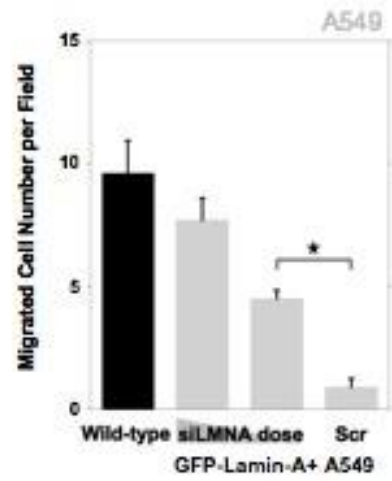


Figure S4-3. Cells with distinct origins and Lamin profiles demonstrate varied 3D migration sensitivity to Lamin-A change (A) In vitro immunofluorescence for Lamin isoforms A and B. Error bars represent standard deviation ($n > 120$; \pm SEM). (B) Western blots of Lamin isoforms for A549, MSC and U251. (C) Table summarizing Lamin-A:B, B, A and A+B values for A549, MSC and U251 cells. Calculations used for obtaining values appearing in inset bar graphs of Fig. 1B are shown below. (D) x- and y-axes are rescaled from Fig. 1C main plot values to Lamin-A:B and relative migration capacity of control cells ($n \geq 10$; \pm SEM). Values in the plot are gradient of migration against Lamin-A:B change by $\sim 50\%$ Lamin-A knockdown.

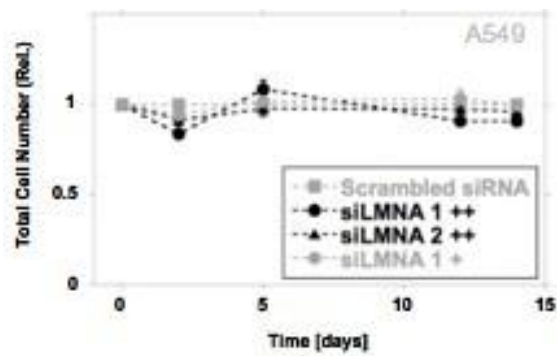
A



B



C



D

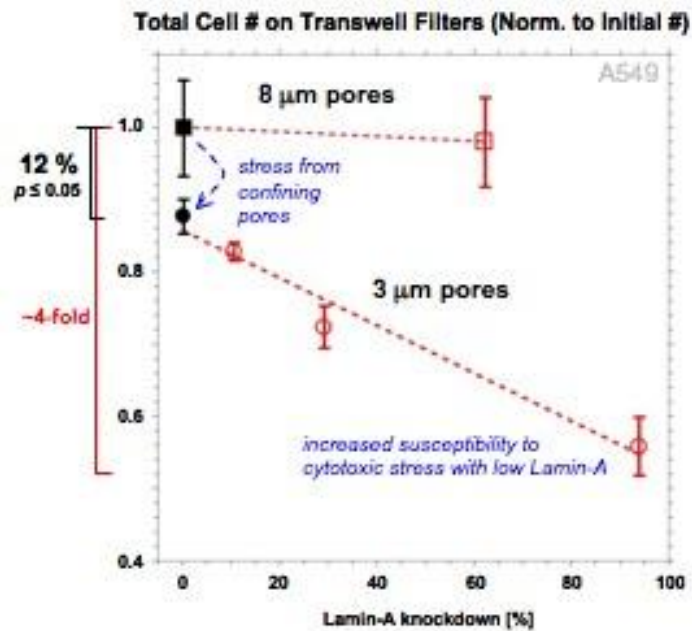
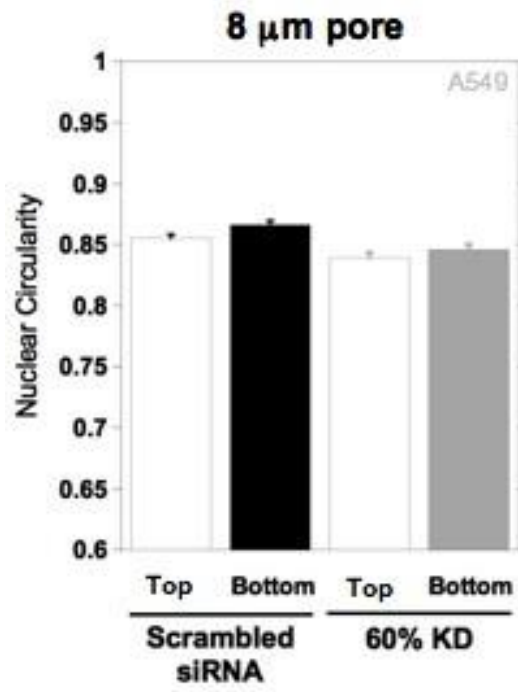


Figure S4-4. siLMNA's with distinct targets consistently increase 3D migration without affecting viability in 2D or in migration thru large pores, but cell numbers are reduced with small pores and with knockdown (A) Recovery of suppressed migration capacity in GFP-Lamin-A overexpressing A549 cells by partial Lamin A knockdown (n = 10; \pm SEM; star $p < 0.01$). (B) Non-linear dose dependence of A549 migration (3 μ m pores) with siLMNA 2 (n = 10; \pm SEM; star $p < 0.01$). (C) Cell proliferation assay of siLMNA-treated cells, showing relative cell viability against scrambled siRNA control on the same time points (n = 2; \pm SEM). (D) Relative total cell numbers on both sides of transwell filters (Number of scrambled siRNA-treated cells on 8 μ m-pore filter after 24 hours as 1, with the same initial number of cell seeded for all conditions) for A549 cells treated with scrambled siRNA or different doses of siLMNA (n = 3; \pm SEM; star $p < 0.05$).

A



BC

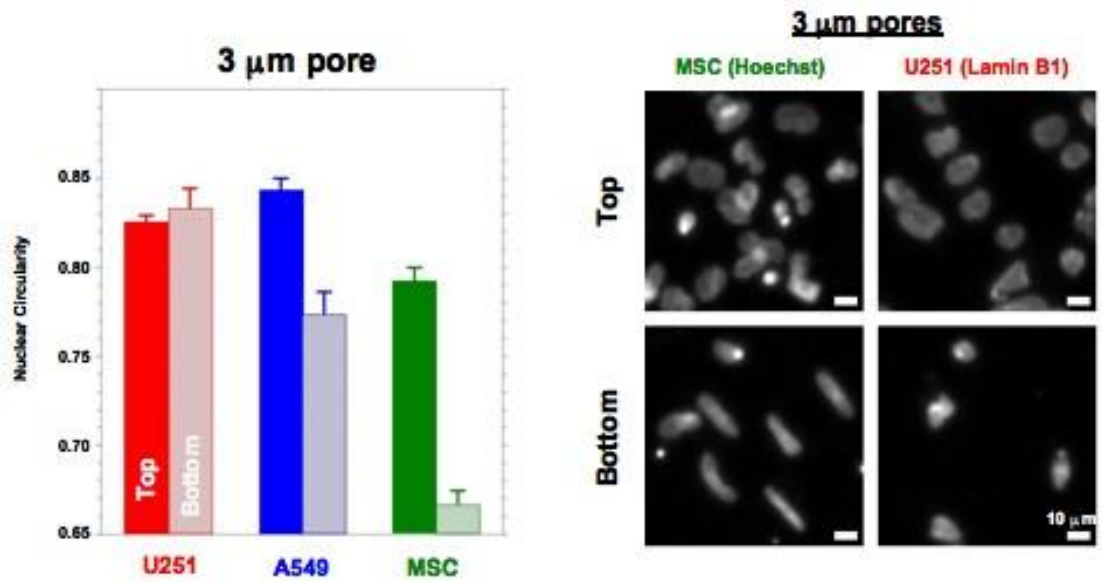
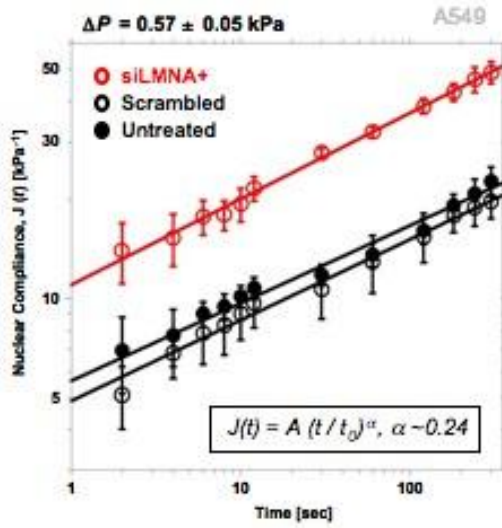
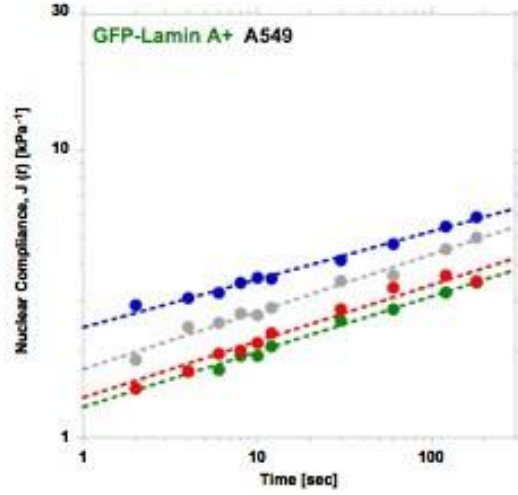


Figure S4-5. **Extent of nuclear deformation by small pore migration shows cell-type specificity** (A) Negligible influence of migration through 8 μm -pore filter on nuclear circularity, irrespective of Lamin-A knockdown ($n > 160$; $\pm\text{SEM}$). (B) Comparison of nuclear circularity change after migration through 3 μm -pore filter for A549, MSC and U251 cells (scrambled siRNA-treated). $n > 70$; $\pm\text{SEM}$. (C) Representative images of nuclei of MSC and U251 cells on top and bottom sides of transwell (3 μm) filter.

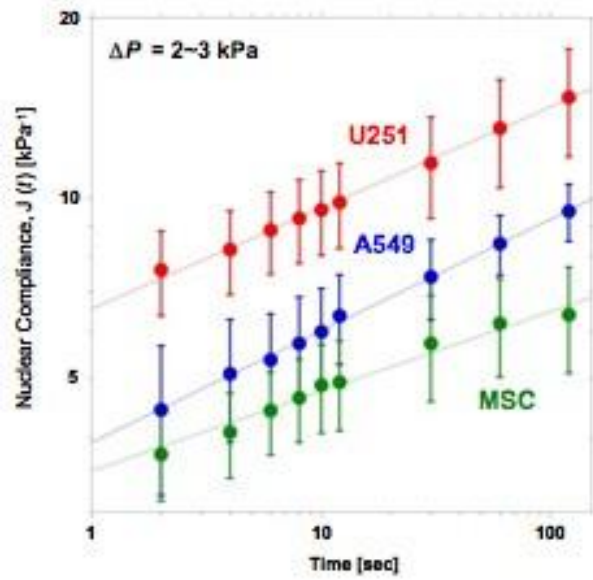
A



B



C



D

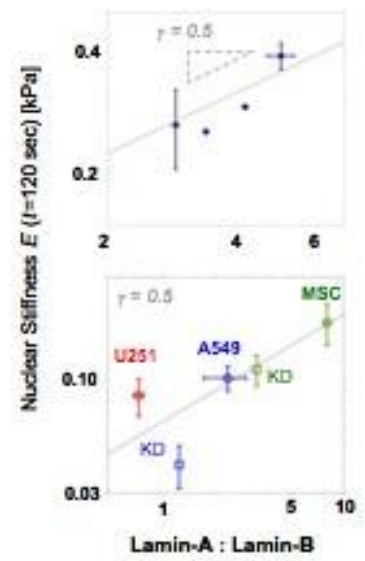
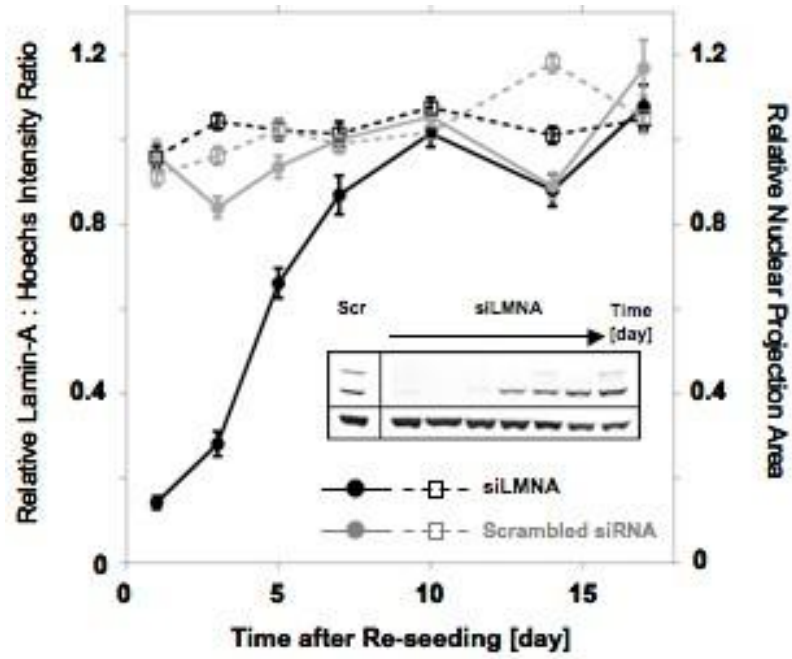
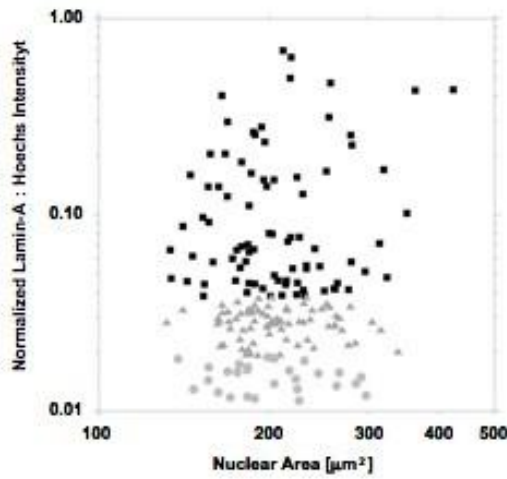


Figure S4-6. **Micropipette aspiration reveals Lamin-A dependence of nuclear stiffness and elasticity** (A) A549 nuclear compliance change with time under constant pressure (~0.5 kPa) with a power law fit for siLMNA+ and control cells (n = 4; \pm SEM). (B) Nuclear Compliance of GFP-Lamin-A overexpressing A549 cells. (C) Nuclear compliance change with time of A549, MSC and U251 cells under 2-3 kPa pressure (n \geq 4; \pm SEM). (D) Nuclear elastic stiffness obtained with micropipette aspiration for GFP-Lamin-A overexpressing A549 cells (upper) and the three cell lines (bottom, n \geq 4; \pm SEM).

A



B



C

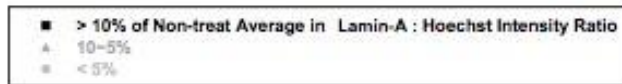
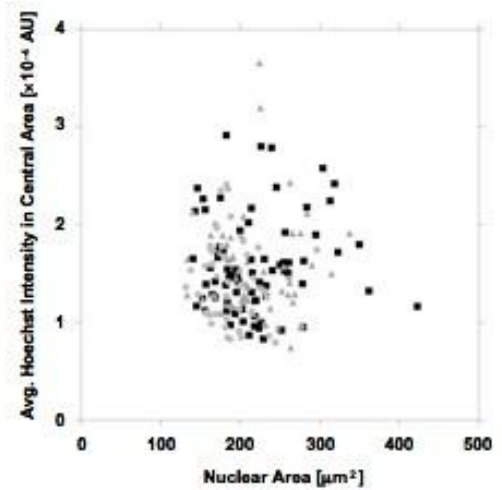


Figure S4-7. **Transient Lamin-A knockdown causes little change in nuclear volume** (A) Changes in normalized Lamin-A expression (filled circles) and projected nuclear area (open circles) after either siLMNA or scrambled siRNA treatment were monitored over 17 days ($n > 50$; \pm SEM). Inset is western blot image of A549 cells treated with either scrambled siRNA (Scr) or siLMNA. For siLMNA treatment conditions, A549 cells were collected for western blot measurements at different time points corresponding to the ones on the main plot. The bands correspond to Lamin-A, Lamin-C and β -Actin from top to bottom. (B and C) Subpopulation analysis of Lamin-A knockdown cells from day 1 post-transfection. Cells divided into subgroups based on Lamin-A expression level (B), and nuclear area vs. averaged Hoechst 33342 intensity in small area at center of nucleus, representing nuclear height, was compared between subgroups (C).

A

B

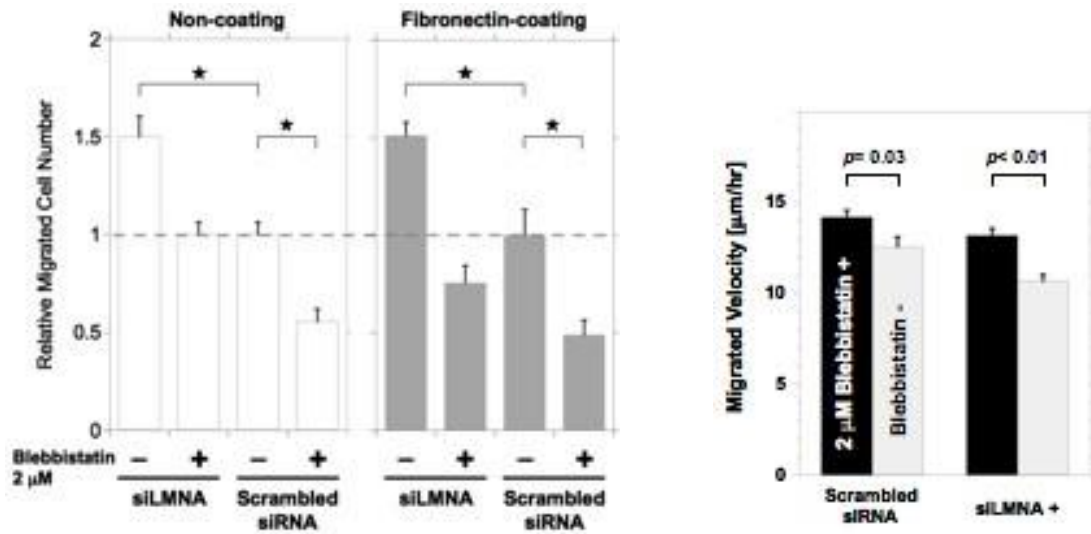
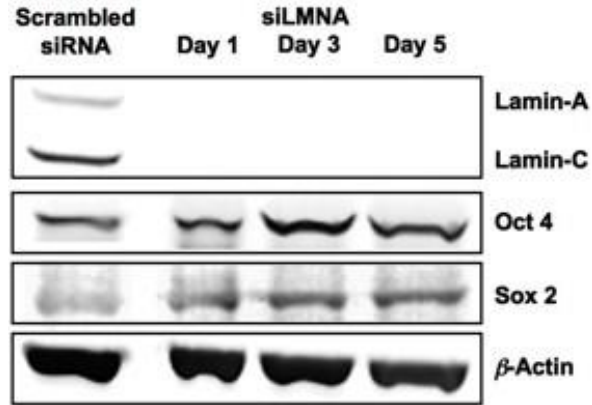


Figure S4-8. **Mosin II-dependent A549 migration** (A) Trans-well migration assay under the treatment with myosin II inhibitor blebbistatin. A549 cells with Lamin-A knockdown were induced to migrate through 3 µm pores in the presence of 2 µM blebbistatin with no coating (left) or fibronectin coating (right). Stars represent statistically significant difference ($n \geq 18$; \pm SEM; star $p < 0.05$). (B) Effect of blebbistatin (2 µM) treatment of 2D migration velocity of A549 cells, either treated with siLMNA+ or control siRNA ($n = 3$; \pm SEM).

A



B

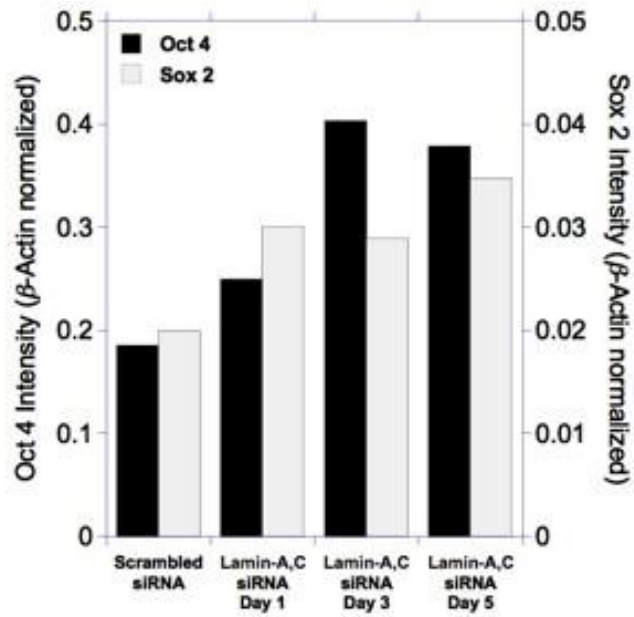


Figure S4-9. **Deep Lamin-A knockdown Induces up-regulation of pluripotency markers (A)**

Western blot for wild type and Lamin-A deep knockdown A549 cells at several time points during siLMNA⁺⁺ treatment. Both antibodies for oct 4 and sox 2 were purchased from Novus

Biologicals. (B) Intensity values obtained in (A) are summarized. Intensities are normalized by those of β -Actin.

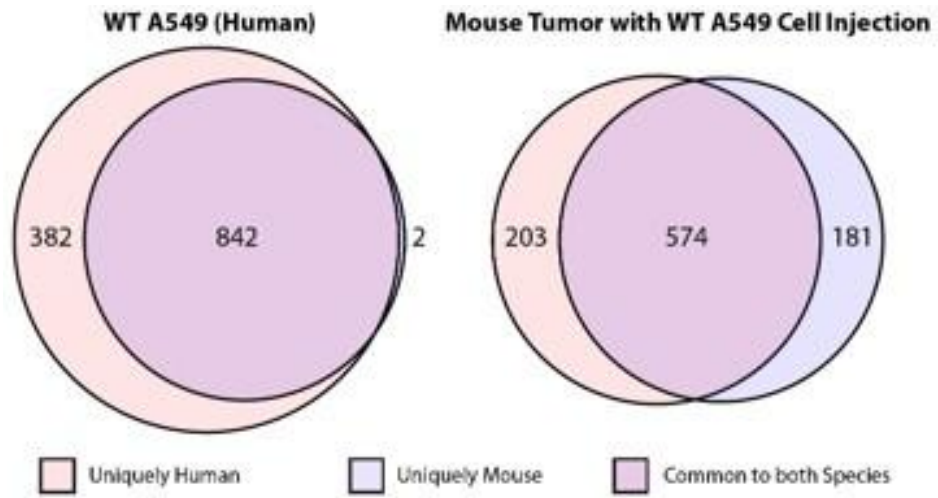


Figure S4-10. **Label-free mass spectrometry distinguishes human- and mouse-specific proteins** Venn diagrams showing sequence overlap of A549 proteins detected in vitro (left) and human- and mouse-unique proteins detected from harvested tumors (right).

Table S4-1. **Proteome of Lamin-A moderate knockdown A549 cells** Comparison of proteome between wild-type and 50% Lamin A knockdown A549 cells. Values in heat-map represent relative expression between knockdown and wild-type cells.

Protein Name (Gene)	# Peptides <Sp FR> / Total	A549 KD control	Protein Name (Gene)	# Peptides <Sp FR> / Total	A549 KD control
Bifunctional aminoacyl-tRNA synthetase (EPRS)	5.8 / 9	40 ± 1	Leukotriene A-4 hydrolase (LTA4H)	5.7 / 7	90 ± 1
Major vault protein (MVP)	17.4 / 25	50 ± 1	Importin subunit beta-1 (KPNA1)	13.4 / 16	90 ± 1
Protein AUC (LMNA)	23.8 / 27	51 ± 1	ATP-dependent RNA helicase A (DHX9)	5.5 / 8	90 ± 1
Coatomer subunit alpha (COPA)	14.7 / 20	55 ± 1	Alanyl-tRNA synthetase, cytoplasmic (AARS)	10.2 / 13	90 ± 1
4F2 cell surface antigen heavy chain (SLC3A2)	12.6 / 16	58 ± 1	Aldehyde dehydrogenase, dimeric NADP-proforming (ALDH3A1)	7.9 / 15	90 ± 1
PDZ and LIM domain protein 5 (PDLIM5)	6.7 / 10	64 ± 1	Threonyl-tRNA synthetase, cytoplasmic (TARS)	12.1 / 16	90 ± 1
Brain acid soluble protein 1 (BASP1)	7.8 / 10	66 ± 1	Serpin H1 (SERPINH1)	7.9 / 12	90 ± 1
ATP-citrate synthase (ACLY)	19.7 / 26	66 ± 1	26S proteasome non-ATPase regulatory subunit 2 (PSMD2)	7.1 / 8	90 ± 1
Catenin alpha-1 (CTNNA1)	6.8 / 10	74 ± 1	Thioredoxin reductase 1, cytoplasmic (TXNRD1)	11.8 / 18	90 ± 1
6-phosphofructokinase, liver type (PFKL)	5.1 / 7	74 ± 1	ATP synthase subunit alpha, mitochondrial (ATP5A1)	9.9 / 16	90 ± 1
Fascin (FSCN1)	8.5 / 12	76 ± 1	Niban like protein 1 (FAM126B)	7.1 / 11	90 ± 1
Stress-induced phosphoprotein 1 (STP1)	6.9 / 10	78 ± 1	Tubulin alpha-1A chain (TUBA1A)	11.1 / 15	90 ± 1
Hypoxia up-regulated protein 1 (HYOU1)	13.6 / 21	78 ± 1	Plectin (PLEC)	34.6 / 62	90 ± 2
UDP-glucose 6-dehydrogenase (UGDH)	10.5 / 19	81 ± 1	Ubiquitin-like modifier activating enzyme 1 (UBA1)	18.9 / 21	90 ± 2
Calreticulin (CALR)	8.9 / 12	83 ± 1	Ritinal dehydrogenase 1 (ALDH1A1)	14.7 / 28	100 ± 1
Transcription factor ISGF-3 components p110beta (STAT1)	13.9 / 18	83 ± 1	Pyruvate kinase isozymes M1/M2 (PKM2)	30.6 / 36	100 ± 1
Myristoylated alanine-rich C-kinase substrate (MARCKS)	6.5 / 8	84 ± 1	Probable ATP-dependent RNA helicase DDX5 (DDX5)	5.3 / 8	100 ± 1
T-complex protein 1 subunit zeta (CCT5A)	6.5 / 10	84 ± 1	WD repeat-containing protein 1 (WDR1)	14.4 / 16	101 ± 2
T-complex protein 1 subunit beta (CCT2)	7.4 / 12	85 ± 1	Gelsolin (GSN)	14.2 / 17	101 ± 1
Palladin (PALLD1)	5.1 / 6	85 ± 1	Polymerase I and transcript release factor (PTRF)	5.1 / 8	101 ± 1
Polyadenylation-binding protein 1 (PABPC1)	8.4 / 10	86 ± 1	Calnexin (CANX)	17.6 / 22	101 ± 2
Exportin 2 (CXSE1L)	6.2 / 9	86 ± 1	60 kDa heat shock protein, mitochondrial (HSPD1)	20.5 / 26	102 ± 1
Myosin-Ib (MYO1B)	8.4 / 11	87 ± 1	Beta actin variant (ACTB)	6.9 / 8	102 ± 1
Talin-1 (TLN1)	16.3 / 29	87 ± 1	Filamin A (FLNA)	70.2 / 87	102 ± 1
Heterogeneous nuclear ribonucleoprotein U (HNRNP-U)	7.3 / 10	88 ± 1	Stress-70 protein, mitochondrial (HSPA9)	18.1 / 20	102 ± 1
T-complex protein 1 subunit gamma (CCT3)	9.3 / 10	88 ± 1	ATP-dependent RNA helicase DDX1 (DDX1)	5.5 / 8	102 ± 1
T-complex protein 1 subunit delta (CCT4)	9.8 / 12	88 ± 1	Clathrin heavy chain 1 (CLTC)	26.9 / 39	103 ± 1
Prolyl 4-hydroxylase subunit alpha-1 (P4HA1)	11.1 / 14	88 ± 1	Transitional endoplasmic reticulum ATPase (VCP)	23.6 / 26	103 ± 2
T-complex protein 1 subunit epsilon (CCT5)	7.0 / 10	88 ± 1	Protein disulfide-isomerase A3 (PDIA3)	17.3 / 20	104 ± 1
Microtubule-associated protein 4 (MAP4)	9.6 / 12	88 ± 1	Protein transport protein Sec31A (SEC31A)	12.4 / 18	105 ± 2
Extended synaptotagmin-1 (ESYT1)	5.8 / 7	88 ± 1	Vacuolar protein sorting-associated protein 35 (VPS35)	7.4 / 10	105 ± 1
Heat shock protein HSP 90 beta (HSP90AB1)	28.7 / 33	88 ± 1	Cytoskeleton-associated protein 4 (CKAP4)	25.1 / 27	105 ± 1
Hecokinase-1 (HK1)	11.7 / 15	88 ± 1	Procollagen-lysine 2-oxoglutarate 5-dioxygenase 2 (PLOD2)	21.3 / 30	105 ± 1
Elongation factor 1-alpha (EEF1A1)	9.3 / 12	90 ± 1	78 kDa glucose-regulated protein (HSPA5)	26.9 / 28	106 ± 2
Ribophony-2 (RPN2)	9.7 / 12	90 ± 1	Protein transport protein Sec23A (SEC23A)	13.0 / 15	106 ± 1
EH domain-containing protein 2 (EHD2)	11.2 / 17	90 ± 1	Importin-7 (IPO7)	7.7 / 10	106 ± 1
Culin-associated NEDD8-dissociated protein 1 (CAND1)	6.1 / 8	90 ± 1	Transformin receptor protein 1 (TRFR)	9.1 / 11	106 ± 1
T-complex protein 1 subunit eta (CCT7)	8.8 / 10	90 ± 1	Coatomer subunit beta' (COPB2)	10.1 / 13	106 ± 2
Heat shock 70 kDa protein 1A1B (HSPA1A)	17.2 / 21	91 ± 1	Plastin-3 (PLS3)	17.0 / 19	107 ± 1
AP-2 complex subunit beta (AP2B1)	12.7 / 17	91 ± 1	6-phosphofructokinase type C (PFKP)	15.2 / 17	107 ± 1
X-ray repair cross-complementing protein 6 (XRCC6)	9.2 / 12	91 ± 1	Mitochondrial inner membrane protein (BMT)	9.9 / 11	107 ± 1
AP-2 complex subunit alpha-1 (AP2A1)	10.7 / 13	91 ± 1	Thrombospondin-1 (THBS1)	14.9 / 23	107 ± 1
T-complex protein 1 subunit theta (CCT8)	11.6 / 15	91 ± 1	Protein disulfide-isomerase (P4HB)	24.8 / 28	107 ± 1
ATP-dependent RNA helicase DDX3X (DDX3X)	5.8 / 8	91 ± 1	Phosphoglucomutase-1 (PGM1)	11.4 / 14	108 ± 1
Heat shock cognate 71 kDa protein (HSPA8)	23.4 / 25	91 ± 1	Paromycin-sensitive aminopeptidase (NPEPPS)	6.4 / 7	108 ± 1
Septin-9 (SEPT9)	5.8 / 8	91 ± 1	Glutaminase kidney isoform, mitochondrial (GLS)	5.6 / 7	108 ± 1
Heterogeneous nuclear ribonucleoprotein Q (SYNCRIP)	7.6 / 9	92 ± 1	Prolyl 4-hydroxylase subunit alpha-2 (P4HA2)	9.8 / 15	108 ± 1
Kinesin 1 heavy chain (KIF5B)	8.6 / 11	92 ± 1	Filamin B (FLNB)	6.7 / 9	108 ± 1
Ribosome-binding protein 1 (RRBP1)	15.8 / 21	92 ± 1	Kinectin (KTN1)	5.0 / 8	109 ± 1
Leucyl-tRNA synthetase, cytoplasmic (LARS)	8.0 / 10	93 ± 1	Caldesmon (CALD1)	29.0 / 34	109 ± 1
Elongation factor 2 (EEF2)	29.2 / 34	93 ± 1	Heat shock 70 kDa protein 4 (HSPA4)	12.5 / 15	109 ± 2
Transketolase (TKT)	18.8 / 24	93 ± 1	5alphacycloccol nuclease domain-containing protein 1 (SND1)	18.9 / 23	109 ± 1
Glucose-6-phosphate 1-dehydrogenase (G6PD)	11.4 / 20	93 ± 1	Importin-5 (IPO5)	13.4 / 17	110 ± 2
Myosin-1c (MYO1C)	17.9 / 23	93 ± 1	5'-nucleotidase (NTSE)	11.6 / 17	110 ± 1
Bifunctional purine biosynthesis protein PURH (ATIC)	9.7 / 13	94 ± 1	Nucleolin (NCL)	11.9 / 15	110 ± 1
Myosin (MSN)	23.4 / 27	94 ± 1	Very long chain specific acyl-CoA dehydrogenase (ACADVL)	7.8 / 9	110 ± 1
Glycyl-tRNA synthetase (GARS)	15.6 / 22	94 ± 1	Neuroblast differentiation-associated protein (AHNAK)	43.8 / 66	110 ± 1
T-complex protein 1 subunit alpha (TCP1)	10.5 / 13	94 ± 1	Endoplasmic reticulum chaperone protein (HSPA8)	15.8 / 30	111 ± 1
Peptidyl-prolyl cis-trans isomerase (FKBP10)	12.1 / 19	94 ± 1	Endoplasmic reticulum chaperone protein (HSPA8)	34.1 / 37	111 ± 2
Heat shock protein HSP 90 alpha (HSPA9AA1)	14.4 / 18	94 ± 2	Glucosylase 2 subunit beta (PRKCSH)	8.8 / 11	113 ± 2
Arginyl-tRNA synthetase, cytoplasmic (RARS)	9.6 / 11	94 ± 1	Alpha actinin-1 (ACTN1)	52.2 / 59	113 ± 2
Eukaryotic translation initiation factor 3 subunit B (EIF3B)	6.4 / 8	94 ± 1	General vesicular transport factor p115 (USO1)	10.1 / 12	113 ± 2
X-ray repair cross-complementing protein 5 (XRCC5)	7.1 / 10	95 ± 1	ATP synthase subunit beta, mitochondrial (ATP5B)	7.8 / 15	115 ± 2
Interleukin enhancer-binding factor 3 (ILF3)	6.4 / 10	95 ± 1	D-fructose-6-phosphate amidotransferase 1 (GFPT1)	13.9 / 16	116 ± 2
Coatomer subunit gamma (COPG)	11.8 / 17	95 ± 1	Isoleucyl-tRNA synthetase, cytoplasmic (IARS)	10.5 / 14	117 ± 2
C-1-tetrahydrofolate synthase, cytoplasmic (MTHFD1)	5.8 / 7	95 ± 1	Vinculin (VCL)	35.5 / 39	120 ± 2
Tubulin beta chain (TUBB1)	11.9 / 18	95 ± 1	Vigilin (VIGLBP)	12.6 / 20	120 ± 2
Programmed cell death 6-interacting protein (PDCD6IP)	12.6 / 14	95 ± 2	Alpha actinin-4 (ACTN4)	34.0 / 37	120 ± 2
RPN1 (RPN1)	18.7 / 21	95 ± 1	Lysosomal membrane protein 2 (SCARB2)	5.0 / 6	122 ± 2
CD44 antigen (CD44)	5.4 / 6	95 ± 1	Integrin alpha-2 (ITGA2)	9.1 / 16	122 ± 2
Calpain-2 catalytic subunit (CAPN2)	11.6 / 17	96 ± 1	Procollagen-lysine 2-oxoglutarate 5-dioxygenase 1 (PLOD1)	10.3 / 13	123 ± 2
Vimentin (VIM)	34.1 / 39	96 ± 1	Dihydropyrimidinase-like 3 (DIPYSL3)	8.3 / 11	124 ± 2
Prolyl 3-hydroxylase 1 (L3EPRE1)	5.6 / 7	96 ± 1	Myoferlin (MYOF)	14.1 / 22	124 ± 2
Heterogeneous nuclear ribonucleoprotein K (HNRNP-K)	9.8 / 12	96 ± 1	Spectrin alpha chain, brain (SPTAN1)	15.1 / 25	127 ± 2
Aminase AII (ANKRD1)	28.5 / 32	96 ± 2	Filamin-C (FLNC)	13.6 / 22	127 ± 2
Adenylyl cyclase-associated protein (CAPT)	9.4 / 14	96 ± 1	Protein glutamine gamma-glutamyltransferase 2 (TGM2)	18.2 / 24	131 ± 2
Glucose-6-phosphate isomerase (GPI)	9.9 / 13	96 ± 1	Integrin beta-1 (ITGB1)	9.9 / 12	138 ± 2
Aminopeptidase N (ANPEP)	15.0 / 21	97 ± 1	Protein NOX20 (FAM114A1)	5.1 / 7	138 ± 2
Medium tumor antigen-associated 61 kDa protein (PPP2R1A)	6.8 / 9	97 ± 1	Integrin, alpha V (ITGAV)	6.6 / 8	140 ± 2
1,4-alpha-glucan branching enzyme (GBE1)	7.8 / 11	97 ± 1	EH domain-containing protein 1 (EHD1)	6.3 / 8	140 ± 2
Coatomer subunit beta (COPB1)	18.4 / 22	97 ± 2	Ras GTPase-activating like protein (GGAU1)	8.7 / 14	143 ± 2
Protein disulfide-isomerase A4 (PDIA4)	16.6 / 18	97 ± 1	LIM domain only protein 7 (LMO7)	5.4 / 8	154 ± 2
Neutral alpha-glucosidase AII (GANN2)	19.3 / 23	97 ± 1	Cytoskeletal dynein 1 heavy chain 1 (DYNC1H1)	6.5 / 11	172 ± 2
Glycogen phosphorylase, brain form (PYGB)	9.4 / 12	97 ± 1	Microtubule-associated protein 1B (MAP1B) (MAP1B)	6.5 / 12	179 ± 2
Bifunctional enzyme subunit alpha, mitochondrial (HADHA)	14.4 / 19	98 ± 1			

Major contributors of peptides to normalization set

Major contributors of peptides to normalization set

Table S4-2. **Proteomic difference between tumor vs. cultured cells** (A) Mass spectrometry-derived quantitation of protein expression in Scr and two siLMNA tumors relative to that of scrambled siRNA-treated in vitro cultured cells (first three columns). The forth column represents relative expression of the same set of proteins between Scr and average of the two siLMNA tumors.

Median Ion Current In Vitro	Tumor	Protein Name (Gene)	Total Pep	<PRF>	Scr (Tumor) Scr (in Vitro)	RD06 (Tumor) Scr (in Vitro)	RD11 (Tumor) Scr (in Vitro)	<RD> (Tumor) Scr (in Vitro)
7.8	7.3	Lamin A/C (LMNA)	1	2.3	182 ± 73	180 ± 38	241 ± 87	233 ± 98
6.7	6.1	Lamin B1 (LMNB1)	1	2.1	218 ± 167	91 ± 20	91 ± 34	194 ± 24
6.7	6.1	Septin-9 (SEPT9)	6	3.1	86 ± 30	46 ± 28	135 ± 56	1338 ± 27737
7.8	6.1	Stress-induced phosphoprotein 1 (STP1)	4	2.9	16 ± 7	31 ± 7	86 ± 25	2923 ± 2323
6.6	6.0	Glutamine kidney isoform, mitochondrial (GLS)	1	2.7	73 ± 37	96 ± 21	276 ± 139	2763 ± 2391
6.7	5.9	Succinate dehydrogenase [ubiquinone] flavoprotein subunit, mito. (SDHA)	1	2.3	39 ± 20	82 ± 14	130 ± 63	1626 ± 1373
6.6	6.3	Dipeptidyl peptidase 1 (DPP1)	4	2.8	71 ± 28	134 ± 101	118 ± 77	1146 ± 1252
6.1	5.9	ATP-dependent diphosphorylation kinase (DAK)	3	2.1	242 ± 176	323 ± 218	329 ± 234	1136 ± 1172
7.0	5.9	Splicing factor, proline- and glutamine-rich (SFPQ)	4	2.1	17 ± 3	33 ± 12	87 ± 37	1683 ± 874
6.8	5.9	DNA replication licensing factor (MCM5)	4	2.3	16 ± 3	16 ± 3	26 ± 12	432 ± 733
6.6	6.3	Apoptosis-inducing factor 1, mitochondrial (AIFM1)	5	2.4	76 ± 31	138 ± 59	97 ± 44	690 ± 1093
6.3	5.7	Arginyl-tRNA synthetase, cytoplasmic (RARS)	5	2.4	82 ± 48	283 ± 232	99 ± 87	793 ± 744
6.2	6.1	UDP-glucose 6-dehydrogenase (UGDH)	3	2.3	333 ± 136	219 ± 96	833 ± 227	676 ± 396
6.5	5.9	NADP-dependent malic enzyme (ME1)	5	2.2	82 ± 31	45 ± 24	113 ± 69	174 ± 423
6.0	6.1	Heterogeneous nuclear ribonucleoprotein U (HNRPU)	3	2.1	244 ± 83	362 ± 129	1068 ± 318	124 ± 207
6.4	5.8	Catalase (CAT)	3	2.1	118 ± 44	196 ± 80	231 ± 96	493 ± 373
7.8	6.3	Heat shock protein HSP 90-alpha (HSP90AA1)	7	3.2	39 ± 13	44 ± 12	72 ± 26	420 ± 306
6.2	5.9	Zinc phosphodiesterase (IAC protein 2) (ZIAC2)	4	2.1	39 ± 23	32 ± 33	61 ± 38	389 ± 220
6.5	6.3	Polypyrimidine tract-binding protein 1 (PTBP1)	5	2.5	120 ± 35	99 ± 26	218 ± 121	290 ± 120
7.1	6.7	CD44 antigen (CD44)	5	2.6	78 ± 25	81 ± 14	108 ± 50	280 ± 138
7.1	6.8	Protein disulfide-isomerase A4 (PDIA4)	13	7.7	126 ± 43	161 ± 35	274 ± 123	373 ± 117
7.6	7.4	Transketolase (TKT)	14	6.5	218 ± 102	138 ± 106	174 ± 112	273 ± 275
6.6	5.7	Eukaryotic translation initiation factor 4B (EIF4B)	6	2.7	118 ± 136	34 ± 9	84 ± 36	264 ± 126
6.9	7.0	Protein disulfide-isomerase (P4H8)	12	5.6	314 ± 148	351 ± 68	91 ± 256	237 ± 132
6.3	7.0	Basal cell adhesion molecule (BCAM)	1	2.1	27 ± 8	33 ± 4	46 ± 17	253 ± 110
6.5	6.2	Glutaminyl-tRNA synthetase (GARS)	5	3.3	132 ± 101	168 ± 24	158 ± 60	246 ± 91
6.8	6.2	Mitochondrial inner membrane protein (IMMT)	19	3.8	132 ± 103	145 ± 84	122 ± 39	243 ± 125
6.5	6.3	Calnexin (CALN1)	4	2.8	114 ± 47	119 ± 21	183 ± 82	339 ± 123
6.6	5.3	Mitochondrial antiviral-signaling protein (MIA3)	3	2.1	25 ± 6	33 ± 6	47 ± 14	329 ± 81
6.5	5.9	Glycyl-tRNA synthetase (GARS)	4	3.1	72 ± 48	139 ± 96	74 ± 38	217 ± 100
6.7	6.4	Cyttoplasmic dyxins 1 intermediate chain 2 (DYX1C2)	3	2.2	119 ± 45	81 ± 16	121 ± 53	216 ± 87
6.7	6.2	SUMO-activating enzyme subunit 2 (SUA2)	5	2.6	183 ± 80	139 ± 72	153 ± 58	189 ± 114
6.2	6.4	Gelsolin (GSN)	9	4.0	697 ± 679	833 ± 398	1620 ± 646	181 ± 100
6.5	6.2	Programmed cell death 6 interacting protein (PDCD6IP)	8	3.8	174 ± 61	174 ± 59	226 ± 84	177 ± 91
6.7	5.7	Protein-glutamine gamma-glutamyltransferase 2 (TGM2)	12	4.5	28 ± 11	24 ± 5	29 ± 16	164 ± 129
7.0	5.8	Nucleolar RNA helicase 2 (DOX1)	8	3.8	28 ± 10	31 ± 18	39 ± 14	161 ± 108
6.6	6.1	Aconitase 2, mitochondrial (ACO2)	3	2.1	229 ± 177	229 ± 204	229 ± 133	559 ± 61
6.8	7.4	Glucose-6-phosphate isomerase (GPI)	10	4.5	1057 ± 238	1267 ± 478	1647 ± 1018	153 ± 76
6.4	6.1	T-complex protein 1 subunit theta (CTC7)	6	3.1	251 ± 87	163 ± 82	263 ± 142	150 ± 99
6.3	6.9	Glucose-6-phosphate 1-dehydrogenase (G6PD)	12	5.1	639 ± 238	605 ± 159	1236 ± 678	144 ± 77
7.3	7.1	Heat shock 70 kDa protein 1A/18 kDa 1A/18 (HSPA1A)	8	3.9	221 ± 130	165 ± 55	139 ± 54	100 ± 71
7.1	6.8	Transcription intermediary factor 1-beta (TRIM28)	4	2.4	122 ± 68	38 ± 10	65 ± 29	137 ± 71
7.0	6.1	T-complex protein 1 subunit beta (CTC2)	3	2.1	1819 ± 1324	1307 ± 398	1731 ± 1108	131 ± 64
6.8	6.8	Irin1 (IRIN)	4	2.2	210 ± 53	243 ± 77	299 ± 124	130 ± 39
6.8	6.5	Cytoskeleton-associated protein 6 (CKAP4)	10	5.1	129 ± 27	126 ± 16	232 ± 92	124 ± 51
6.7	6.7	Aminoacyl-tRNA synthetase 8 (RARS8)	4	2.3	128 ± 90	171 ± 141	263 ± 161	122 ± 19
6.8	5.9	Heat shock protein 70 kDa, mitochondrial (HSPA1)	6	2.9	38 ± 17	33 ± 13	39 ± 25	121 ± 63
6.6	6.3	70 kDa gastrin-binding protein (GAD6A)	14	7.6	151 ± 57	178 ± 70	125 ± 73	117 ± 14
6.6	6.2	Protein disulfide-isomerase A1 (PDIA3)	9	4.0	1376 ± 372	1021 ± 884	1799 ± 1058	116 ± 12
6.6	6.6	Pyruvate kinase (cytosol) M2 isoform (PKM2)	7	3.7	236 ± 137	213 ± 127	215 ± 133	115 ± 15
6.8	6.4	Bifunctional purine biosynthetic protein PURH (KTC)	16	7.0	82 ± 37	108 ± 73	180 ± 124	114 ± 12
7.2	6.9	Calnexin (CANX)	14	6.2	167 ± 49	278 ± 162	143 ± 53	114 ± 9
7.8	6.1	Cytinyl-tRNA synthetase (CARS)	4	2.1	126 ± 69	88 ± 51	88 ± 56	113 ± 25
6.5	6.1	Heat shock related 70 kDa protein 2 (HSPA2)	5	2.3	150 ± 42	87 ± 30	144 ± 55	111 ± 19
6.4	6.1	Calpain-1 catalytic subunit (CAPN1)	10	5.8	405 ± 157	318 ± 181	299 ± 147	110 ± 23
6.9	6.9	Thromboxyl synthetase, cytoplasmic (TARS)	6	3.5	79 ± 43	76 ± 43	85 ± 43	110 ± 18
6.6	6.1	Asparaginyl-tRNA synthetase, cytoplasmic (NARS)	5	2.6	118 ± 34	102 ± 46	82 ± 40	107 ± 33
6.6	6.4	Very long-chain specific acyl-CoA dehydrogenase, mitochondrial (ACADVL)	13	7.0	189 ± 73	197 ± 75	208 ± 122	107 ± 11
7.0	6.7	X-ray repair cross-complementing protein 6 (XRCC6)	21	9.2	122 ± 37	100 ± 30	106 ± 24	107 ± 13
6.9	6.8	X-ray repair cross-complementing protein 5 (XRCC5)	21	8.7	161 ± 36	134 ± 44	123 ± 30	106 ± 17
6.6	6.2	NADH ubiquinone oxidoreductase 75 kDa subunit, mitochondrial (NDUFB1)	3	2.3	361 ± 436	368 ± 416	249 ± 295	105 ± 21
6.0	6.5	Calpastatin (CAST)	4	2.1	1860 ± 1361	1873 ± 1162	1019 ± 878	105 ± 17
6.7	6.3	Far upstream element-binding protein 2 (KHSRP)	5	2.6	192 ± 100	147 ± 100	133 ± 46	105 ± 16
6.0	6.1	Phosphoglucosaminase-1 (PGAL1)	5	2.7	499 ± 299	400 ± 367	327 ± 236	104 ± 17
6.6	6.5	Leukotriene A-4 hydrolase (LIPH)	8	4.4	332 ± 191	160 ± 97	121 ± 56	104 ± 14
6.5	6.0	Transferrin receptor protein 1 (TFRC)	12	5.8	102 ± 58	86 ± 50	53 ± 18	100 ± 19
6.6	6.7	Retinol dehydrogenase 1 (RDH1A)	11	5.3	304 ± 227	328 ± 423	433 ± 189	99 ± 22
6.6	6.1	Glycogen phosphorylase, brain form (PYGL)	6	3.5	1648 ± 1168	1389 ± 1089	132 ± 417	86 ± 21
6.0	6.3	Thioredoxin reductase 1, cytoplasmic (TXNRD1)	8	3.5	638 ± 318	308 ± 199	294 ± 184	99 ± 21
6.1	6.9	Nucleolin (NCL)	11	5.5	104 ± 62	86 ± 50	81 ± 43	88 ± 36
6.6	6.2	Sec substrate contactin (CTTNB)	3	2.1	77 ± 27	79 ± 26	62 ± 27	87 ± 25
6.3	5.9	Calcium-binding mitochondrial carrier protein Anlar2 (SLC25A11)	3	2.1	186 ± 132	152 ± 124	86 ± 94	87 ± 25
6.3	6.8	Calpain-2 catalytic subunit (CAPN2)	6	3.0	914 ± 335	790 ± 314	497 ± 369	86 ± 22
6.5	5.8	Ribophorin-2 (RPN2)	6	2.7	61 ± 34	88 ± 56	36 ± 30	95 ± 29
6.0	6.4	Ubiquitin-like modifier-activating enzyme 1 (UBA1)	5	2.4	1978 ± 1365	2573 ± 1398	829 ± 910	84 ± 11
7.7	7.1	Deregulation factor 2 (DEF2)	3	2.1	143 ± 34	129 ± 45	106 ± 34	94 ± 15
6.6	6.2	Lysyl-tRNA synthetase (KARS)	5	2.7	95 ± 27	74 ± 31	75 ± 22	94 ± 14
6.7	6.4	Ribophorin-1 (RPN1)	9	4.1	231 ± 161	126 ± 80	200 ± 69	93 ± 12
6.9	6.5	Gluconidase 2 subunit beta (PRKG2)	10	4.3	133 ± 44	102 ± 31	160 ± 48	92 ± 13
6.8	5.9	T-complex protein 1 subunit epsilon (CTCE)	5	2.4	38 ± 7	41 ± 30	37 ± 9	90 ± 14
6.5	6.1	T-complex protein 1 subunit zeta (CTCZA)	4	2.1	99 ± 52	49 ± 23	123 ± 64	90 ± 17
6.4	5.7	Annexin A6 (ANXA6)	5	2.6	73 ± 71	75 ± 53	46 ± 16	68 ± 28
7.5	6.9	60 kDa heat shock protein, mitochondrial (HSPD1)	7	3.0	81 ± 24	180 ± 185	78 ± 33	68 ± 29
6.4	5.8	DNA replication licensing factor (MCM7)	7	2.4	90 ± 63	36 ± 38	49 ± 41	68 ± 16
6.5	5.8	Neurolysin, mitochondrial (NLN)	3	2.1	117 ± 29	106 ± 27	72 ± 29	66 ± 11
7.0	6.7	#12 cell-surface antigen heavy chain (SLC3A2)	17	8.5	89 ± 18	72 ± 20	57 ± 12	84 ± 9
6.8	6.2	Neutral alpha-glycosidase AB (GALNA8)	6	2.5	193 ± 83	181 ± 39	52 ± 24	83 ± 37
6.5	6.2	Ribosome-binding protein 1 (RBP1)	6	2.2	818 ± 1917	3317 ± 1116	1339 ± 1997	82 ± 43
6.3	6.0	Epigallocatechin gallate-binding protein 14 (TRIM14)	4	2.6	194 ± 106	139 ± 113	32 ± 18	80 ± 10
6.4	5.9	Glycogen phosphorylase, liver form (PYGL)	4	2.1	342 ± 169	374 ± 238	163 ± 124	79 ± 15
6.4	5.8	tRNA (lysine)-5-methyltransferase (NSUN2)	4	2.3	148 ± 80	106 ± 84	79 ± 57	78 ± 16
6.9	6.3	β-phosphotransferase type C (PFKB)	13	5.9	74 ± 18	66 ± 15	64 ± 21	78 ± 11
7.2	7.1	Endoplasmic reticulum protein 1 (ERPF1)	8	4.1	322 ± 173	219 ± 30	81 ± 17	77 ± 27
6.6	5.8	Neutral amino acid transporter B0 (SLC1A5)	4	2.6	84 ± 59	48 ± 31	37 ± 30	74 ± 12
6.2	5.7	Methionyl-tRNA synthetase, cytoplasmic (MARS)	8	3.1	133 ± 92	88 ± 51	48 ± 17	64 ± 22
6.3	6.2	Purothionin-sensitive aminopeptidase (NPEPPS)	3	2.1	331 ± 162	188 ± 142	38 ± 19	39 ± 9
6.5	5.8	DNA replication licensing factor (MCM5)	5	2.1	84 ± 45	16 ± 5	17 ± 5	15 ± 12
7.7	7.4	Alpha-actinin-4 (ACTN4)	6	3.2	172 ± 49	66 ± 13	15 ± 5	25 ± 4
6.8	6.6	Alpha-actinin-1 (ACTN1)	5	2.4	214 ± 108	33 ± 40	17 ± 10	19 ± 7

1/10

Major contributors to normalization peptide set

% ± s.e.

4-7. Reference

Akter, R., Rivas, D., Geneau, G., Drissi, H. and Duque, G. (2009). Effect of Lamin A/C Knockdown on Osteoblast Differentiation and Function. *Journal of Bone and Mineral Research* **24**, 283-293.

Barnes H.A. (2000). Handbook of Elementary Rheology. University of Wales, Institute of Non-Newtonian Fluid Mechanics

Beadle, C., Assanah, M. C., Monzo, P., Vallee, R., Rosenfeld, S. S. and Canoll, P. (2008). The role of myosin II in glioma invasion of the brain. *Molecular Biology of the Cell* **19**, 3357-3368.

Belt, E. J. T., Fijneman, R. J. A., van den Berg, E. G., Bril, H., Delis-van Diemen, P. M., Tijssen, M., van Essen, H. F., de Lange-de Klerk, E. S. M., Belien, J. A. M., Stockmann, H. B. A. C. et al. (2011). Loss of lamin A/C expression in stage II and III colon cancer is associated with disease recurrence. *European Journal of Cancer* **47**, 1837-1845.

Broers, J. L. V., Ramaekers, F. C. S., Bonne, G., Ben Yaou, R. and Hutchison, C. J. (2006). Nuclear lamins: Laminopathies and their role in premature ageing. *Physiological Reviews* **86**, 967-1008.

Chamberlain, J. S., Metzger, J., Reyes, M., Townsend, D. W. and Faulkner, J. A. (2007). Dystrophin-deficient mdx mice display a reduced life span and are susceptible to spontaneous rhabdomyosarcoma. *Faseb Journal* **21**, 2195-2204.

Cheng, G., Tse, J., Jain, R. K. and Munn, L. L. (2009). Micro-Environmental Mechanical Stress Controls Tumor Spheroid Size and Morphology by Suppressing Proliferation and Inducing Apoptosis in Cancer Cells. *Plos One* **4**.

Coffinier, C., Jung, H. J., Nobumori, C., Chang, S., Tu, Y. P., Barnes, R. H., Yoshinaga, Y., de Jong, P. J., Vergnes, L., Reue, K. et al. (2011). Deficiencies in lamin B1 and lamin B2 cause neurodevelopmental defects and distinct nuclear shape abnormalities in neurons. *Molecular Biology of the Cell* **22**, 4683-4693.

Dahl, K. N., Engler, A. J., Pajerowski, J. D. and Discher, D. E. (2005). Power-law rheology of isolated nuclei with deformation mapping of nuclear substructures. *Biophysical Journal* **89**, 2855-2864.

Dahl, K. N., Ribeiro, A. J. S. and Lammerding, J. (2008). Nuclear shape, mechanics, and mechanotransduction. *Circulation Research* **102**, 1307-1318.

Dechat, T., Pflughaar, K., Sengupta, K., Shimi, T., Shumaker, D. K., Solimando, L. and Goldman, R. D. (2008). Nuclear lamins: major factors in the structural organization and function of the nucleus and chromatin. *Genes Dev* **22**, 832-53.

Dembo, M. and Wang, Y. L. (1999). Stresses at the cell-to-substrate interface during locomotion of fibroblasts. *Biophysical Journal* **76**, 2307-2316.

Dote, H., Burgan, W. E., Camphausen, K. and Tofilon, P. J. (2006). Inhibition of hsp90 compromises the DNA damage response to radiation. *Cancer Res* **66**, 9211-20.

Elbashir, S. M., Harborth, J., Lendeckel, W., Yalcin, A., Weber, K. and Tuschl, T. (2001). Duplexes of 21-nucleotide RNAs mediate RNA interference in cultured mammalian cells. *Nature* **411**, 494-498.

Foster, C. R., Przyborski, S. A., Wilson, R. G. and Hutchison, C. J. (2010). Lamins as cancer biomarkers. *Biochemical Society Transactions* **38**, 297-300.

Friedl, P., Maaser, K., Klein, C. E., Niggemann, B., Krohne, G. and Zanker, K. S. (1997). Migration of highly aggressive MV3 melanoma cells in 3-dimensional collagen lattices results in local matrix reorganization and shedding of alpha 2 and beta 1 integrins and CD44. *Cancer Research* **57**, 2061-2070.

Frock, R. L., Kudlow, B. A., Evans, A. M., Jameson, S. A., Hauschka, S. D. and Kennedy, B. K. (2006). Lamin A/C and emerin are critical for skeletal muscle satellite cell differentiation. *Genes & Development* **20**, 486-500.

Goetz, M. P., Toft, D., Reid, J., Ames, M., Stensgard, B., Safgren, S., Adjei, A. A., Sloan, J., Atherton, P., Vasile, V. et al. (2005). Phase I trial of 17-allylamino-17-demethoxygeldanamycin in patients with advanced cancer. *J Clin Oncol* **23**, 1078-87.

Houghton, J., Stoicov, C., Nomura, S., Rogers, A. B., Carlson, J., Li, H. C., Cai, X., Fox, J. G., Goldenring, J. R. and Wang, T. C. (2004). Gastric cancer originating from bone marrow-derived cells. *Science* **306**, 1568-1571.

Hutchison, C. J. and Worman, H. J. (2004). A-type lamins: Guardians of the soma? *Nature Cell Biology* **6**, 1062-1067.

Johnson, C. P., Tang, H. Y., Carag, C., Speicher, D. W. and Discher, D. E. (2007). Forced unfolding of proteins within cells. *Science* **317**, 663-6.

Jung, H. J., Coffinier, C., Choe, Y., Beigneux, A. P., Davies, B. S. J., Yang, S. H., Barnes, R. H., Hong, J., Sun, T., Pleasure, S. J. et al. (2012). Regulation of prelamin A but not lamin C by miR-9, a brain-specific microRNA. *Proceedings of the National Academy of Sciences of the United States of America* **109**, E423-E431.

Kaufmann, S. H., Mabry, M., Jasti, R. and Shaper, J. H. (1991). Differential Expression of Nuclear-Envelope Lamin-a and Lamin-C in Human Lung-Cancer Cell-Lines. *Cancer Research* **51**, 581-586.

Kim, Y., Sharov, A. A., McDole, K., Cheng, M., Hao, H., Fan, C. M., Gaiano, N., Ko, M. S. H. and Zheng, Y. (2011). Mouse B-Type Lamins Are Required for Proper Organogenesis But Not by Embryonic Stem Cells. *Science* **334**, 1706-1710.

Lammerding, J., Fong, L. G., Ji, J. Y., Reue, K., Stewart, C. L., Young, S. G. and Lee, R. T. (2006). Lamins A and C but not lamin B1 regulate nuclear mechanics. *Journal of Biological Chemistry* **281**, 25768-25780.

Luxton, G. W. G., Gomes, E. R., Folker, E. S., Vintinner, E. and Gundersen, G. G. (2010). Linear Arrays of Nuclear Envelope Proteins Harness Retrograde Actin Flow for Nuclear Movement. *Science* **329**, 956-959.

Maloney, A., Clarke, P. A., Naaby-Hansen, S., Stein, R., Koopman, J. O., Akpan, A., Yang, A., Zvelebil, M., Cramer, R., Stimson, L. et al. (2007). Gene and protein expression profiling of human ovarian cancer cells treated with the heat shock protein 90 inhibitor 17-allylamino-17-demethoxygeldanamycin. *Cancer Res* **67**, 3239-53.

Mayr, M., Hu, Y. H., Hainaut, P. and Xu, Q. B. (2002). Mechanical stress-induced DNA damage and rac-p38MAPK signal pathways mediate p53-dependent apoptosis in vascular smooth muscle cells. *Faseb Journal* **16**, 1423-+.

Meng, X. N., Jin, Y., Yu, Y., Bai, J., Liu, G. Y., Zhu, J., Zhao, Y. Z., Wang, Z., Chen, F., Lee, K. Y. et al. (2009). Characterisation of fibronectin-mediated FAK signalling pathways in lung cancer cell migration and invasion. *British Journal of Cancer* **101**, 327-334.

Mierke, C. T., Frey, B., Fellner, M., Herrmann, M. and Fabry, B. Integrin alpha5beta1 facilitates cancer cell invasion through enhanced contractile forces. *J Cell Sci* **124**, 369-83.

Nakamizo, A., Marini, F., Amano, T., Khan, A., Studeny, M., Gumin, J., Chen, J., Hentschel, S., Vecil, G., Dembinski, J. et al. (2005). Human bone marrow-derived mesenchymal stem cells in the treatment of gliomas. *Cancer Research* **65**, 3307-3318.

Nash, S., Stafford, J. and Madara, J. L. (1987). Effects of Polymorphonuclear Leukocyte Transmigration on the Barrier Function of Cultured Intestinal Epithelial Monolayers. *Journal of Clinical Investigation* **80**, 1104-1113.

Olins, A. L., Herrmann, H., Lichter, P., Kratzmeier, M., Doenecke, D. and Olins, D. E. (2001). Nuclear envelope and chromatin compositional differences comparing undifferentiated and retinoic acid- and phorbol ester-treated HL-60 cells. *Experimental Cell Research* **268**, 115-127.

Pajerowski, J. D., Dahl, K. N., Zhong, F. L., Sammak, P. J. and Discher, D. E. (2007). Physical plasticity of the nucleus in stem cell differentiation. *Proceedings of the National Academy of Sciences of the United States of America* **104**, 15619-15624.

Pillay, J., den Braber, I., Vrisekoop, N., Kwast, L. M., de Boer, R. J., Borghans, J. A. M., Tesselaar, K. and Koenderman, L. (2010). In vivo labeling with (H²O)-H-2 reveals a human neutrophil lifespan of 5.4 days. *Blood* **116**, 625-627.

Pittenger, M. F. and Martin, B. J. (2004). Mesenchymal stem cells and their potential as cardiac therapeutics. *Circulation Research* **95**, 9-20.

Roman, J., Ritzenthaler, J. D., Roser-Page, S., Sun, X. J. and Han, S. W. (2010). alpha 5 beta 1-Integrin Expression Is Essential for Tumor Progression in Experimental Lung Cancer. *American Journal of Respiratory Cell and Molecular Biology* **43**, 684-691.

Rubinstein, M. and Colby, R. H. (2003). Polymer physics. Oxford ; New York: Oxford University Press.

Scaffidi, P. and Misteli, T. (2006). Lamin A-dependent nuclear defects in human aging. *Science* **312**, 1059-1063.

Schirmer, E. C. and Gerace, L. (2004). The stability of the nuclear lamina polymer changes with the composition of lamin subtypes according to their individual binding strengths. *Journal of Biological Chemistry* **279**, 42811-42817.

Shimi, T., Pflieger, K., Kojima, S., Pack, C. G., Solovei, I., Goldman, A. E., Adam, S. A., Shumaker, D. K., Kinjo, M., Cremer, T. et al. (2008). The A- and B-type nuclear lamin networks: microdomains involved in chromatin organization and transcription. *Genes Dev* **22**, 3409-21.

Shin, J. W., Swift, J., Spinler, K. R. and Discher, D. E. (2011). Myosin-II inhibition and soft 2D matrix maximize multinucleation and cellular projections typical of platelet-producing megakaryocytes. *Proceedings of the National Academy of Sciences of the United States of America* **108**, 11458-11463.

Shive, M. S., Brodbeck, W. G. and Anderson, J. M. (2002). Activation of caspase 3 during shear stress-induced neutrophil apoptosis on biomaterials. *Journal of Biomedical Materials Research* **62**, 163-168.

Sullivan, T., Escalante-Alcalde, D., Bhatt, H., Anver, M., Bhat, N., Nagashima, K., Stewart, C. L. and Burke, B. (1999). Loss of A-type lamin expression compromises nuclear envelope integrity leading to muscular dystrophy. *Journal of Cell Biology* **147**, 913-919.

Swift, J., Ivanovska, I., ... and Discher, D. E. (2012) *Submitted*

Tilli, C. M. L. J., Ramaekers, F. C. S., Broers, J. L. V., Hutchison, C. J. and Neumann, H. A. M. (2003). Lamin expression in normal human skin, actinic keratosis, squamous cell carcinoma and basal cell carcinoma. *British Journal of Dermatology* **148**, 102-109.

Trepel, J., Mollapour, M., Giaccone, G. and Neckers, L. (2010). Targeting the dynamic HSP90 complex in cancer. *Nature Reviews Cancer* **10**, 537-549.

Tsai, J. W., Chen, Y., Kriegstein, A. R. and Vallee, R. B. (2005). LIS1 RNA interference blocks neural stem cell division, morphogenesis, and motility at multiple stages. *Journal of Cell Biology* **170**, 935-945.

Weinberg, R. A. (2007). *The biology of cancer*. New York: Garland Science.

Willis, N. D., Wilson, R. G. and Hutchison, C. J. (2008). Lamin A: a putative colonic epithelial stem cell biomarker which identifies colorectal tumours with a more aggressive phenotype. *Biochem Soc Trans* **36**, 1350-3.

Winnard, P. T., Kluth, J. B. and Raman, V. (2006). Noninvasive optical tracking of red fluorescent protein-expressing cancer cells in a model of metastatic breast cancer. *Neoplasia* **8**, 796-U12.

Wolf, K., Mazo, I., Leung, H., Engelke, K., von Andrian, U. H., Deryugina, E. I., Strongin, A. Y., Brocker, E. B. and Friedl, P. (2003). Compensation mechanism in tumor cell

migration: mesenchymal-amoeboid transition after blocking of pericellular proteolysis. *Journal of Cell Biology* **160**, 267-277.

Yamada, S., Yanamoto, S., Yoshida, H., Yoshitomi, I., Kawasaki, G., Mizuno, A. and Nemoto, T. K. (2010). RNAi-mediated downregulation of alpha-actinin-4 decreases invasion potential in oral squamous cell carcinoma. *International Journal of Oral and Maxillofacial Surgery* **39**, 61-67.

Yang, J., Mani, S. A., Donaher, J. L., Ramaswamy, S., Itzykson, R. A., Come, C., Savagner, P., Gitelman, I., Richardson, A. and Weinberg, R. A. (2004). Twist, a master regulator of morphogenesis, plays an essential role in tumor metastasis. *Cell* **117**, 927-939.

Zhang, X. D., Gillespie, S. K. and Hersey, P. (2004). Staurosporine induces apoptosis of melanoma by both caspase-dependent and -independent apoptotic pathways. *Molecular Cancer Therapeutics* **3**, 187-197.

Chapter 5: Conclusions

5-1. Long-circulating Nano-particles for Cancer Therapies

Based on the previous studies with flexible Filomicelles showing increased circulation time and enhanced therapeutic efficacy against model subcutaneous tumor, the presented study explored the possibility of the use of Filomicelles against brain tumor, which is one of the most challenging types of cancer. Brain tumor cell, or glioblastoma multiforme, itself shows high susceptibility against model drug used in this study, paclitaxel (TAX). It is the poor accessibility that makes brain cancer highly difficult to cure. Strict control of material transport across the brain vasculature (BBB) rejects intravasation of even small molecules ($< \text{kDa}$) as well as macromolecules or sub-micron particles. Filomicells were previously shown to circulate long enough to reach brain vasculature, but remained inside the blood vessel. This observation motivated the use of radiation therapy to achieve temporal disruption in BBB to let circulating particles sneak into the brain tumor tissue to release the cargo drug molecules inside. Successful extension of the survival of brain tumor-bearing mice treated with the combination therapy is encouraging, but the future study needs to cover entire sets of controls necessary to support the current result: empty carrier control; conventional formulation of TAX with Cremophor EL; and less circulating polymer nano-carrier with non-worm morphologies. TAX dose dependence of therapeutic effect will also strongly support validation of the combination therapy.

Longer circulation time of a drug-loaded nano-particle increases the possibility of the system to eventually reach the tumor tissue. Widely used PEG is beneficial for avoiding the attachment of particular serum proteins, opsonins, which serves as a flag for immune cell to recognize the particles and uptake. Many studies have shown eventual opsonization of PEG-coated particles, which inevitably leads to the clearance from systemic circulation and poor therapeutic effect of drug delivery system. Attachment of CD47 or CD47-derived ‘Self’ peptide increased accumulation of model particle in subcutaneous tumor tissue and even tumor shrinkage when TAX was loaded. The future study should apply CD47 or ‘Self’ peptide to real drug delivery system instead of polystyrene beads, with particular disease model rather than flank tumors. Combination use of PEG and ‘Self’ protein/peptide may be possible to achieve next-generation targeted therapeutics that can actively avoid both opsonization and clearance by immune cells in case the particle eventually get opsonized.

5-2. Nuclear Physics of Cancer Cells and Tumor Progression

Lamin-A,C expression and nuclear stiffness varies significantly among cell types with distinct origins, recently revealing the strong correlation with surrounding tissue stiffness. This observation in a sense leads to the reduction that nuclear Lamins have strong influences on wide range of cell phenotypes from differentiation state to cell migration capacity. Lamin isoform ratio nicely predicts cell migration sensitivity to Lamin-A,C expression change and nuclear physics (i.e. viscosity vs. elasticity of nucleus as a

viscoelastic material) with all the tested three cell lines with different origins, functions and phenotypes. Lamin-A,C knockdown commonly reduces the obstacle for cell migration process in all tested cell lines, but at the same time impairs protection against mechanical stress exerted against cells migrating through physically constraining environment. Understanding or better control of Lamin-A,C expression and cell migration capability in particular cell is beneficial in various possible applications such as cancer diagnosis/prognosis (deducing the reports that some cancer cells possess Lamin-A,C level different from surrounding healthy cells) or optimization of motility of mesenchymal stem cells that can be used in regenerative medicine. Future study requires further investigation into how quantitatively Lamin-A,C affects migration in individual cell level in various cell types to achieve better prediction of cell motility in real tissues.